Ex vivo Validation of PET Imaging by 3D-printed Phantoms

C.F. Groenendijk

Ex vivo Validation of PET Imaging by 3D-printed Phantoms

by

C.F. Groenendijk

to obtain the degree of Master of Science
at the Delft University of Technology,
to be defended publicly on Thursday December 6, 2018 at 11:00 AM.

Student number: 4261798

Thesis committee:	Dr. ir. D.R. Schaart,	TU Delft, supervisor
	Dr. ir. M. Goorden,	TU Delft
	Dr. ir. A. G. Denkova,	TU Delft
	Dr. J.M.C. Brown,	TU Delft
	Dr. S.F. Petit	Erasmus MC, Rotterdam

This thesis is confidential and cannot be made public until July 20, 2019.

Acknowledgements

With this master thesis I complete the final requirements for the degree of Master of Science in Medical Physics at Delft University of Technology (TU Delft), the Netherlands. In this document "*Ex vivo* Validation of PET Imaging by the use of 3D-Printed Phantoms" I present my exploration and new insights in the characterization of the Inveon microPET system to assess tumor heterogeneity by proposing development of FDG-PET during radiotherapy treatment for non-small cell lung cancer patients.

For the thesis' existence I have many people to thank for and I am pleased to do so. First of all, I would like to thank Steven Petit, Assistant Professor Department of Radiation Oncology (Erasmus MC), who inspired me by his research on validation of functional imaging to measure intra-tumor heterogeneity and invited me to be part of it.

I owe my greatest debt to my supervisor Jeremy Brown, Post-Doc at section Medical Physics & Technology (TU Delft), for improving my understanding about everything but especially image reconstruction. His probing questions inspired me to further research and to dig deeper, so I could increase this research' academic value. Thank you for all the time you invested in me and the great support you have provided during my project.

Great guidance provided by Jan von der Thüsen, Consultant Histopathologist (Erasmus MC) and Titia Meijer, PhD-student, gave important relevance to the search results. The inspiring discussions with Marcel Segbers and Mark Konijnenberg, Medical Physicists (Erasmus MC) have improved the analysis.

I am very grateful for the help from DEMO group (TU Delft) especially Kevin Kamman, by the 3D-printing of the phantom samples needed for my research. And for the indispensable assistance of Jan de Swart, Preclinical Imaging Specialist (Erasmus MC) at the phantom experiments with the microPET scanner.

Special thanks to my valued fellow master students Elise, Eline and Vincent (Reactor Institute Delft) for helpful comments and a lot of fun.

I am deeply indebted to Dennis Schaart, Head of Section Medical Physics & Technology at Radiation Science & Technology (TU Delft) for his overall guidance throughout this research project.

I am very grateful to my family for their warm support during my study, especially my parents and my brother who are always encouraging me to pursue my intellectual interests. I am also lucky to have friends who nurture my intellectual aspirations, they kept me going.

C.F. Groenendijk
Delft, December 2018

Contents

List of Figures

1

Ex vivo Validation of PET Imaging
A Review

C.F. Groenendijk
Literature Study - Medical Physics
November 26, 2018

Abstract
Radioresistence to radiotherapy accounts for poor local tumor control in Non-Small Cell Lung Cancer (NSCLC) patients. On-treatment FDG-PET imaging allows the detection of radioresistant regions and escalation of the dose to these regions. Pathology is a requisite in the correlation of FDG uptake with a biological trait. In inoperable NSCLC patients, the pathology cannot be accessed, introducing the exPET study to maintain viability of resected tissue specimens. To validate this proposition, *ex vivo* experiments will be accomplished to compare pathological characteristics with FDG-PET uptake values. Findings attained from the investigated studies indicate a desire to an automated detection algorithm of proliferating cells in Ki-67 immunostained tissue specimens. The *ex vivo* culturing platform will allow the assessment of FDG uptake measured by the Inveon microPET scanner. Characterization of the system will by performed by the use of 3D-printed high spatially encoded geometries resembling tumor characteristics, introducing a whole new insight in the characterization of the Inveon microPET system. An ideal method in exploring tumor heterogeneity is presented thereby proposing development of FDG-PET during radiotherapy treatment in NSCLC patients.

Introduction

Non-Small Cell Lung Cancer (NSCLC) accounts for 80%-85% of all lung cancers of which the majority are diagnosed as inoperable. Thoracic radiotherapy is the main treatment used in inoperable stage III NSCLC patients which is associated with poor outcomes, encountering an average survival of 9 to 11 months and a 2- and 3-year survival of 10-20% and 5-10% respectively [68]. In the current radiotherapy treatment, a homogeneous dose is delivered to the tumor. However, since NSCLC tumors are heterogeneous masses, radiotherapy treatment leads to a non-homogeneous response within tumors due to radioresistant regions. This is may be an important cause of poor local tumor control in NSCLC and the result of local recurrences and treatment failure [66]. The introduction of response imaging during the course of the treatment was proposed as an initial step to overcome this problem. Measuring the response non-invasively *in vivo* by the use of the functional imaging modality positron emission tomography (PET) could identify resistant regions. Escalating the dose to these poorly responding regions and reducing it in more susceptible regions may increase local tumor control whilst minimizing the occurrence of possible side effects [26, 75].

In order to measure response, the radioactive tracer 2-deoxy-2-(^{18}F)fluoro-D-glucose (FDG) can be used to correlate with different biological processes. FDG has been proven feasible in distinguishing variation in response between tumors [74]. However, the challenge remains to validate the correlation of the imaging target with a local biological trait. In order to correlate FDG with a biological trait, a ground truth is required concerning the pathology of the tissue in which biological characteristics can be analyzed. Since it concerns inoperable NSCLC patients, the pathology cannot be accessed. Maintaining viability of tissue specimens could be a step towards the *ex vivo* comparison between pathological characteristics and FDG-PET imaging outcomes. This task has driven the introduction of the exPET study, stating the *ex vivo* validation of PET imaging for radiotherapy response assessment for NSCLC. In the proposed study *ex vivo* experiments of NSCLC specimens could allow the detection of viable regions based on FDG uptake in tissue slices, which will contribute to one of the main challenges of the exPET study. Other challenges include the imaging of the minuscule tissue specimens by the use of FDG-PET and the identification of differences in FDG concentrations. Next, the pathological examination of proliferation active areas is accepted as a challenge in the exPET study in which it would be highly beneficial to detect the number of proliferating cells by an automated detection algorithm. Discussed topics include the biological complexity of tumors, concept of dose painting, issue of detecting proliferation active areas based on a proliferation marker, *ex vivo* experiments and microPET.

Tumor Heterogeneity

Cancer arises by the occurrence of multiple mutations that create mutant clones [29]. The development of mutant clones is influenced by intrinsic factors including genetic effects and extrinsic factors including the the surrounding micro-environment [67]. Variation at the genetic and phenotypic level is noticed between tumors of different cell and tissue types, as well as among individuals with the same type of tumor, which is defined as inter-tumor heterogeneity. However, diversity in genetically distinct subclones is observed within tumors, which is defined as intra-tumor heterogeneity [59]. This heterogeneous collection of cell types is responsible for the spatially separation of the micro-environment [13]. Information about spatial variation has been well observed in pathological examinations showing coexisting regions of vasculature, cell density, normal tissue involvement, proliferation and hypoxia [5, 46, 92]. The aforementioned biological characteristics of the tumor influence the response to radiotherapy [46], explained by the fact that genetic transformations are caused by cell-intrinsic biological properties [13], showing radioresistant behavior in tumor eradication [61]. Radio-resistance is an important factor responsible for the failure of radio- and chemotherapy and the poor prognosis in cancer patients, ultimately leading to metastases and tumor recurrence [77].

Dose Painting

Irradiation of the tumor with a larger dose may improve local tumor control. However, dose escalation to the entire tumor is hampered by the tolerance of surrounded normal tissue [26]. Due to the extreme inter-patient variability in the severity of toxicity after a certain dose of radiotherapy, the given dose is not at the highest possible level in many individual patients because dose thresholds are set based on the most sensitive patients [8]. A potential solution to handle tumor heterogeneity is to boost delivered dose to radioresistant regions [2]. The determination of the spatial maps visualizing tumor heterogeneity upon which the selective boosting must be determined can be accomplished by functional imaging techniques before treatment [78]. This concept of dose painting based on pre-treatment biological images was introduced by Ling et al. They stated that biological images were of great interest in the distribution of dose and could be applied in intensity-modulated radiotherapy (IMRT) [50]. By visualizing areas with potential radio-resistance, additional dose was 'painted' onto that volume. An example in which dose painting was employed based on a biological characteristic is hypoxia, which is characterized by poor oxygenation of the tissue [10]. Hypoxia is one of the important biological characteristics that instigate radio-resistancy in radiotherapy [52]. This concept was further performed by Chao et al. who investigated the feasibility of targeting the tumor based on hypoxic areas and preventing the irradiation of normal tissues by the use of IMRT. Their results showed a successful method in which an increased dose was delivered in the hypoxic tumor volume without affecting normal tissue sparing [15]. Furthermore, Malinen et al. compared uniform and non-uniform dose distributions in IMRT based on hypoxic regions. Results showed a factor three increase in tumor control probability concerning the non-uniform dose distribution [53], substantiating the concept of dose escalation based on the biological characteristic hypoxia. Thorwarth et al. investigated the effect on tumor control probability in different dose escalation plans. Conventional IMRT was compared to a uniform dose escalation plan and a plan based on dose painting by numbers, both based on hypoxia. For the latter a map of dose escalation factors was implemented based on dynamic [^{18}F]-fluoromisonidazole PET data. Both dose escalation plans were proved to have an increased tumor control probability where dose painting by numbers was perceived to more effectively deliver dose compared to an additional uniform dose escalation [79].

The mentioned studies demonstrated that the concept of dose painting based on pre-treatment images improved local tumor control and that it is a useful method to deal with tumor heterogeneity. The concept of dose-painting based on response during treatment is of concern in the proposed study. Several studies verified the feasibility of response assessment by the use of FDG-PET imaging during the course of a radiotherapy treatment and considered it as a potential method towards personalized treatments. Aerts et al. investigated whether high FDG uptake sites within NSCLC tumors remain stable during radiotherapy treatment. They drew the conclusion that FDG uptake sites do remain stable during radiotherapy, enabling the possibility of dose escalations to radio-resistant areas within the tumor determined by FDG-PET [1]. Furthermore, the group of Van Baardwijk et al. aimed for treatment adaptations based on early responses on radiotherapy in NSCLC patients. Outcomes showed several fluctuations within FDG uptake values during treatment. As a consequence, predicting response in an early stage appeared to be difficult. According to them, the biological meaning of these fluctuations must be examined in order to use response based dose escalations accurately in the future [83]. Gillham et al. tested the hypothesis whether FDG-PET imaging during radiotherapy treatment facilitates dose escalation based on the response of the treatment. A moderate improvement was observed concerning dose escalation because FDG uptake did not show a high correlation with radio-resistant areas [33]. Vera et al. observed differences in FDG uptake and a decrease in proliferative activity during treatment in which they verified the feasibility of FDG imaging before and during radiotherapy [85].

The quoted studies did not compare their outcomes with pathological characteristics, as a consequence that the question of correlating pathology with an imaging tracer continues to arise. The ability of FDG-PET to measure proliferative activity in response assessment is useful because proliferation characterizes viability, allowing FDG-PET to identify viable tissue areas. This marks the importance of the correlation between pathology and an imaging tracer.

Ki-67 Proliferation Marker and Automated Detection

A generally acknowledged molecular biomarker to assess proliferation in NSCLC is the Ki-67 protein. The corresponding Ki-67 labelling index (LI) defines the percentage of tumor cell nuclei that show immunoreactivity [49]. The Ki-67 protein is present in cell nuclei during all active phases of the cell division cycle. This characteristic makes the protein an appropriate marker for cell proliferation. However, since the Ki-67 antigen was also present in normal cells, the utilization of Ki-67 antibodies increased significantly in different types of neoplasms. The use of Ki-67 in the identification of proliferating cells in tumor tissue is beneficial, since Ki-67 immunostaining can be executed easily on histology sections of non-small cell lung cancer.

Studies have been performed to investigate the Ki-67 protein. Yamamoto et al. examined the correlation of radiotracer uptakes with Ki-67 immunohistochemistry in NSCLC and observed a significant correlation between FDG uptake and the Ki-67 labelling index [90]. Jakobsen et al. discussed the prognostic role of the Ki-67 labelling index (LI) in NSCLC patients. They reviewed the potential role of histological subtypes on the use of the Ki-67 labeling index of all studies that were performed from 2000 to 2012. It was difficult to compare studies with different patient populations and applied methodologies, but they concluded that no agreement was found on the significant influence of the Ki-67 labeling index [39]. In all studies, Ki-67 cut-off values were determined according to hot spots with a certain percentage of Ki-67 positive cells. This method caused a misleading Ki-67 LI due to heterogeneity of proliferating cells in tumors. A more robust method to assess the amount of Ki-67 positive cells in histological subtypes is to analyze whole subtypes, instead of hot spots, with an automated approach to detect proliferating cells.

The assessment of Ki-67 proliferative activity in tumor slices via automated detection is a staple of research into breast cancer dynamics [28, 43, 62]. Mohammed et al. explored the difference between automated detection of the Ki-67 LI versus visual scoring and compared their accuracies. Automated detection of Ki-67 proliferating cells was accomplished by a nuclear scoring algorithm, deriving target areas with accompanying counting scores. Results showed that automated scoring was in good agreement with visual scoring However, visual scoring was better in predicting cancer survival, but benefits of automated assessment show reduced workload compared to manual counting and improved accuracy. Despite, validation of the automated assessment is required [62]. Konsti et al. performed a similar study, emphasizing the importance of automated assessment being an independent predictor of survival in breast cancer [43]. Other studies demonstrated the use of computer assisted image analysis on digitized slides of human breast cancer, substantiating the fact of improved accuracy compared to manual counting. Furthermore, the reproducibility of computer assisted assessments is enhanced too. Fasanella et al. mentioned an important statement that it is not realistic to utilize cut-off values in low, intermediate and high categories of proliferative activity. This is because cut-off values are varying among the type of antibodies and the type of assessment [28]. This again shows the benefit of automated assessment over manual assessment.

Limited studies of automated detection algorithms have been undertaken for NSCLC. The first of these limited studies was undertaken by the group of Liu et al. in which they automatically quantified the Ki-67 index of neuroendocrine tumors of the lung. The ImageScope Nuclear v9 algorithm software was used to determine the Ki-67 proliferation index and mentioned the role of Ki-67 as an effective diagnostic marker for neuroendocrine tumors [51].

A different molecular biomarker to assess tumor proliferation was used by Chen et al.: 3'-deoxy-3'[^{18}F]-fluorothymidine, [^{18}F]-FLT. They hypothesized that high FLT uptake values correspond to high proliferation areas in tumors. However, a significant positive correlation was not found [18]. One potential factor explaining this included the fact that the Ki-67 LI represents the level of proliferation for only part of the tumor, while the SUV-max corresponds to the whole tumor. The proposed study will further explore this phenomenon through investigating the number of proliferating cells immunostained with Ki-67 and correlating them to observed FDG concentrations in tissue slices.

Biologic Correlates with FDG

Zhao et al. explored other biological correlates with FDG than proliferative cells. They demonstrated that the distribution of FDG within the tumor corresponds to glucose transporters and hexokinase-II (HK-II) [93]. Glucose transporters facilitate the transport of glucose across the plasma membrane [38] where hexokinase-II strongly regulates glucose metabolism with a raised level in cancer cells [58]. Enhanced and thus altered expression levels of glucose transporters and hexokinase-II, stimulated by hypoxic regions, were supposed to contribute to the elevated FDG accumulation in the central tumor showing a heterogeneous distribution. Moreover, FDG uptake was favored in hypoxic regions compared to normoxic regions. Furthermore, FDG uptake levels were enhanced in HIF-1α (hypoxia-inducible factor 1-α) regions. HIF-1α is responsible for upregulating genes that play a role in cell survival, angiogenesis and resistance to radiotherapy. Mamede et al. substantiated the claim that a close correlation exists between the expression of Glut-1 and HK-II and FDG uptake in NSCLC. Furthermore, they illustrated that expression of the proliferating cell nuclear antigen (PCNA) correlated with FDG uptake. In addition to that, nonmalignant tissue regions also show increased FDG uptake [54], concluding that FDG is not a candidate for differentiating malignant and nonmalignant lesions of the lungs. The group of Ahuja et al. immunohistochemically investigated the expression of cell membrane glucose transporters and suggested that high FDG uptake values indicate more metabolically active lesions which are at increased risk for relapse irrespective of the clinical stage [3].

The diverse outcomes of the above mentioned studies indicate that FDG uptake in tumor tissue is influenced by several biological characteristics. An important note is that the performed studies are based on patient studies with *in vivo* FDG measurements in clinical PET scanners. The proposed study will measure response in a small-animal PET scanner by the use of *ex vivo* experiments of tumor specimens.

Ex vivo experiments

The conventional cell line technique in which cell cultures are established enable proliferation of cells within a certain medium [82], but have limited predictive value with respect to the biological characteristics of specific cancer types. Permanent modifications that occur in cell line generation, together with the fact that cell lines do not represent the full heterogeneity of NSCLCs, make the conventional cell line techniques inappropriate in the assessment of tumor responses [37].

Research is being done on novel approaches in which short-term primary cultures were obtained from the tumor which could accurately represent the biological behavior of the original tumor. In urothelial carcinomas (UC) of the bladder, a new culturing system was developed by Seifert et al., allowing the successful growth of UC. In addition to previous strategies, a hypoxic environment was created which increased the tumor cell growth rate. Subsequently, the addition of certain media to the culturing conditions led to growth and survival of UC cultures [73]. Sato et al. created an organoid culture platform which could be implemented in pathological examinations of the intestinal tract. The organotypic tumor slices reflected more precise the intestinal epithelium than in previous cancer cell lines [72]. The derivation of patient-derived xenograft mouse models in cancer research was a third example of a strategy for primary tumor culturing. Hidalgo et al. utilized this concept to study tumor response to drug treatments, however these technique used an *in vivo* platform whereupon the added value of *ex vivo* platforms was highly accentuated [37].

Naipal et al. created a method in which they optimized conditions of existing organotypic tumor slice techniques that permit *ex vivo* culturing of primary breast cancer to use in the assessment of tumor responses to anti-cancer drugs. They were able to maintain the desired tissue cultures for a minimum of 7 days while preserving cell proliferation, viability and the morphology of the tissue. Tissue slicing technologies were examined, growth medium was optimized and an optimal environment was created to enhance the exchange of nutrients. The authors stated that the developed culture system offers a relatively fast method to identify therapy-resistant tumors which could lead to an increasing benefit of treatment optimization and the reduced side effects [63].

In the proposed study, the organotypic tissue slice model will be applied for NSCLCs which

was proven feasible. This allows a useful *ex vivo* platform to investigate FDG uptake with pathological characteristics by the use of PET imaging, addressed in the following section.

PET Imaging

Positron emission tomography (PET) is one of the main modalities for tomographic imaging in nuclear medicine [19], capable of measuring positron emitting isotopes concerning their spatial distribution and concentration in living subjects [76]. This property allows the determination of intra-tumor heterogeneity which is of high importance in the assessment of diagnosis, therapy response and survival [27, 80]. Positron-emitting radionuclides attached to biological tracers are injected into the body and accumulate in certain tissue types based on appropriate receptors [36]. When a positron is emitted from the biological tracer, it will annihilate with an electron, resulting in the conversion of two annihilation photons with identical energies of 511 keV, traveling in opposing directions. Gamma-ray detectors are able to detect the annihilation photons within a very short time frame mentioning a coincidence event. By annihilation coincidence detection the localization of the origin of annihilation can be determined [19]. The performance of a PET scanner is characterized by spatial resolution, sensitivity, the system scatter fraction and the (noise equivalent) count rates [20, 71]. The spatial resolution of a PET scanner is described by the ability to accurate represent the unequal distribution of radioactivity in the object. It is officially defined as the ability of the scanner to differentiate two points in an image, expressed as a minimal distance [71]. The spatial resolution of a PET scanner is determined primarily by the detector element size [19]. Other impediments include the positron range effect and noncolinearity of annihilation photons which obviously affect the quality of imaging [22, 87]. According to Levin et al., the most dominant influence of spatial resolution on the system is the positron range effect [48]. Multiple scattering due to interaction with atomic electrons is responsible for the slowing down of positrons while travelling through tissue, eventually leading to annihilation with an electron. The travelled distance between the site of β^+ emission and the location of annihilation is called the positron range. The interaction with atomic electrons causes deviations in the travelling path of the positron, making the positron range an effective range. Since localization of the coincidence event is based on the annihilation location instead of the site of β^+ emission, the determined position does not correspond with the true position of the positron emission, creating an error which results in deterioration of the spatial resolution [71].

Response assessment in tissue samples by PET is limited by the resolution of the scanner since heterogeneity in the samples is spatially variant on a scale smaller than the scanner resolution. However, the development of microPET scanners have made it possible to non-invasively image biological functions in small animals [36]. Subsequently, microPET offers a high resolution, a high sensitivity and a good count rate performance for low doses of radiotracers [16]. About 10-15 years ago, many studies were done on the characteristics and performance evaluation of several small animal PET scanners [41, 42, 45, 76]. In the proposed study, the Inveon (Siemens) small-animal microPET scanner will be used whose performance was evaluated by Constantinescu et al. and Chatziioannou et al. [16, 20]. Techniques to improve spatial resolution of the Inveon microPET scanner through the use of 3D-printed tumor resembling phantoms have not been performed yet, introducing a whole new insight in the characterization of the Inveon microPET system.

A closely related imaging modality that holds the same ability to detect radiotracers as PET would be Single Photon Emission Computed Tomography (SPECT). However, studies have shown that the use of a clinical SPECT system with 511 keV collimators lead to reduced resolution and lower system volume sensitivity but that it varied between different cancer types. [14, 22, 55]. Due to availability of the Inveon microPET system and the preference of PET imaging above SPECT imaging concerning resolution and sensitivity, the microPET imaging modality was selected.

Phantom Experiments

Numerous phantom experiments have been performed on clinical PET scanners. The group of Wollenweber et al. utilized 3D-printed fillable phantoms that were used to examine the

detection limit of PET imaging. They mentioned the frequently seen concern about phantom designs often not reflecting the true nature [89]. In microPET systems, phantom experiments are accomplished with the generally known NEMA image quality phantom [6] and the Derenzo phantom [21]. These studies again show designs of phantoms which do not reflect true nature, but the extent to whether it is a limitation is dependent on the purpose of the study. According to the literature, the proposed study appears to be the first in using 3D-printed tissue like phantoms. Another limitation in phantom experiments could be the filling procedure. Since a 3D-printing concept will be used, the highly accurate manufacturing process together with freedom in design customization allows the creation of complex high spatially encoded geometries in which the filling procedure can be optimized and the phantoms can easily resemble the tumor slice heterogeneous characteristics.

Conclusion

Heterogeneity of Non-Small Cell Lung Cancers may cause reduced local tumor control and poor treatment outcomes. The different biologic characteristics within a tumor respond differently creating radio-resistance to radiotherapy. Through selectively redistributing the dose and escalating the dose to the poorly responding regions during the course of the treatment, normal tissue can be spared, leading to a more effective treatment of the tumor and increase in local tumor control. However, the challenge remains to validate the correlation of the imaging target with a local biological trait. The introduction of the exPET study will investigate this validation by carrying out *ex vivo* experiments of NSCLC tissue specimens immunostained with the proliferation marker Ki-67. The *ex vivo* culturing platform will allow the assessment of FDG uptake measured by the Inveon microPET scanner. The number of proliferating cells will be assessed by an automated detection algorithm, which was proven to have increased accuracy in heterogeneous breast cancer by Mohammed et al. The proposed study aims to substantiate this claim for NSCLC patients in particular. Owing to the group of Naipel et al., *ex vivo* experiments can be accomplished for NSCLC specimens, enabling the measurement of FDG uptake *ex vivo*. *Ex vivo* culturing platforms are of great value in the investigation of drug response, mentioned by Hidalgo et al. The FDG uptake will be measured in the Inveon microPET system since normal PET scanners are limited in their spatial resolution to assess heterogeneity on such a small scale. 3D-printed phantoms will be used to verify the capability of the Inveon microPET scanner to detect small differences in FDG concentration. The tissue like 3D-printed phantoms are beneficial since they will serve as a ground truth. By the assessment of available reconstruction algorithms on the Inveon microPET scanner, the ideal method in exploring tumor heterogeneity will be developed, leading to insight into the development of FDG-PET during radiotherapy treatment in NSCLC patients.

2

Characterization of the Inveon microPET System by the use of 3D-printed Phantoms

Abstract

Assessment of heterogeneity in tumor specimens in daily clinical PET scanners is hampered by the resolution of the PET scanner. The development of a microPET system has created the possibility to investigate uptake of 2-deoxy-2-(^{18}F)fluoro-D-glucose (FDG) in small animals. However, phantom experiments in which tumor slice heterogeneity is mimicked has not been performed yet. In this study, the development of novel 3D-printed phantoms gave insight into a new field of characterization of the Inveon microPET scanner. The capability of the microPET scanner to distinguish FDG concentrations at a small scale was investigated and maximized by the implementation of a deblurring technique. The performance of different image reconstruction algorithms was compared. The deblurring technique was applied on the microPET results for the most appropriate reconstruction algorithm. The presented work has shown the ability of the deblurring technique to improve the contrast and transition between phantom features. The most remarkable contribution of the deblurring technique is the correction for spillover effects, leading to improved differentiation of different FDG values in small features, allowing a more accurate representation of measured objects.

Keywords — 3D-printed phantoms - deblurring technique - microPET - FDG

2.1. Introduction

Positron Emission Tomography (PET) is a functional imaging modality capable able of measuring the spatial distribution and concentration of positron emitting isotopes. The positron emitting tracer 2-deoxy-2-(^{18}F)fluoro-D-glucose (FDG) is a glucose analogue widely used in PET imaging [60] which application is found in measuring treatment response in tumor regions [74]. Response assessment in tumor specimens by PET is limited by the resolution of the scanner since heterogeneity in the specimens is spatially variant on a scale smaller than the scanner resolution. The development of microPET scanners have made it possible to non-invasively image biological functions in small animals [36]. Subsequently, microPET offers a high resolution, a high sensitivity and a good count rate performance for low doses of radiotracers [16]. Many studies have been performed on the characteristics and performance evaluation of several small animal PET scanners [41, 42, 45, 76]. However, a capability study to accurately detect FDG differences in small tumor specimens was not performed yet. This approach will be addressed by the development of 3D-printed phantoms in order to characterize the Inveon microPET system. 3D-printing of phantoms has a number of benefits that include high design complexity and fast production times. The present work employs on these benefits to develop a set of novel PET phantoms that mimic the structure of tumour tissue slice heterogeneity.

The performance of a PET scanner is characterized by spatial resolution, sensitivity, system scatter fraction and the (noise equivalent) count rate [20, 71]. The spatial resolution of a PET scanner is described by the ability to accurately represent unequal distributions of radioactivity in an object. Physical limitations of PET spatial resolution include the positron range and noncolinearity of annihilation photons, the latter caused by the residual momentum of the annihilated electron-positron pair, emitting photons with an angle deviant from the expected 180° [16]. The error resulting from a shifted line of response with respect to the true point of annihilation degrades PET spatial resolution. The first limitation is caused by multiple scattering due to interaction with atomic electrons, responsible for the slowing down of positrons while travelling through tissue, eventually leading to annihilation with an electron. The travelled distance between the site of β^+ emission and the location of annihilation is called the positron range. The interaction with atomic electrons causes deviations in the travelling path of the positron, making the positron range an effective range. Since localization of the coincidence event is based on the annihilation location instead of the site of β^+ emission, the determined position does not correspond to the true position of the positron emission, creating an error responsible for deterioration of PET spatial resolution [71].

Images of radiotracer distributions are acquired by tomographic image reconstruction. Reconstruction algorithms include analytic methods in which a direct mathematical solution is used and iterative methods which utilize a more complex mathematical solution [4]. In 2D PET data acquisition, data is collected from a single slice in which septa serve to reject annihilation photons originated from random coincidences and scattering events. Data reconstruction can be performed for both analytic and iterative methods concerning filtered back projection (FBP) and ordered subsets expectation maximization in 2D (OSEM2D), respectively. 3D PET data is reconstructed from projection data available from oblique planes iteratively by 3D ordered subsets expectation maximization (OSEM3D) [19, 91].

Image reconstruction results in PET images consisting of a stack of image planes comprising an image volume in which each voxel intensity indicates the amount of radioactivity. In the ideal case, the voxel intensity corresponds directly to the amount of radioactivity in the accompanying feature. Physical limitations impede this, but attenuation and scatter corrections allow partial compensation. Despite this, errors in ascribing activity concentrations to small feature volumes are still present due to image sampling. One limitation is the definite volume of a PET voxel. Image sampling in combination with physical limitations of the scanner together blur the images. This effect is explained by partial volume effects and lead to over- and underestimations in quantitative assessments [7].

The presented work characterizes the Inveon microPET scanner by the use of 3D-printed phantoms which mimick tumor tissue heterogeneity. The development of a deblurring technique is used to address the spillover effect associated with microPET image reconstruction. An overview of the phantom development, design requirements and 3D-printed technique can be found in section 2.2. The theoretical explanation concerning the deblurring technique is outlined in section 2.2.8. A comparison of the deblurred PET data with original PET data is outlined in section 2.3. Finally, a discussion and an overall conclusion of the presented work can be found in section 2.6.

2.2. Methods

2.2.1. Inveon microPET

The Siemens Inveon microPET scanner (Siemens Medical Solutions) is a circularly oriented scanner consisting of 16 detector modules, each composed of four detector blocks oriented in the axial direction. A total of 25,600 lutetium oxyorthosilicate (LSO) detector crystals are organized in a 16.1 cm ring diameter. The detector blocks are composed of a 20 x 20 array of 1.59 mm x 1.59 mm x 10.00 mm LSO crystals. Detector modules are arranged in opposing directions to ensure time coincidence, creating an effective axial field of view of 12.7 cm and a transverse field of view of 10.0 cm. Each detector within the scanner is optically connected to a position-sensitive photomultiplier tube by the use of a tapered multiple-element light guide. Acquired PET data can be arranged into two-dimensional sinograms or into three-dimensional sinograms with varying span numbers and ring differences. Several image reconstruction algorithms are available in the Inveon software including the filtered backprojection (FBP) and 2D ordered-subset expectation maximization (OSEM 2D) resorted by the Fourier rebinning algorithm if data is sorted into 2D sinograms. When data is sorted into 3D sinograms, the images can be reconstructed by the use of the 3D ordered subset expectation maximization (OSEM 3D) algorithm with or without an additional maximum a posteriori (MAP) algorithm [20, 47, 65].

2.2.2. Phantom Development

Phantoms were developed to create fillable tumor tissue like geometries for measurements of detectability in PET imaging. The phantoms developed for the experiments were 3D-printed at the Dienst Elektronische en Mechanische Ontwikkeling (DEMO) group at the TU Delft. 3D-printing is a very accurate manufacturing process that enables the creation of objects one layer at a time [70]. High accuracy manufacturing from a functional material enables the creation of extreme complex geometries. The freedom of design customization is highly beneficial in the phantom development for the proposed study since the phantoms must resemble the tumor slice dimensions and must reflect tumor heterogeneity as much as possible. The phantoms are square geometries of 10.0 x 10.0 x 1.0 mm with a varying internal structure. This requirement is put into practice by printing blocks of varying heights in random and fixed gradients with respect to each other. A required characteristic of the printed phantoms includes an inlet and outlet for the injection of FDG into the phantom. Each phantom inlet and outlet are composed of thin tubes of 10 mm and a diameter of 1.8 mm. The phantom was filled with FDG and air was pushed out, performed at an angle of approximately 45 degrees in a phantom holder. Another important requirement in the phantom design was the minimization of material around the central part of the phantom to prevent annihilation of positrons in surrounding material and affecting the PET outcome. This is the argument for the distance of 10 mm from the phantom to the inlet and can be observed in figure 2.4. However, this design led to a fragile phantom. Multiple designs have been printed to test for brittleness, eventually resulting in the phantoms shown in figure 2.4a and 2.4.

Table 2.1: Overview printed phantom names and dimensions

Phantom Name	Geometry
Snake	Tubes
4x4	4x4 blocks
2x2	2x2 blocks
H100	Homogeneous 1 mm
H25	Homogeneous 0.25 mm

2.2.3. Phantom Designs

Table 2.1 shows an overview of the printed phantoms with their names used in this study and their accompanying geometry. The first phantom that was printed was the 4x4 phantom. The internal structure of the 4x4 phantom was composed of 16 blocks of 2.5 x 2.5 mm. The heights of the blocks varied from 0 to 1 mm with steps of 0.25 mm, shown in figure 2.2a. The design of the internal structure of the 4x4 phantom was chosen to contain fixed gradients and random gradients in order to examine differences in spillover effects within the phantom. In other parts of the phantom random gradients are present with varying step sizes. The second phantom was composed of a 2x2 array to mimic a lower resolution version of the 4x4 array, and possible tumors with lower variation of heterogeneity. This phantom contains four blocks in total of different height, again varying from 0 mm to 1 mm with steps of 0.25 mm, shown in figure 2.2b. Consequently, two homogeneous phantoms were printed

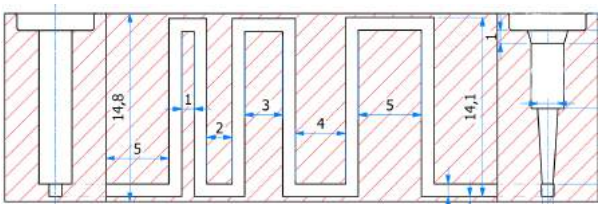

Figure 2.1: Snake dimensions

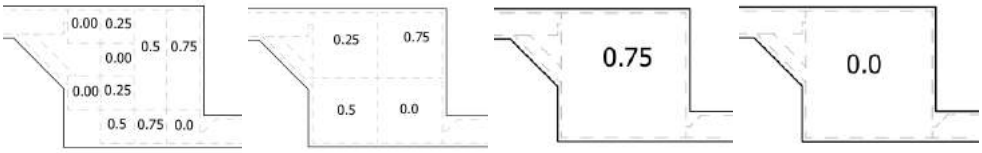

(a) 4x4 (b) 2x2 (c) H25 (d) H100

Figure 2.2: Phantom internal dimensions

with a height of 1 mm and 0.25 mm respectively (figure 2.2c and 2.2d). At last, a model phantom was created which served as a snake phantom which resembled a snake geometry (figure 2.1) with increasing distances between vertical segments. The exact purpose of this phantom will be explained later on. Criteria on the minimum thickness of the phantom walls needed investigation in order to guarantee robust walls. Additionally, the optimal printing orientations have been examined to prevent printing failure or breaking of the phantom. The determined minimum thickness of the phantom walls is 300 μm and the phantom ceiling had a thickness of 400 μm.

2.2.4. 3D-printing

The printing process is called Stereolithography (SLA) Direct Light Processing (DLP). In this technique, the fabrication platform was submerged in the liquid photocurable resin in a 'bat' configuration, shown in figure 2.3. Phantom construction occured layer-by-layer by photopolymerization which was spatially guided by a digital light projector [86]. By the use of a Digital Mirror Device (DMD), shown in figure 2.3, a single image of each layer was illuminated on the platform at once. The use of a digital screen is responsible for the composition of square pixels in each image, in the end leading to a layer composed of voxels [31]. The printing performance of the machine is dependent on the characteristics of the printed object together with the resin properties and layer thickness [86]. The machine characteristics of the Envisiontec Perfactory Mini include a XY resolution of 33 μm or 19 μm. The specific profile used to overlay the pixels leads to a XY resolution of 17 μm x 10 μm. The voxel resolution in Z is 15 to 150 μm. The projector resolution is 1920 x 1200 pixels [24].

2.2.5. Phantom Experiments

The phantom experiments were undertaken at the Department of Radiology and Nuclear Medicine at the Erasmus MC. Beforehand, x-ray CT scans were taken of all empty phantoms. Filling of the phantoms was accomplished by the use of 3D-printed phantom holders. The phantom holders were specially designed to fill the phantoms at an angle of 45°. Small screws were used to close the inlet and the outlet

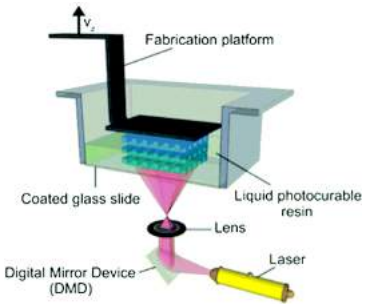

Figure 2.3: Visualization of the SLA-DLP printing technique [86]

Table 2.2: Activity concentrations and injected volumes in the phantom experiments

	Snake	**4x4**	**2x2**	**H100**	**H25**
Start Act. Conc. [Bq/ml]	40.6E+05	40.0+E05	72.4E+05	72.4E+05	40.0E+05
Decay time [min]	9	83	109	61	182
Decay-corr. Act. Conc. [Bq/ml]	38.4E+05	23.7E+05	36.4E+05	49.3E+05	12.7E+05
Volume phantom [ml]	0.108	0.099	0.125	0.177	0.088

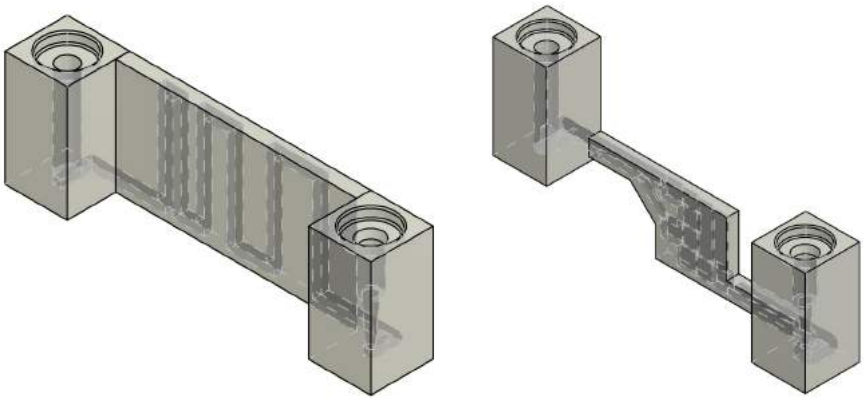

(a) Snake phantom (b) Phantom

Figure 2.4: Phantom designs

of the phantom, making the phantom airtight. The phantom was aligned with the microPET scanner in the axial direction and was attached to a foam bed before starting the acquisition. Afterwards, an x-ray CT scan was taken of the filled phantom to check for correct filling of the phantoms. The injected activity concentration, the volume and decay corrected activity concentrations are listed in table 2.2.

PET Acquisition Parameters
With the microPET scanner an acquisition time of 1800 seconds was used for the FDG filled phantoms with a photopeak at 511 keV, an energy window of 350 - 650 keV and a timing window of 3.432 ns. In all reconstruction algorithms, no attenuation correction was applied. The images have been reconstructed into 256 x 256 matrices in the Intel/VAX 4-byte float data type.

2.2.6. PET Data Assessment

PET data was stored in DICOM. The DICOM files were imported into Matlab, 2018. Volumetric data was provided in a 256 x 256 matrix in a stack of 159 planes with a voxel size of 0.388 x 0.388 x 0.796 mm. Pixel intensity values per plane of the raw PET data were converted to activity concentrations in Bq/ml by the extraction of the rescale slope and rescale intercept from the DICOM header. The rescaling is implemented as follows:

$$A_{pixel} = a \cdot PIV + b \tag{2.1}$$

where PIV is the original Pixel Intensity Value of the PET data. a is the rescale slope and b is the rescale intercept. A_{pixel} is the activity concentration in Bq/ml [40, 57]. Of the PET data a selection of planes was chosen for each phantom which hold the volume of interest. In order to fully enclose the volume of interest with a height of 1 mm, four planes each with a height of 0.388 mm were selected. The four planes of interest were selected by calculating the mean activity concentration present in the phantom per plane. The four slices with the highest activity concentrations per plane were selected and visually checked for reliability for further assessment. Inspection of the FBP data showed negative pixel values in the background of the data. These values were all set to zero in order to proceed the analysis.

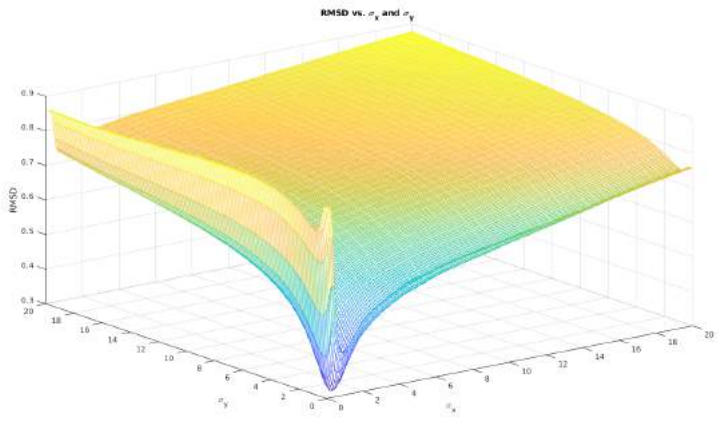

Figure 2.5: Root Mean Square Difference vs. σ_x and σ_y

2.2.7. Determination of Activity Concentrations

Measured phantom

Pixel activity concentrations of the four planes were summed, creating a 2D image of the PET data. By multiplying the activity concentrations by the volume of a voxel and dividing by the voxel's length and width, activity values in Bq/cm^2 were acquired. This approach was explained by the following formula:

$$A_{measured} = \frac{\sum_{n=1}^{4} A_{pixel} \cdot V_{voxel}}{l_{pixel} \cdot w_{pixel}} = \sum_{n=1}^{4} A_{pixel} \cdot h_{voxel} \tag{2.2}$$

where A_{pixel} is the activity concentration in a pixel in Bq/ml per plane, V_{voxel} is the volume of a voxel in ml, n equals the plane number, h_{voxel} is the height of one voxel in cm and l_{pixel} and w_{pixel} indicate the length and width of a pixel in cm.

Computational phantom

A computational phantom was created containing the true activity values in order to perform quantitative comparison with the measured PET results. The activity concentrations of the computational phantom equal the decay corrected injected activities in the phantom. This calculation was made for each phantom. The true activity concentration was approached by the following formula:

$$A_{true} = A_{injected} e^{-\lambda t} \cdot h_{comp} \tag{2.3}$$

where A_{true} is the true activity concentration based on the injected activity concentration $A_{injected}$, of which the values are shown in table 2.2. λ is the decay constant, t the elapsed time and h_{comp} is the height of the compartment in cm in which activity is present.

2.2.8. Image Post-Processing

Due to the limitations in detection, positron range, gamma-ray scattering and lost events, the reconstructed image estimates are not an exact replication of the object. These effects result in a "blurred" estimate of the object to be recovered and can be modelled as:

$$G(u,v) = H(u,v)F(u,v) + N(u,v)$$

in which $G(u,v)$ defines the blurred image, $F(u,v)$ represents the real, but unknown image and $H(u,v)$ stands for the blurring kernel. $N(u,v)$ describes the additive Poisson noise.

A deblurring technique was developed in order to correct for part of the deteriorating effects. The snake phantom served as a training object in order to estimate the point spread function of the system. Figure 2.1 shows the dimensions of the snake phantom. The distance between the vertical segments increases with 1.0 mm for each new segment. The purpose of the horizontal space between the lines of the snake phantom was to assess image resolution improvement after the implementation of the deblurring technique. The estimated PSF was applied in the restoration process of the reconstructed images.

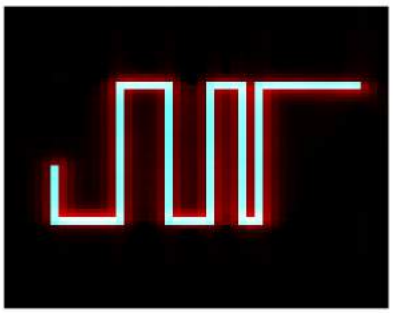

Figure 2.6: Overlay computational phantom with measured PET phantom

Estimation of the Point Spread Function

The first step of the PSF estimation was the implementation of a computational version of the snake phantom. The computational snake phantom possesses the dimensions of the true snake phantom. Normalized two-dimensional cross-correlation was computed between the computational object and the measured PET data in order to accurately align the two objects. The normalized 2D cross-correlation function provided an offset in the x- and y-direction on which the location of the computational phantom could be adjusted in order to achieve the best alignment between the two objects. The result can be observed in figure 2.6.

Of the computational snake phantom, a manually blurred version was created by the use of a Gaussian smoothing filter. The manually blurred image must resemble the real PET data as much as possible. Since the extent of blurring in measured PET data was assumed to be anisotropic, a two-dimensional Gaussian smoothing kernel was used, called an axis-aligned anisotropic Gaussian filter, containing varying standard deviations along row and column dimensions. To assess the difference between the two data sets the Root Mean Square Difference (RMSD) was used [11]:

$$RMSD = \sqrt{\frac{\int\int |I_n(x,y) - E_n(x,y)|^2 dxdy}{\int\int |I_n(x,y)|^2 dxdy}} \tag{2.4}$$

in which $I_n(x,y)$ equals the normalized version of the known object and $E_n(x,y)$ is the normalized version of the estimated image. The degree of blurring is determined by the standard deviation of the Gaussian filter. The 2D Gaussian standard deviations were swept over a range of zero to twenty in steps of 0.1, with an additional range for further optimization of $\pm$ 0.3 with steps of 0.01 and the resultant computational image was assessed with respect to the measured PET data. The optimal filter dimensions were given at the absolute minimum of the calculated RMSD. The result is shown in figure 2.5. Convolution of the computational phantom with the anisotropic Gaussian filter (with optimized dimensions) resulted in a (manually) blurred version of the computational phantom, observed in 2.7b.

The blind deconvolution algorithm in Matlab was used to deblur the manually blurred image and to reconstruct the PSF belonging to the restored image. From the standard deviations of the 2D Gaussian filter, the dimensions of the microPET PSF were determined. The dimensions of the PSF served as the dimensions of the initial estimate of the PSF filled with ones. By deconvolving the initial estimate of the PSF with the manually blurred image, the likelihood that the restored image was an instance of the manually blurred image was maximized. Since zero knowledge is available about the distortion of the image, this algorithm effectively determines the PSF based on an initial guess. The blind deconvolution algorithm is an iterative process, for which the optimum number of iterations was determined in order to achieve the most accurate deblurring result. By iteratively check the RMSD between the restored image and the computational phantom, the optimal number of iterations was found at the lowest RMSD. This number of iterations was used in the blind deconvolution algorithm together with the manually blurred image and initial PSF estimate. The result comprised the restored image and a reconstructed PSF.

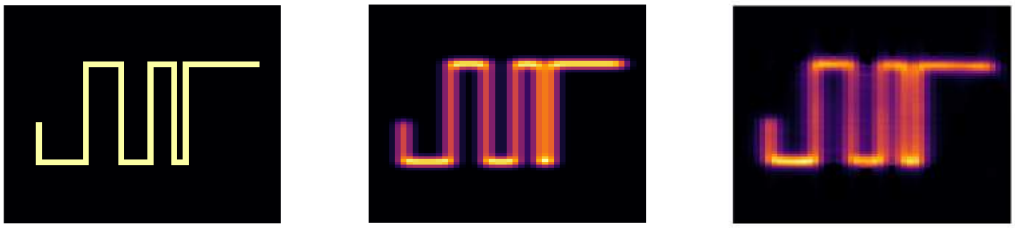

(a) Computational snake (b) Manually blurred snake (c) PET data snake

Figure 2.7: Manual blurring of the computational phantom, compared to real data

Image Restoration

Deblurring of the other phantoms was executed by the Lucy-Richardson deconvolution algorithm. To improve the restoration process, several parameters were added. The number of iterations was set to the above mentioned optimized number of iterations. A fundamental problem, however, in the attempt to deblur the data is noise amplification. By increasing the number of iterations, the deblurred image can exhibit artifacts which do not represent the actual structure in the original image. To overcome this problem, a damping parameter was used in order to limit the deviations in regions of the restored image and the original image. Afterwards, renormalization of the data was performed in order to keep the total amount of activity equal before and after the deblurring step.

2.2.9. Assessment of Reconstructed Image Quality

The performance of the deblurring technique was assessed by three figures of merit composed of the contrast, the signal to noise ratio and the RMSD (equation 2.4) of the original data and the deblurred data. The individual features in the heterogeneous phantoms were numbered in order to easily compare them, shown in table 2.3a and 2.3b.

Table 2.3: Numbering of phantom compartments

(a) Numbering 2x2 phantom

11	12
21	22

(b) Numbering 4x4 phantom

11	12	13	14
21	22	23	24
31	32	33	34
41	42	42	44

The contrast is defined as:

$$C = \frac{\mu_1 - \mu_2}{\mu_1 + \mu_2}$$

in which μ_1 and μ_2 stand for the mean values of two different features within the phantom. By comparing the contrast between features to the contrast of the features in the computational phantom, a relative contrast ratio results [11]:

$$\frac{C_m}{C_c}$$

.

In the heterogeneous phantoms, contrast was examined between two features within the phantom. The internal arrangement creates interesting contrast ratios to compare. Figure 2.8 shows the feature pairs of which the relative contrast ratio were determined. In each subfigure, the colored contours indicate the comparison of two feature pairs which possess the same ratio which should result in the same relative contrast. Captions below the subfigures indicate the concerned ratios. The same was applied for the 2x2 phantom, shown in figure 2.9. For the homogeneous phantoms, contrast was assessed by comparing the phantom ROI with a region in the background, visually depicted in figure 2.10 for the H100 phantom and figure 2.11 for the H25 phantom.

The Signal-to-Noise Ratio (SNR) was used to assess the amount of noise present in a feature. The SNR is calculated as follows:

$$SNR = \frac{\mu}{\sigma}$$

(a) 0:1 (b) 0:0.5 (c) 1:1 (d) 1:2 (e) 1:4 (f) 2:3 (g) 3:4

Figure 2.8: Contrast comparisons in the 4x4 phantom

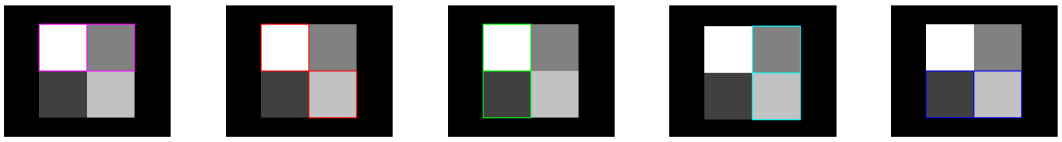

(a) 1:2 (b) 1:3 (c) 1:4 (d) 2:3 (e) 3:4

Figure 2.9: Contrast comparisons in the 2x2 phantom

in which μ equals the mean and σ stands for the standard deviation of the pixel values in the feature [11].

Line profiles were analyzed across phantoms in which the raw PET data and deblurred PET data was compared to the true activity values in the phantom. For all line profiles, the blue line indicates the true activity values of the phantom. The red line indicate the raw PET data of the concerned phantom. The green line shows deblurred data of the concerned phantom for the OSEM3DMAP algorithm. All line phantoms were drawn across the center region of the phantom or segments.

2.2.10. Image Post-Processing

The deblurring technique was applied on the snake phantom data of all reconstruction algorithms. The reconstruction algorithm which showed the most promising result of the deblurring technique was selected for further analysis. Consequently, the remaining phantoms were deblurred by the deblurring technique and the outcomes were examined.

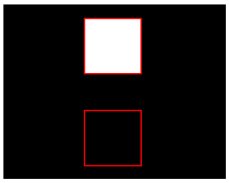

Figure 2.10: Contrast comparison in the H100 phantom

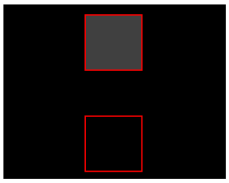

Figure 2.11: Contrast comparison in the H25 phantom

2.3. Results

Results concerning the phantom experiments will be exemplified based on increasing complexity of the phantoms, starting with the homogeneous phantom of 1 mm, followed by the 0.25 mm thick homogeneous phantom, then the 2x2 phantom and at last the 4x4 phantom. This is the fixed structure that will be maintained in the upcoming results.

2.3.1. CT Images

Preliminary to the phantom PET experiments, a CT scan was acquired of all empty phantoms to check the internal geometry. Afterwards, a CT scan was acquired of the FDG filled phantoms to check for air bubbles. Figures 2.12, 2.13, 2.14, 2.15, and 2.16 show the CT images of each phantom in their empty condition, a side view and the FDG filled version of the phantom. The CT scans were extensively inspected on the presence of air bubbles and were proved to be qualified for analysis.

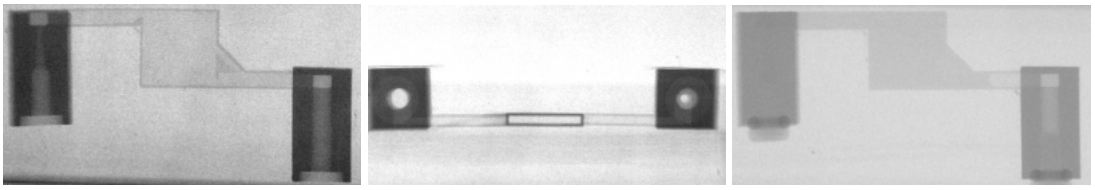

(a) CT H100 phantom empty (b) CT H100 phantom side view (c) CT H100 phantom filled

Figure 2.12: CT images of the empty, side view and filled H100 phantom

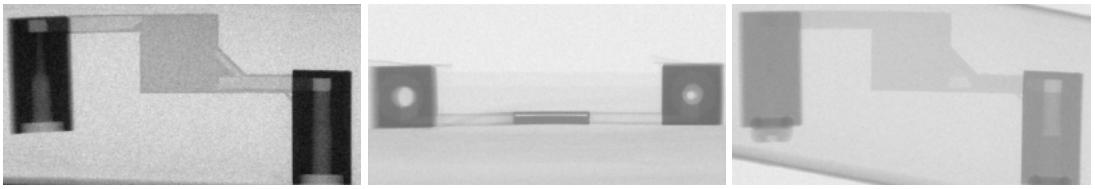

(a) CT H25 phantom empty (b) CT H25 phantom side (c) CT H25 phantom filled

Figure 2.13: CT images of the empty, side view and filled H25 phantom

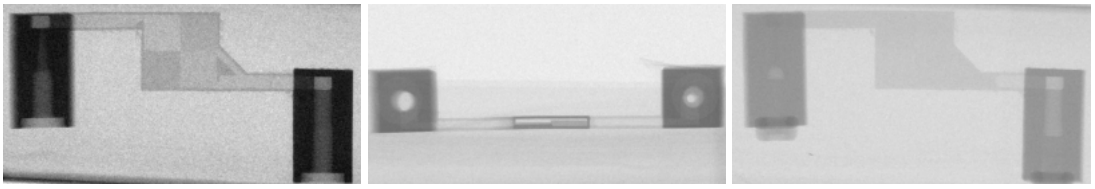

(a) CT 2x2 phantom empty (b) CT 2x2 phantom side view (c) CT 2x2 phantom filled

Figure 2.14: CT images of the empty, side view and filled 2x2 phantom

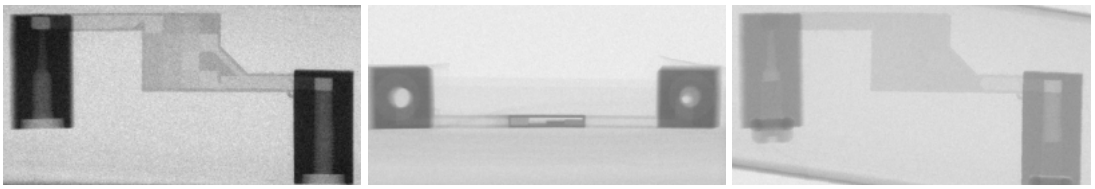

(a) CT 4x4 phantom empty (b) CT 4x4 phantom side view (c) CT 4x4 phantom filled

Figure 2.15: CT images of the empty, side view and filled 4x4 phantom

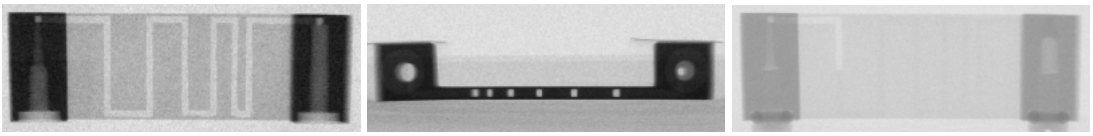

(a) CT snake phantom empty (b) CT snake phantom side view (c) CT snake phantom filled

Figure 2.16: CT images of the empty, side view and filled snake phantom

2.3.2. Image Post-Processing

A visual representation of the estimated PSF with the PSF values was shown in figure 2.17. Figure 2.18 shows the overlay of the computational phantoms with the measured PET phantoms.

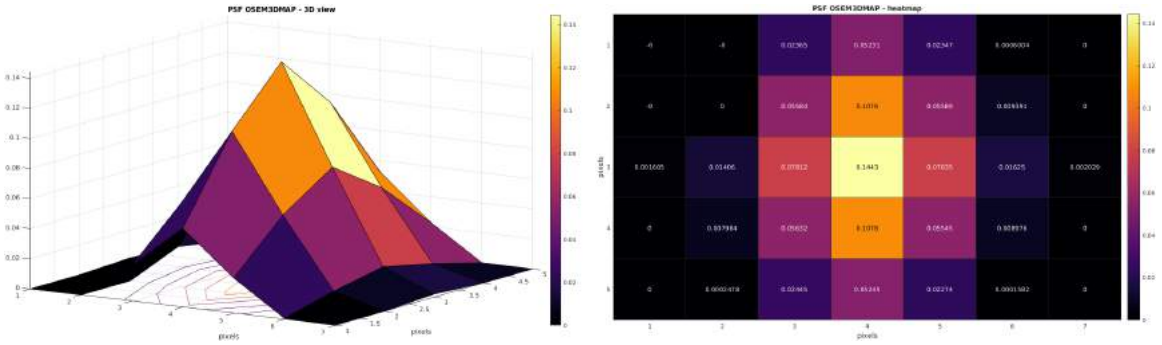

(a) 3D PSF (b) PSF values

Figure 2.17: Visualization of the Point Spread Function and its values

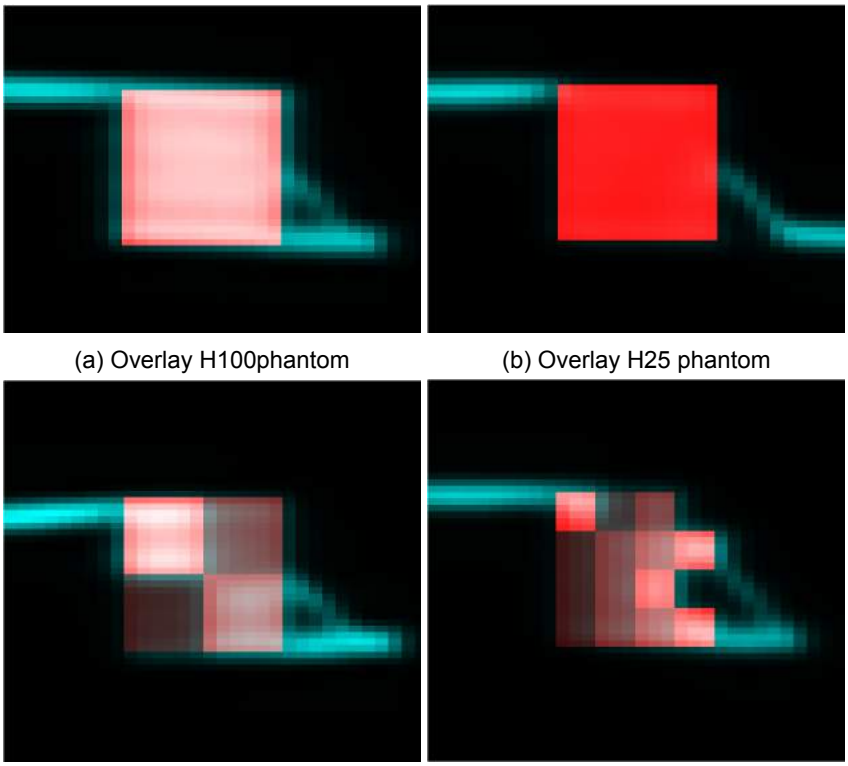

(a) Overlay H100phantom (b) Overlay H25 phantom

(c) Overlay 2x2 phantom (d) Overlay 4x4 phantom

Figure 2.18: Overlay of computational phantoms with measured phantoms

2.3.3. Homogeneous Phantom H100

The upcoming section discusses the result of the PET experiments for the homogeneous phantom of 1 mm. The maximum and mean activities are shown in table 2.4. Iterative algorithms perform considerable better in the reconstruction of the data than in the analytic algorithm, showing a difference of almost 25% for the mean activity. The standard deviation in the phantom is 1% to 2% lower in OSEM3D(MAP). Relative contrast ratios are shown in table 2.5, showing similar results for the reconstruction algorithms. The SNR of two regions of interest in the H100 phantom is shown in table 2.6. ROI 1 includes the whole phantom where ROI 2 includes a centered region in the phantom. In a larger region (ROI 1) the SNR is improved in OSEM3D algorithms. However, for smaller regions (ROI 2), FBP and OSEM2D perform better, showing a large difference in SNR compared to OSEM3D algorithms.

Table 2.4: Maximum and mean activity values per algorithm - H100 phantom

H100 phantom					
	True values	FBP	OSEM2D	OSEM3D	OSEM3DMAP
Max. Activity [Bq/cm^2]	4.93E+06	2.08E+06	2.41E+06	3.26E+06	3.46E+06
W.r.t. True Maximum (%)	100	42.2	48.9	66.2	70.2
Mean Activity [Bq/cm^2]	4.93E+06	1.76E+06	2.07E+06	2.75E+06	2.94E+06
W.r.t. True Mean (%)	100	35.6	42.0	55.7	59.6
Average SD/ROI [Bq/cm^2]	0	2.69E+05	2.88E+05	3.54E+05	3.74E+05
W.r.t. mean act. (%)	0	15.3	13.9	12.9	12.7

A comparison of line profiles across the H100 phantom of the original data and deblurred data with the OSEM3DMAP algorithm was show in figure 2.19 and 2.20. The horizontal line indicates a line profile in the axial direction of the scanner. The vertical line profile was made in the radial direction of the scanner. The raw PET data of the H100 phantom shows a smooth transition of activity values across the borders of the phantom. Deblurred data shows a sharper transition at the edges. The line profile in the radial direction (figure 2.20) shows less consistent values across the line.

Table 2.5: Relative contrast ratios for different algorithms per ROI - H100 phantom

H100 phantom				
	C_m/C_c			
	FBP	**OSEM2D**	**OSEM3D**	**OSEM3DMAP**
ROI	1,000	0,999	1,000	1,000

Table 2.6: Signal-to-noise ratios for different algorithms per ROI - H100 phantom

H100 phantom				
	SNR			
	FBP	**OSEM2D**	**OSEM3D**	**OSEM3DMAP**
ROI 1	14,171	15,204	16,089	16,868
ROI 2	58,196	61,828	30,625	42,941

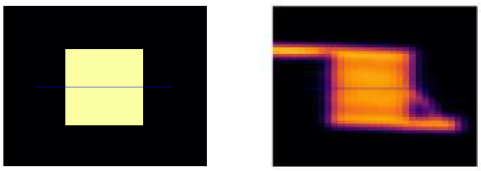

(a) Axial line - H100 true (b) Axial line - H100 raw

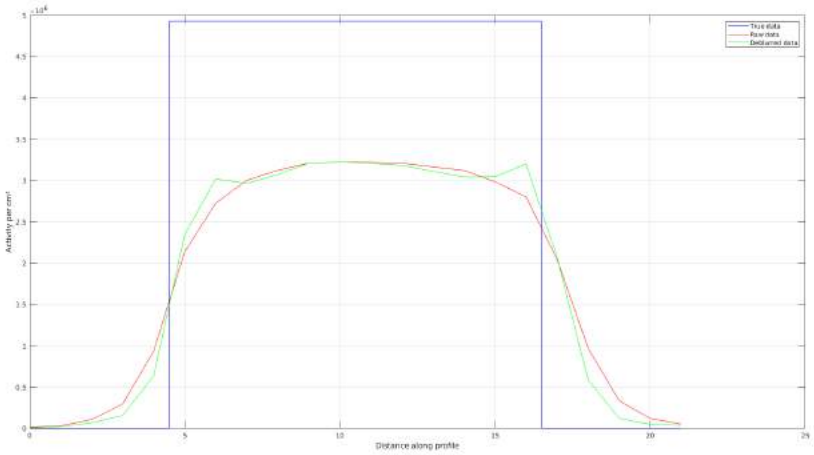

(c) Axial line profile H100

Figure 2.19: Axial line across phantom with line profile - H100

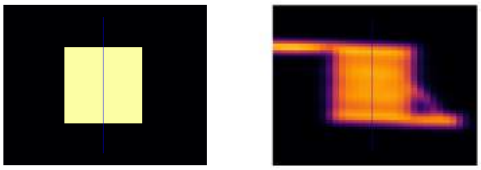

(a) Rad. line - H100 true (b) Rad. line - H100 raw

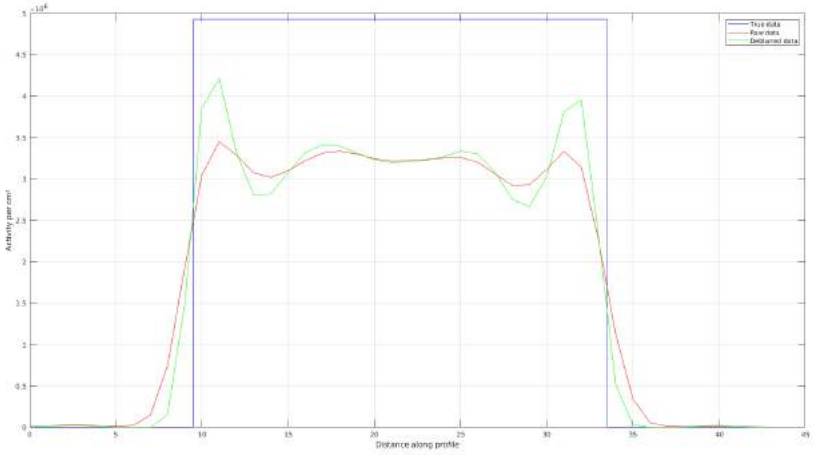

(c) Radial line profile H100

Figure 2.20: Radial line across phantom with line profile - H100

2.3.4. Homogeneous Phantom H25

The 0.25 mm homogeneous phantom shows a large difference between the maximum activity values between the reconstruction algorithms, ranging from 46% to 89% of the true value. However, for the mean activities this effect is not observed. An opposite result is seen in the standard deviation within the H25 phantom compared with the H100 phantom. Standard deviation is significantly higher in the OSEM3D algorithms. Relative contrast ratios in the H25 phantom show slightly worse contrast than in the H100 phantom. Improved SNRs are shown for both ROIs for the FBP and OSEM2D algorithm.

Table 2.7: Maximum and mean activity values H25 phantom for each reconstruction algorithm

H25 phantom					
	True values	FBP	OSEM2D	OSEM3D	OSEM3DMAP
Max. Activity [Bq/cm^2]	3,18E+05	1.47E+05	1.84E+05	2.85E+05	2.85E+05
W.r.t. True Maximum (%)	100	46.2	57.9	89.6	89.6
Mean Activity [Bq/cm^2]	3,18E+05	9.44E+04	1.10E+05	1.36E+05	1.32E+05
W.r.t. True Mean (%)	100	29.7	34.6	42.8	41.5
Average SD/ROI [Bq/cm^2]	0	1.29E+04	1.57E+04	2.85E+04	2.80E+04
W.r.t. mean act. (%)	0	13.7	14.3	21.0	21.2

The line profiles across the H25 phantom are shown in figure 2.21 and 2.22. In the radial line profile, extreme activity enhancements are observed close to the edges in the deblurred data. These enhancements are also observed in the raw data, but the deblurred data intensifies this effect. As in the H100 phantom, deblurred data shows sharper transitions at the edges of the phantom in the axial and radial direction.

Table 2.8: Relative contrast ratios for different algorithms per ROI - H25 phantom

H25phantom				
	C_m/C_c			
	FBP	**OSEM2D**	**OSEM3D**	**OSEM3DMAP**
ROI	0,981	0,998	0,999	0,999

Table 2.9: Signal-to-noise ratios for different algorithms per ROI - H25 phantom

H25phantom				
	SNR			
	FBP	**OSEM2D**	**OSEM3D**	**OSEM3DMAP**
ROI 1	10,759	10,064	6,277	6,217
ROI 2	21,110	19,963	14,089	14,496

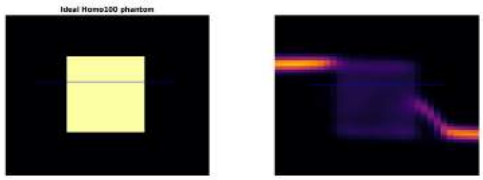

(a) Axial line - H25 true (b) Axial line - H25 raw

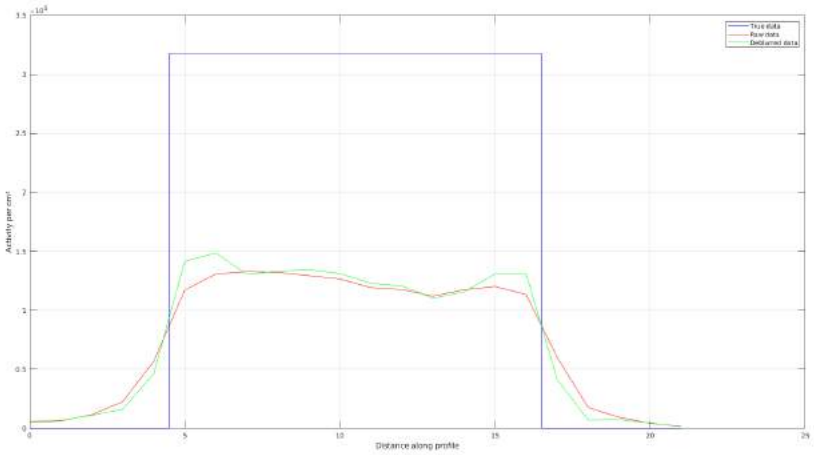

(c) Axial line profile - H25

Figure 2.21: Axial line across phantom with line profile - H25

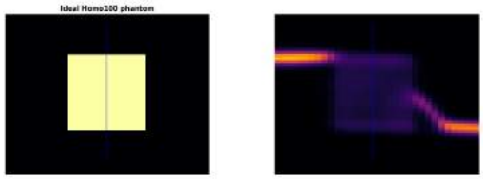

(a) Rad. line - H25 true (b) Rad. line - H25 raw

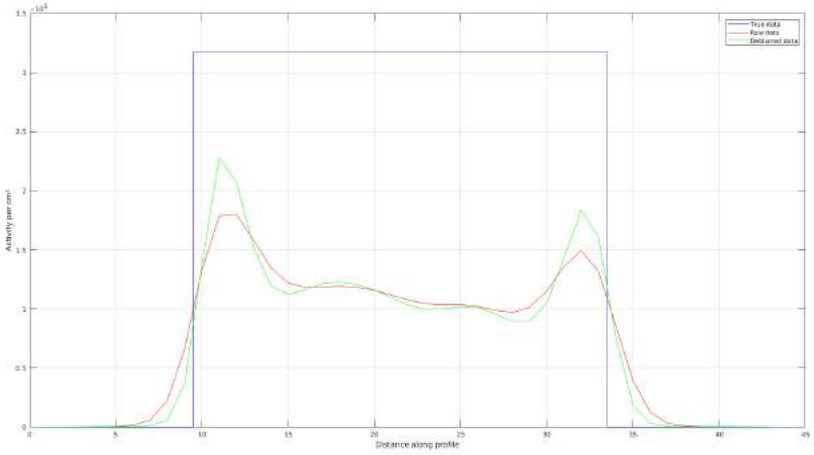

(c) Radial line profile - H25

Figure 2.22: Radial line across phantom with line profile - H25

2.3.5. 2x2 Phantom

The true and measured activity values of the 2x2 phantom are listed in table 2.10. The same trend concerning the maximum activity values is shown in the 2x2 phantom as in the previous homogeneous phantoms. FBP shows the lowest recovery values of the activity values and the highest standard deviation per feature of the phantom. OSEM2D shows the lowest standard deviation per feature, indicating the most homogeneous distribution of activity values across each feature. The OSEM3DMAP shows the highest recovery for both the mean and maximum activity values in the phantom. Relative contrast ratios in table 2.11 show higher values in iterative algorithms, especially in OSEM3D. FBP shows the lowest relative contrast ratios between features within the 2x2 phantom. SNR values show diverse outcomes for the 2x2 phantom. A remarkable observation is that OSEM3D and OSEM3DMAP show higher SNRs for the regions with low activity values, while FBP and OSEM2D show higher SNRs for the regions with high activity values.

Table 2.10: Maximum and mean activity values 2x2 phantom for each reconstruction algorithm

2x2 phantom					
	True values	FBP	OSEM2D	OSEM3D	OSEM3DMAP
Max. Activity [Bq/cm^2]	3.64E+06	1.34E+06	1.57E+06	2.50E+06	2.59E+06
W.r.t. True Maximum (%)	100.0	36.8	43.0	68.7	71.1
Mean Activity [Bq/cm^2]	2.28E+06	7.46E+05	8.98E+05	1.20E+06	1.27E+06
W.r.t. True Mean (%)	100.0	32.8	39.5	52.9	55.7
Average SD/ROI [Bq/cm^2]	0	1.60E+05	1.69E+05	2.53E+05	2.69E+05
W.r.t. Mean Act. (%)	0	21.4	18.8	21.0	21.2

The main argument for the creation of heterogeneous phantoms was to look at the capability of the scanner to distinguish FDG concentrations. To assess this capability, the proportions of activity values within features with respect to other features are compared. The true proportions between activity values based on the compartment heights are shown in figure 2.13. The number 1.0 stands for a printing height of 0.0 mm indicating the highest activity values present in that compartment. The other compartments 0.500, 0.250, and 0.750 refer to printing heights of 0.5 mm, 0.75 mm and 0.25 mm. Table 2.14, 2.15, 2.16 and 2.17 visualize the activity value proportions determined by the different reconstruction algorithms. Comparison with the true data shows a best match with OSEM3DMAP proportions. The true ratio between feature 21 and 22 equals 0.33. The OSEM3DMAP ratio between these features equals 0.372, which is higher than in OSEM3D: 0.375. The true ratio between feature 12 and 22 equals 0.67. The OSEM3DMAP ratio between these features equals 0.670, which is more accurate than in OSEM3D: 0.681. Ratios between other features are calculated, concluding that OSEM3DMAP matches best with the true proportions.

Table 2.11: Relative contrast ratios for different algorithms per ROI - 2x2 phantom

2x2 phantom				
	C_m/C_c			
Feature	**FBP**	**OSEM2D**	**OSEM3D**	**OSEM3DMAP**
11-12	0,856	0,861	0,998	0,987
11-21	0,813	0,818	0,945	0,937
12-22	0,876	0,909	0,950	0,985
21-22	0,788	0,803	0,908	0,914
11-22	0,811	0,778	1,066	0,987

A comparison of the line profiles across the 2x2 phantom can be observed in figures 2.23, 2.24, 2.25 and 2.26. Two line profiles across the features are drawn in the radial direction and two line profiles across the features are drawn in the axial direction. Activity fluctuations in the radial direction seem to occur more often in high activity areas: compare feature 11 with feature 22. The lower activity regions (feature 12 and 21) show less fluctuations in activity values. The line profiles across the features in the axial direction do not show high fluctuations in activity values and represent more smooth transitions, whereby the deblurred data shows slightly sharper transitions than the raw data.

Table 2.12: Signal-to-noise ratios for different algorithms per ROI - 2x2 phantom

	2x2 phantom	
	SNR	
FBP	21,678	7,385
	3,819	18,436
OSEM2D	25,797	7,678
	5,060	17,588
OSEM3D	11,215	8,752
	6,594	13,632
OSEM3DMAP	11,061	8,738
	7,958	13,848

Table 2.13: True proportions between activity values in the 2x2 phantom

1.000	0.500
0.250	0.750

Table 2.14: FBP

1,000	0,556
0,344	0,792

Table 2.15: OSEM2D

1,000	0,554
0,342	0,800

Table 2.16: OSEM3D

1,000	0,501
0,276	0,736

Table 2.17: OSEM3DMAP

1,000	0,505
0,280	0,753

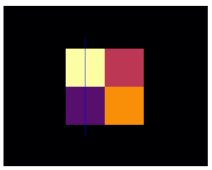

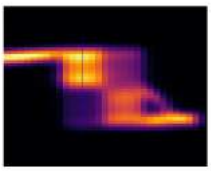

(a) Line 11-21 - 2x2 true (b) Line 11-21 - 2x2 raw

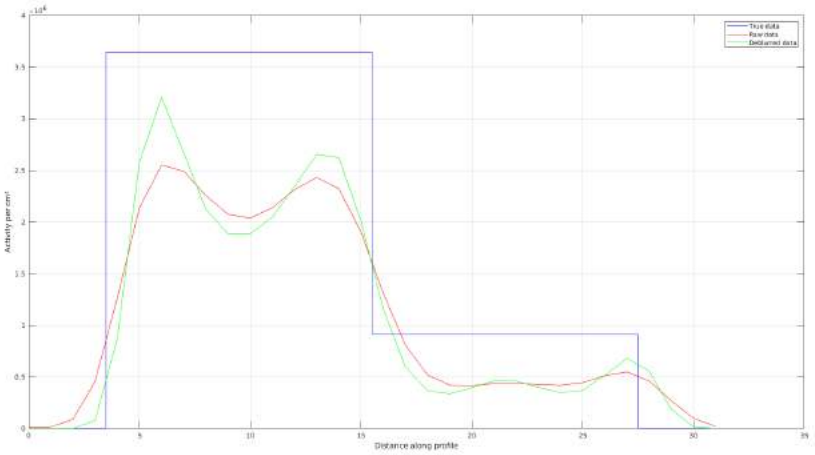

(c) Radial line profile 11-21 - 2x2 phantom

Figure 2.23: Radial line profile 11-21 - 2x2 phantom

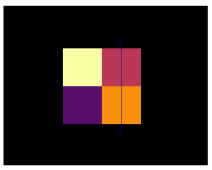

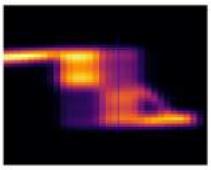

(a) Line 12-22 - 2x2 true (b) Line 12-22 - 2x2 raw

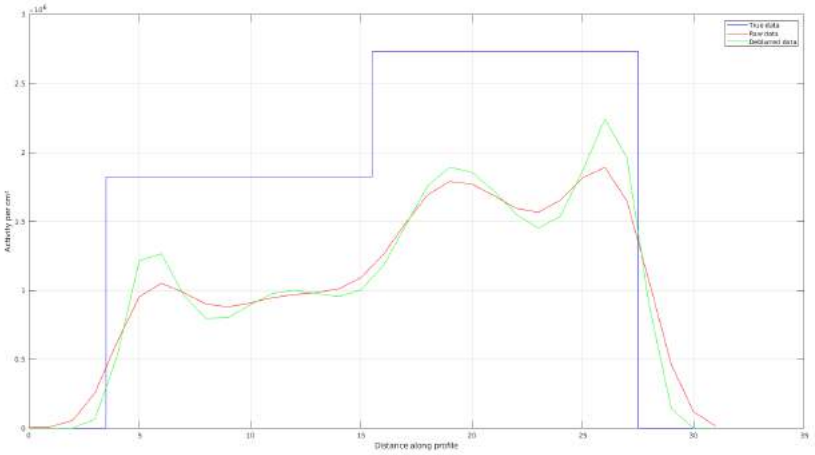

(c) Radial line profile 12-22 - 2x2 phantom

Figure 2.24: Radial line profile 12-22 - 2x2 phantom

(a) Line 11-12 - 2x2 true (b) Line 11-12 - 2x2 raw

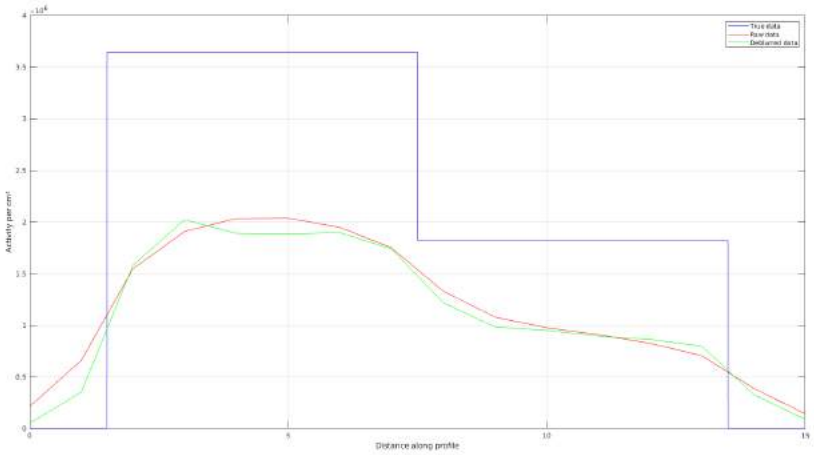

(c) Axial line profile 11-12 - 2x2 phantom

Figure 2.25: Axial line profile 11-12 - 2x2 phantom

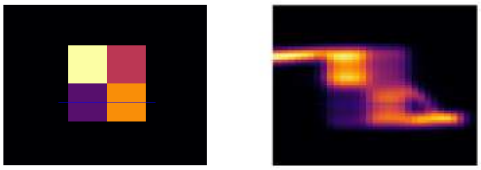

(a) Line 21-22 - 2x2 true (b) Line 21-22 - 2x2 raw

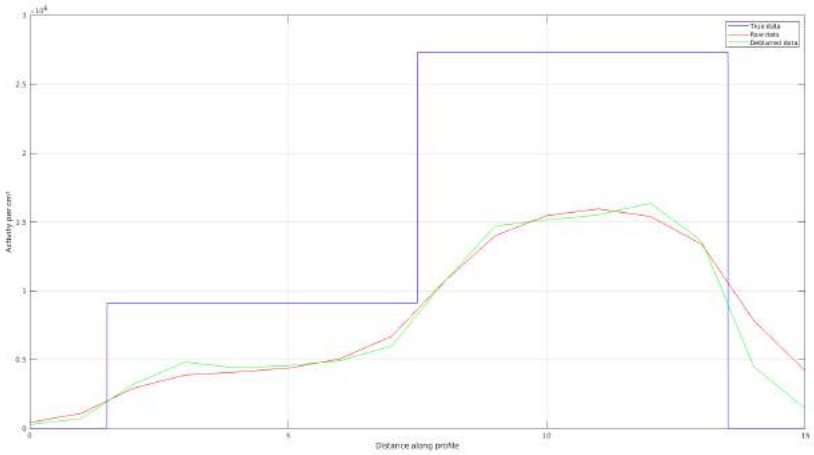

(c) Line profile 21-22 - 2x2 phantom

Figure 2.26: Axial line profile 21-22 - 2x2 phantom

2.3.6. 4x4 Phantom

The true and measured activity values of the 4x4 phantom are listed in table 2.18. Same results concerning the reconstruction algorithms is observed in this phantom compared with the other phantoms. The highest standard deviation per region of interest is shown in the OSEM3D algorithm. By analyzing the SNRs of the 4x4 phantom in table 2.20, FBP is the obvious winner showing the highest SNRs, with OSEM2D on second place. With regard to relative contrast ratios, the same observations in the 4x4 phantom are seen as for the 2x2 phantom: OSEM3D(MAP) showing significantly higher contrast in comparison with FBP and OSEM2D (table 2.19). The comparison of feature pairs with equal contrast ratio of the true phantom (figure 2.8) show conspicuous results shown in table 2.19 in which each two rows of contrast ratios should indicate equal contrast ratios. The majority of the feature pairs do not comply with this fact.

Table 2.18: Maximum and mean activity values 4x4 phantom for each reconstruction algorithm

4x4 phantom					
	True values	FBP	OSEM2D	OSEM3D	OSEM3DMAP
Max. Activity [Bq/cm^2]	2.37E+06	7.75E+05	9.51E+05	1.56E+06	1.59E+06
W.r.t. True Maximum (%)	100	32.6	40.1	65.7	66.8
Mean Activity [Bq/cm^2]	1.26E+06	4.50E+05	5.37E+05	6.66E+05	6.75E+05
W.r.t. True Mean (%)	100	35.7	42.6	52.9	53.5
Average SD/ROI [Bq/cm^2]	0	8.30E+04	9.93E+04	1.65E+05	1.65E+05
W.r.t. mean act. (%)	0	18.4	18.5	24.8	24.5

The proportions of activity values between features with respect to other features are compared for the 4x4 phantom. The true proportions between activity values based on the compartment heights are shown in table 2.21. Table 2.22, 2.23, 2.24 and 2.25 visualize the activity value proportions determined by the different reconstruction algorithms showing under- and overestimations of the activity values. Comparison with the true data shows a best match with OSEM3DMAP proportions. Interesting features are number 14 and 34 (table 2.3b), both features which should not supposed to contain activity values so should both possess the value 0. Feature 14 equals 0.291 and feature 34 equals 0.408 in which the latter was surrounded by high activity values, an explanation of the enhanced value. Features 21, 31 and 41 are supposed to contain the value 0.25 but equal 0.238, 0.243 and 0.228 respectively. A value lower than the true value, indicating spill-out of activity to the background.

Table 2.19: Relative contrast ratios for different algorithms per ROI - 4x4 phantom

4x4 phantom				
	C_m/C_c			
Feature	**FBP**	**OSEM2D**	**OSEM3D**	**OSEM3DMAP**
21-31	Inf	Inf	Inf	Inf
22-32	Inf	Inf	Inf	Inf
14-24	0,458	0,493	0,613	0,623
34-44	0,234	0,287	0,433	0,441
12-13	0,038	0,026	0,029	0,024
32-33	0,691	0,708	0,834	0,828
22-23	0,990	1,064	1,184	1,188
42-43	1,132	1,134	1,182	1,179
23-24	0,133	0,227	0,605	0,618
43-44	0,315	0,321	0,661	0,682
11-12	0,227	0,256	0,366	0,366
11-21	0,684	0,728	0,916	0,900
13-14	0,222	0,245	0,365	0,368
14-24	0,458	0,493	0,613	0,623

A comparison of the line profiles across the 4x4 phantom are shown in figures 2.27 to 2.34. Line profiles are examined across each row or column of features. The line profiles in the axial direction are interesting for the second row (21-22-23-24) and the fourth row (41-42-43-44) which both possess the same gradient of height differences, showing the same trend of activity values across the gradient.

Table 2.20: Signal-to-Noise ratios for different algorithms per ROI - 4x4 phantom

	4x4 phantom			
	SNR			
FBP	4.63	5.72	4.90	1.76
	3.68	6.92	10.08	9.39
	3.68	5.59	17.25	2.98
	2.97	4.43	5.65	7.66
OSEM2D	3.93	5.34	5.62	1.72
	3.72	6.80	9.68	9.79
	3.69	5.75	16.00	2.59
	3.17	5.23	6.98	6.57
OSEM3D	2.26	3.44	6.94	1.35
	3.66	6.15	8.38	5.08
	3.81	5.15	10.67	1.79
	2.92	4.57	5.72	3.36
OSEM3DMAP	2.35	3.54	6.73	1.35
	3.66	6.11	8.12	4.91
	3.81	5.20	10.95	1.77
	2.91	4.59	5.73	3.47

Table 2.21: True proportions between activity values in the 4x4 phantom

1.000	0.250	0.500	0.000
0.250	0.500	0.750	1.000
0.250	0.500	1.000	0.000
0.250	0.500	0.750	1.000

Deblurred data shows improvement in activity value transitions between different compartments. The extreme fluctuations present in the data of the 2x2 phantom were less visible in the 4x4 phantom data, seen in figure 2.31. The fluctuations in data seen in figure 2.32 are explained by the adjacent high activity values of column 3 (figure 2.33). Figure 2.34 shows the obvious improvement of the deblurred data with respect to raw data showing enhanced maximum values and lowered minimum values.

Table 2.22: FBP

1,000	0,760	0,741	0,472
0,330	0,644	0,963	1,000
0,281	0,626	1,000	0,570
0,267	0,577	0,914	1,000

Table 2.23: OSEM2D

1,000	0,734	0,721	0,438
0,304	0,608	0,937	1,000
0,282	0,618	1,000	0,526
0,269	0,575	0,912	1,000

Table 2.24: OSEM3D

1,000	0,640	0,628	0,292
0,239	0,519	0,841	1,000
0,242	0,565	1,000	0,410
0,229	0,511	0,828	1,000

Table 2.25: OSEM3DMAP

1,000	0,640	0,630	0,291
0,238	0,516	0,838	1,000
0,243	0,568	1,000	0,408
0,228	0,509	0,823	1,000

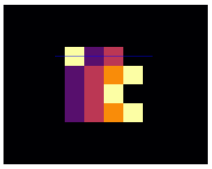

(a) Line - 4x4 true

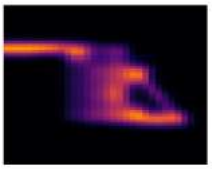

(b) Line - 4x4 raw

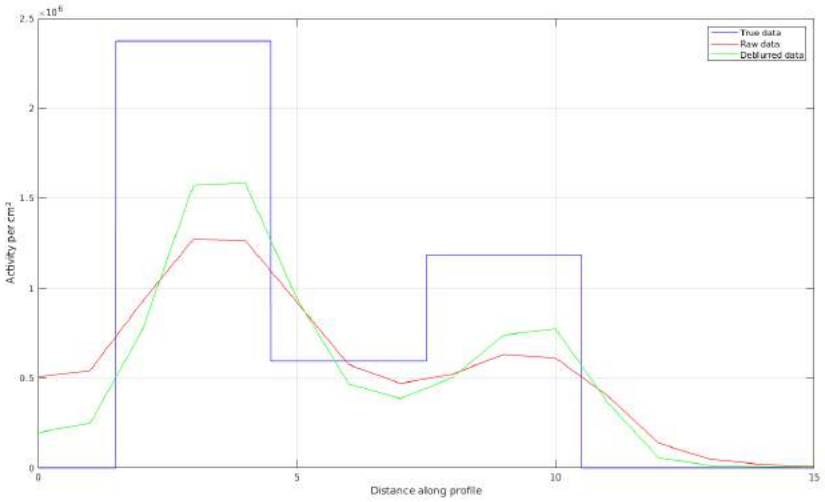

(c) Line profile 11-12-13-14

Figure 2.27: Line profile 11-12-13-14 - 4x4 phantom

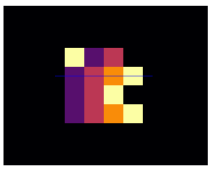

(a) Line - 4x4 true

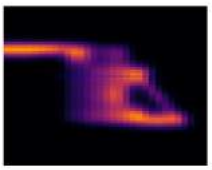

(b) Line - 4x4 raw

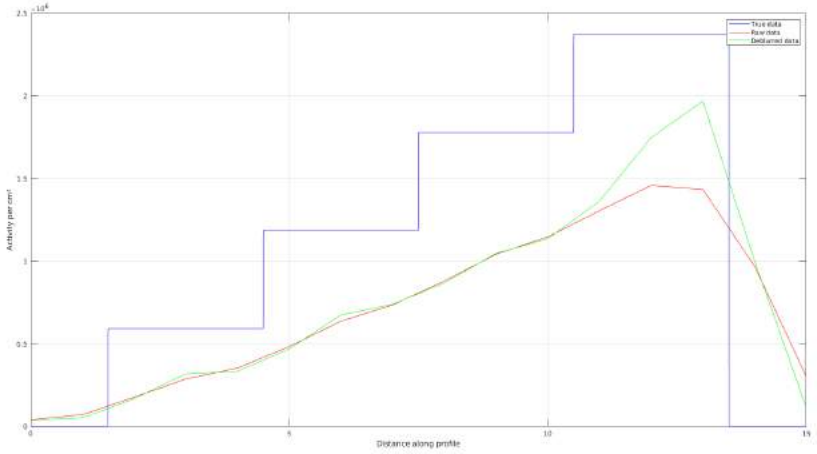

(c) Line profile 21-22-23-24

Figure 2.28: Line profile 21-22-23-24 - 4x4 phantom

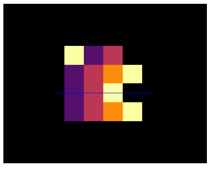

(a) Line - 4x4 true

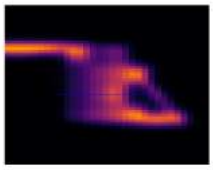

(b) Line - 4x4 raw

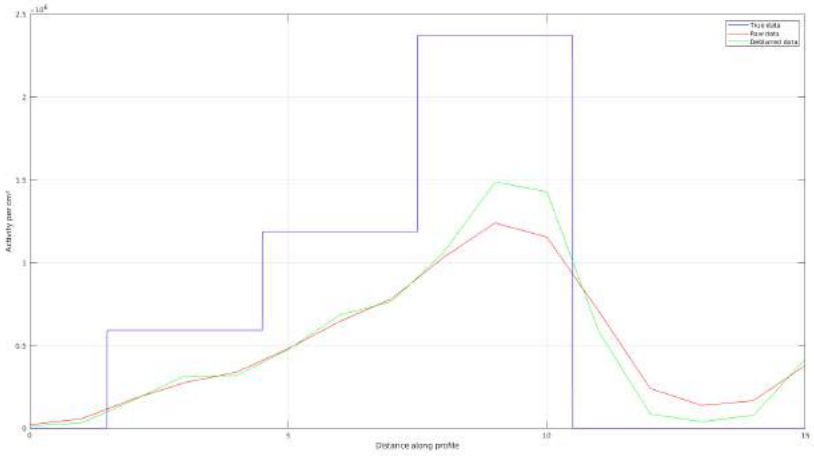

(c) Line profile 31-32-33-34

Figure 2.29: Line profile 31-32-33-34 - 4x4 phantom

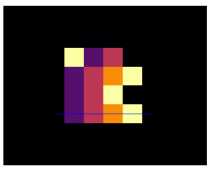

(a) Line - 4x4 true

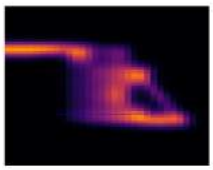

(b) Line - 4x4 raw

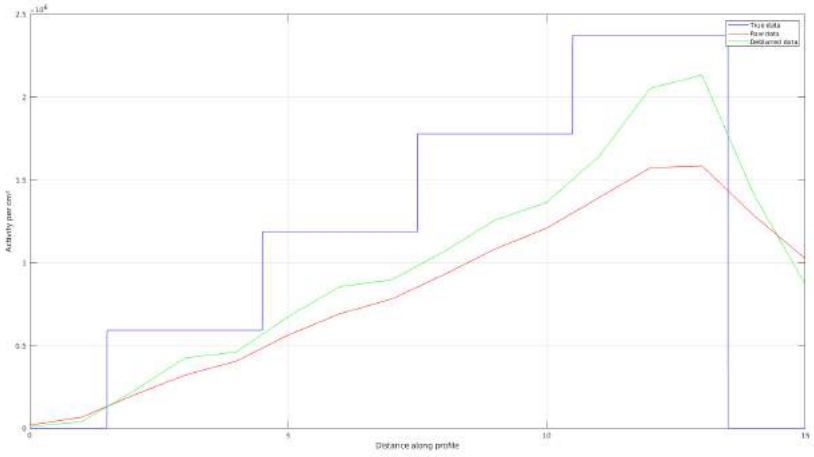

(c) Line profile 41-42-43-44

Figure 2.30: Line profile 41-42-43-44 - 4x4 phantom

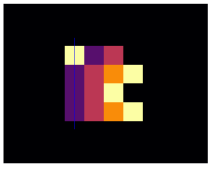

(a) Line - 4x4 true

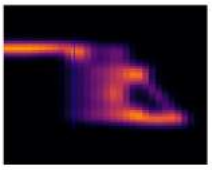

(b) Line - 4x4 raw

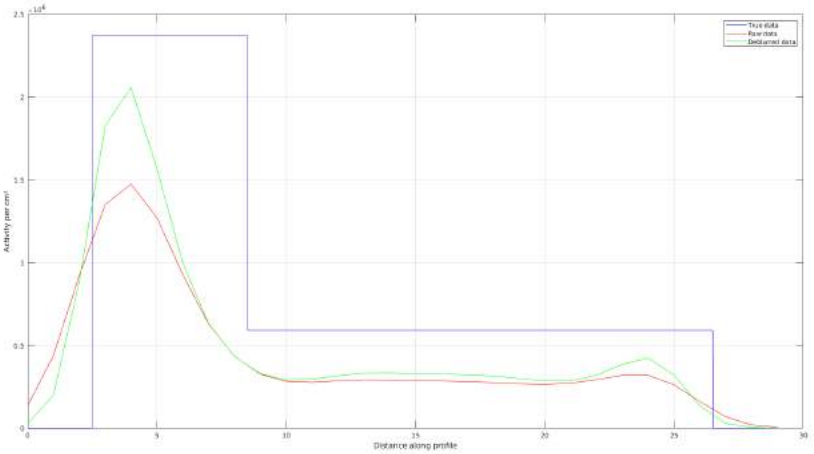

(c) Line profile 11-21-31-41

Figure 2.31: Line profile 11-21-31-41 - 4x4 phantom

(a) Line - 4x4 true

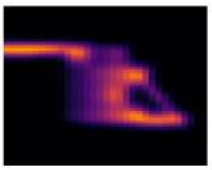

(b) Line - 4x4 raw

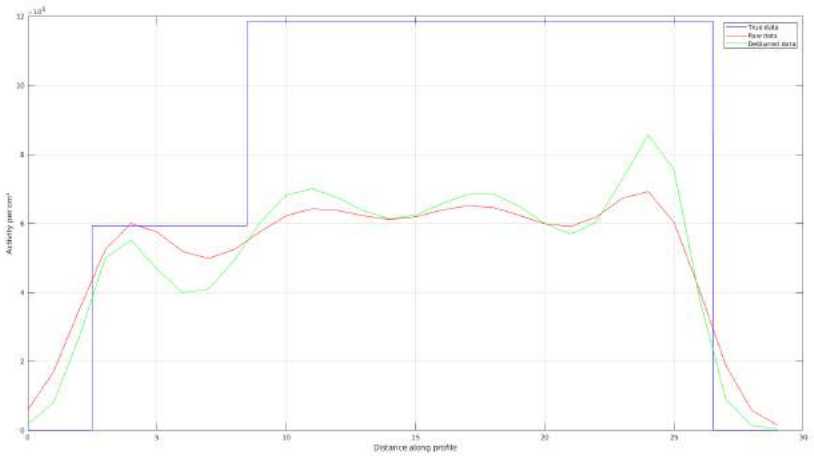

(c) Line profile 12-22-32-42

Figure 2.32: Line profile 12-22-32-42 - 4x4 phantom

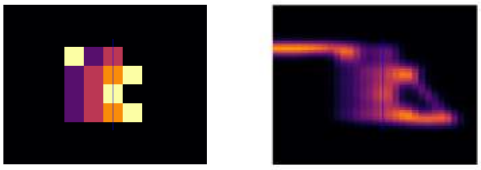

(a) Line - 4x4 true (b) Line - 4x4 raw

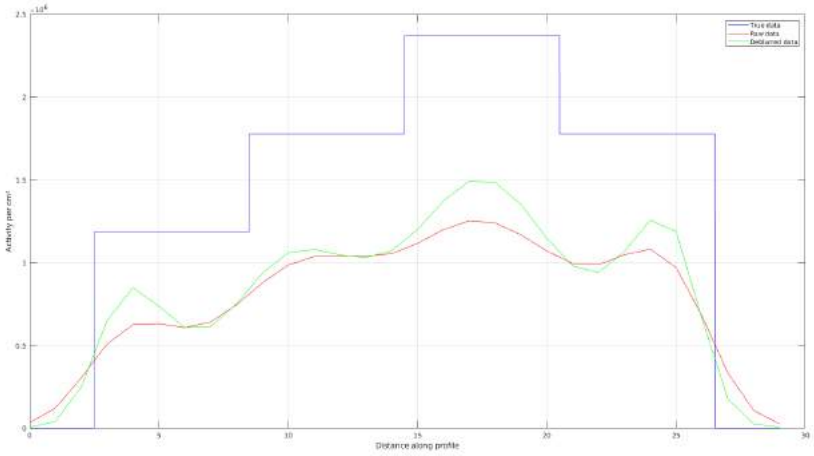

(c) Line profile 13-23-33-43

Figure 2.33: Line profile 13-23-33-43 - 4x4 phantom

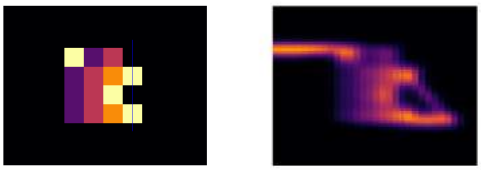

(a) Line - 4x4 true (b) Line - 4x4 raw

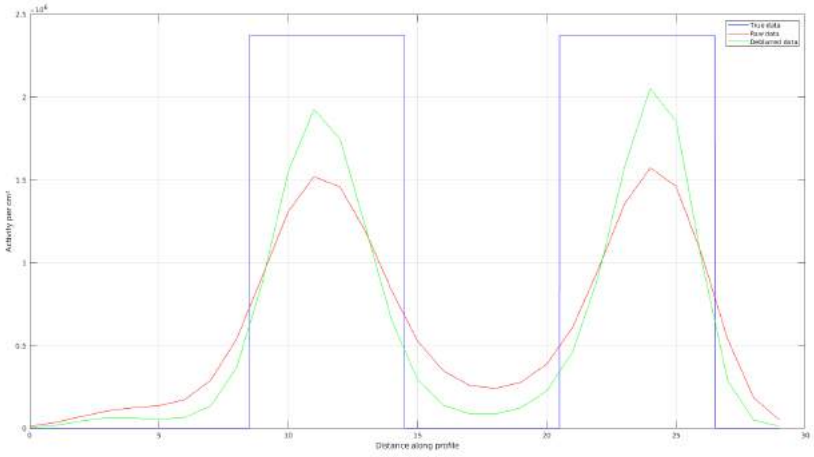

(c) Line profile 14-24-34-44

Figure 2.34: Line profile 14-24-34-44 - 4x4 phantom

Table 2.26: RMSD for all phantoms & reconstruction algorithms

	RMSD values			
	FBP	**OSEM2D**	**OSEM3D**	**OSEM3DMAP**
4x4 phantom	0,840	0,843	0,789	0,786
2x2 phantom	0,786	0,805	0,761	0,774
H100 phantom	0,537	0,551	0,555	0,548
H25 phantom	0,939	0,952	0,963	0,965

2.3.7. RMSD Values

An overview of RMSD values per phantom and per algorithm is shown in table 2.26. To recap from section 2.2.8: the RMSD describes the amount of similarity between the phantom based on the PET measurements and the computational phantom. RMSD values do not show extreme differences between the reconstruction algorithms. For the heterogeneous phantoms slightly better RMSD values are seen in OSEM3D and OSEM3DMAP. For the homogeneous phantoms, FBP and OSEM2D show a slightly better RMSD.

2.4. Deblurring of the Snake Phantom

The deblurring technique is applied on the snake phantom for all reconstruction algorithms. The result of the deblurring technique is shown in figure 2.36 in which for each reconstruction algorithm a line profile is taken for the raw data and the deblurred data (figure 2.35). For each reconstruction algorithm the deblurred data shows a more accurate representation of the data with respect to the true data. Both OSEM3D and OSEM3DMAP show capability of complete distinction between the two most right segments of the snake phantom. Since OSEM3DMAP shows the highest deblurring performance, the deblurring technique was applied on the remaining phantoms for the OSEM3DMAP reconstruction algorithm. The results are shown in the following section.

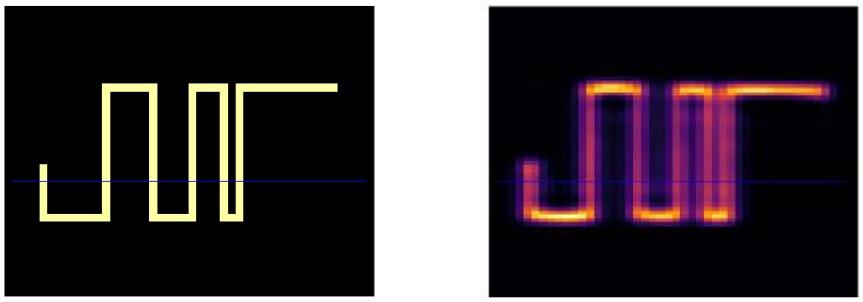

(a) Axial line - true data (b) Axial line - raw data

Figure 2.35: Lines across snake phantom

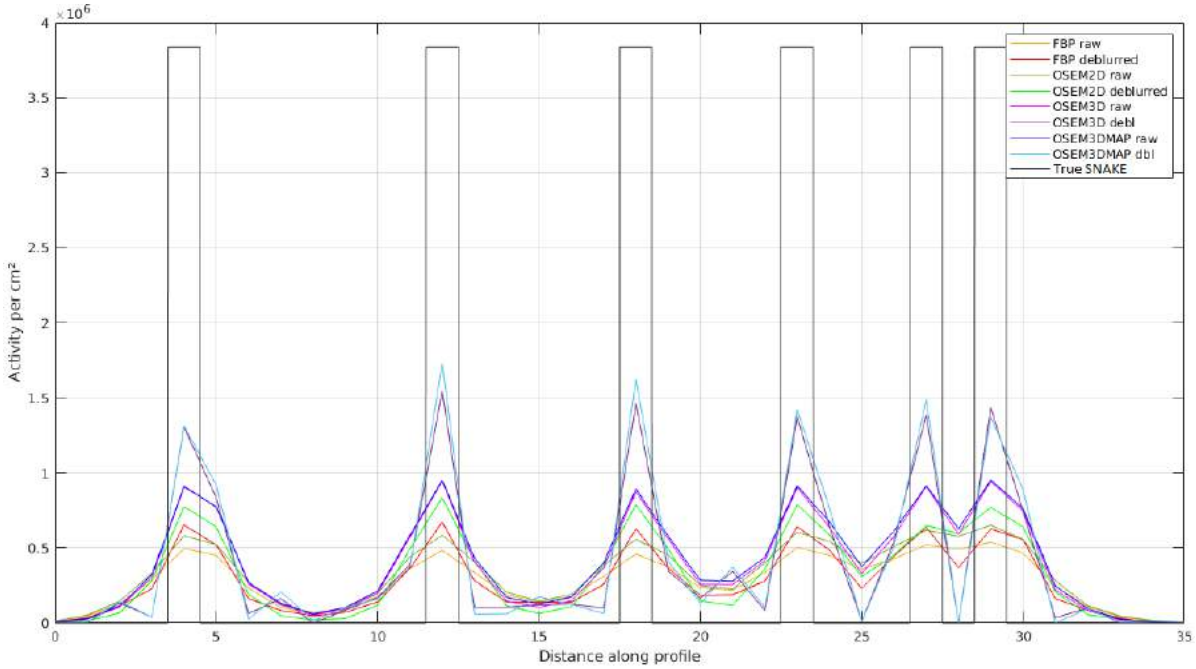

Figure 2.36: Line profiles raw and deblurred SNAKE phantom per reconstruction algorithm

2.5. Deblurred outcomes of OSEM3DMAP

Homogeneous H100 Phantom

In the H100 phantom, a large increase in maximum activity is observed in deblurred data (table 2.27), while a small increase in mean activity is seen, resulting in increased standard deviation in the phantom. The SNR decrease in both ROIs in the deblurred data, a rational observation when standard deviations are increased (table 2.28). The relative contrast shows a minimal increase (table 2.29).

Table 2.27: Maximum and mean activity raw data vs. deblurred data - H100

	H100 phantom		
	True values	Raw data	Deblurred data
Max. $[Bq/cm^2]$	4,93E+06	3,46E+06	4,41E+06
W.r.t. True Max (%)	100	70,2	89,4
Mean $[Bq/cm^2]$	4,93E+06	2,94E+06	3,10E+06
W.r.t. True Mean (%)	100	59,6	62,8
Av. SD/ROI $[Bq/cm^2]$	0	3,74E+05	5,07E+05
W.r.t. Mean Act (%)	0	12,7	16,4

Table 2.28: SNR raw vs. deblurred data - H100

	H100 phantom		
	SNR		
	Feature	**Raw data**	**Debl Data**
OSEM3DMAP	ROI 1	16,87	11,48
	ROI 2	42,94	30,55

Homogeneous H25 Phantom

A remarkable observation in the deblurred data of the H25 phantom is the recovery of the maximum activity above the true maximum: a value of 105%, shown in table 2.30. The mean activity shows only an increase of 2%. SNR values (table 2.31) and relative contrast (table 2.32) values show similar outcomes compared with the H100 phantom.

Table 2.29: Relative contrast raw vs. deblurred data - H100

	H100 phantom		
	C_m/C_r		
	Feature	**Raw data**	**Debl Data**
OSEM3DMAP	ROI	0,9995	0,9996

Table 2.30: Maximum and mean activity raw data vs. deblurred data - H25

	H25 phantom		
	True values	Raw data	Deblurred data
Max. [Bq/cm^2]	3,18E+05	2,85E+05	3,34E+05
W.r.t. True Max (%)	100	89,7	105,1
Mean [Bq/cm^2]	3,18E+05	1,32E+05	1,39E+05
W.r.t. True Mean (%)	100	41,6	43,8
Av. SD/ROI [Bq/cm^2]	0	2,80E+04	3,90E+04
W.r.t. Mean Act (%)	0	21,2	28,0

Table 2.31: SNR raw vs. deblurred data - H25

	H25 phantom		
	SNR		
	Feature	**Raw data**	**Debl Data**
OSEM3DMAP	ROI 1	6,22	4,73
	ROI 2	14,50	10,51

Table 2.32: Relative contrast raw vs. deblurred data - H25

	H25 phantom		
	C_m/C_r		
	Feature	**Raw data**	**Debl Data**
OSEM3DMAP	ROI	0,9994	0,9995

2x2 Phantom

Deblurring of the heterogeneous 2x2 phantom shows the largest improvement in the proportions of the activity values, shown in table 2.36. Improvement is seen between features 21 and 22: a ratio of 0.333 for true data, 0.372 for raw data and 0.328 for deblurred data. Between features 21 and 12, the ratio improves from 0.554 to 0.518 with a true ratio of 0.50. SNR values for deblurred data only increases in feature 21 (table 2.34). Relative contrast increases between all features for deblurred data (table 2.35).

Table 2.33: Maximum and mean activity raw data vs. deblurred data - 2x2

	2x2 phantom		
	True values	Raw data	Deblurred data
Max. [Bq/cm^2]	3,64E+06	2,59E+06	3,29E+06
W.r.t. True Max (%)	100,0	71,1	90,4
Mean [Bq/cm^2]	2,28E+06	1,27E+06	1,33E+06
W.r.t. True Mean (%)	100,0	55,7	58,3
Av. SD/ROI [Bq/cm^2]	0	2,69E+05	3,49E+05
W.r.t. Mean Act (%)	0,0	21,2	26,3

Table 2.34: SNR raw vs. deblurred data - 2x2

	2x2 phantom			
	SNR raw data		SNR dbl data	
OSEM3DMAP	11,061	8,738	5,438	6,678
	7,958	13,848	8,780	10,276

Table 2.35: Relative contrast raw vs. deblurred data - 2x2

	2x2 phantom		
	C_m/C_c		
	Feature	Raw data	Debl Data
OSEM3DMAP	11-12	0,987	1,078
	11-21	0,937	1,013
	12-22	0,985	1,125
	21-22	0,914	1,013
	11-22	0,987	1,023

Table 2.36: Deblurred data activity proportions - 2x2

1.000	0.471
0.244	0.745

4x4 Phantom

A great improvement in the proportions of the deblurred activity values of the 4x4 phantom is observed, reflecting the true height proportions more accurately. This result can be observed in a 3D representation of the 4x4 phantom shown in figure 2.37, for the true data, raw data and deblurred data. Transitions between phantom compartments are smooth for the raw data and show more sharp transitions between compartments in the deblurred data.

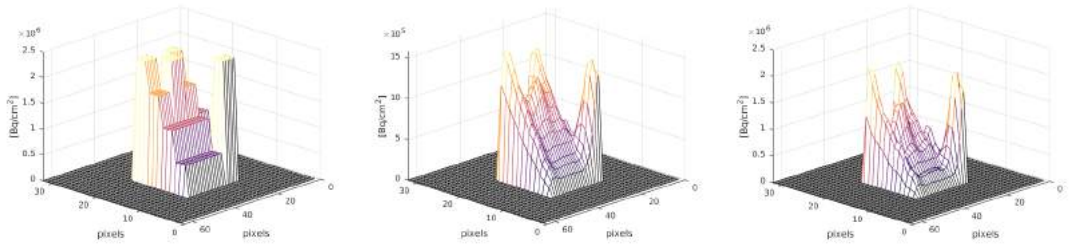

(a) 3D representation 4x4 true data

(b) 3D representation 4x4 raw data

(c) 3D representation 4x4 deblurred data

Figure 2.37: 3D representation of the 4x4 phantom: true, raw and deblurred data

Regarding the proportions, remarkable differences are seen between features that are surrounded by large height differences compared to small surrounding height differences. For example feature 12 which is surrounded by very high activities compared to features 21, 31 and 41 of which the latter features resemble more true activity, while feature 12 is more than doubled compared to the other features. Same results are observed regarding the maximum and mean activity values in deblurred data as in the other phantoms (table 2.37). SNR values per feature are lowered for deblurred data (table 2.38), but relative contrast values between features show again significant improvement, shown in table 2.39. The majority of feature pairs show higher similarity in the deblurred data than in the raw data.

Images of measured PET data and deblurred PET data of all phantoms is shown in figure 2.38.

Table 2.37: Maximum and mean activity raw data vs. deblurred data - 4x4

	4x4 phantom		
	True values	Raw data	Deblurred data
Max. $[Bq/cm^2]$	2,37E+06	1,59E+06	2,13E+06
W.r.t. True Max (%)	100	66,8	89,9
Mean $[Bq/cm^2]$	1,26E+06	6,75E+05	7,03E+05
W.r.t. True Mean (%)	100	53,5	55,8
Av. SD/ROI $[Bq/cm^2]$	0	1,65E+05	2,30E+05
W.r.t. Mean Act. (%)	0	24,5	32,6

Table 2.38: SNR raw vs. deblurred data - 4x4

	4x4 phantom							
	SNR raw data				**SNR deblurred data**			
OSEM3DMAP	2.35	3.54	6.73	1.35	1,72	2,52	4,95	1,05
	3.66	6.11	8.12	4.91	3,48	5,36	7,67	3,00
	3.81	5.20	10.95	1.77	3,57	5,20	6,01	1,16
	2.91	4.59	5.73	3.47	2,42	3,49	4,33	2,30

Table 2.39: Relative contrast raw vs. deblurred data - 4x4

	4x4 phantom		
	C_m/C_c		
	Feature	**Raw data**	**Deblurred data**
OSEM3DMAP	21-31	Inf	Inf
	22-32	Inf	Inf
	14-24	0,623	0,734
	34-44	0,441	0,615
	12-13	0,024	0,211
	32-33	0,828	0,991
	22-23	1,188	1,206
	42-43	1,179	0,910
	23-24	0,618	0,954
	43-44	0,682	0,915
	11-12	0,366	0,530
	11-21	0,900	0,997
	13-14	0,368	0,524
	14-24	0,623	0,734

Table 2.40: Proportions deblurred OSEM3DMAP data - 4x4 phantom

1.000	0.517	0.596	0.186
0.207	0.465	0.760	1.000
0.219	0.503	1.000	0.252
0.212	0.475	0.769	1.000

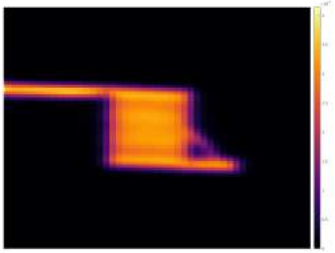

(a) Raw data - H100 phantom

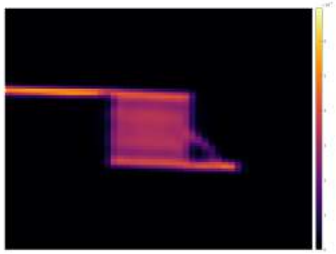

(b) Deblurred data - H100 phantom

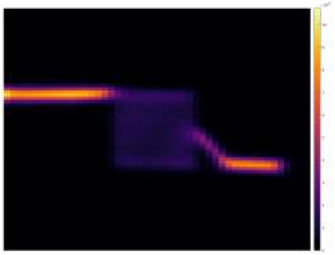

(c) Raw data - H25 phantom

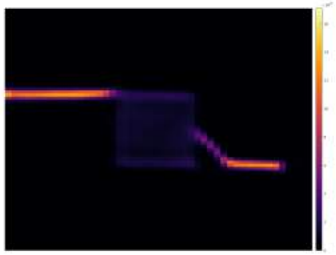

(d) Deblurred data - H25 phantom

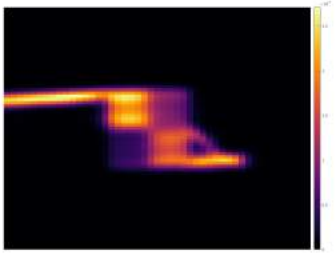

(e) Raw data - 2x2 phantom

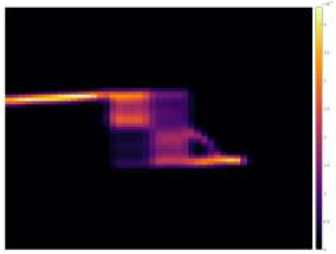

(f) Deblurred data - 2x2 phantom

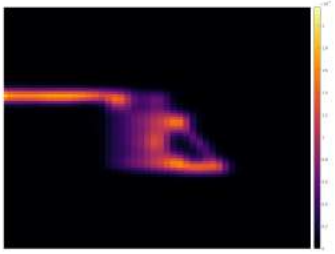

(g) Raw data - 4x4 phantom

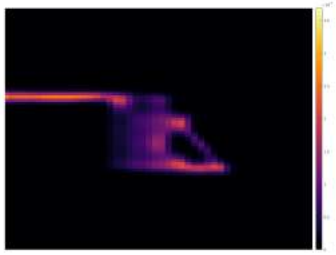

(h) Deblurred data - 4x4 phantom

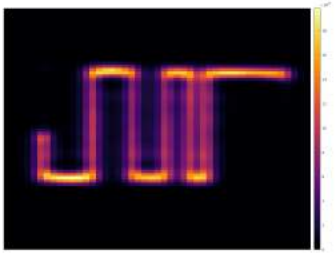

(i) Raw data - snake phantom

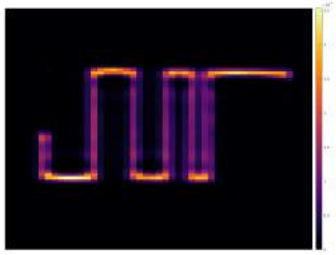

(j) Deblurred data - snake phantom

Figure 2.38: Deblurred images of the OSEM3DMAP reconstruction algorithm

2.6. Discussion & Conclusion

In the presented work, an in depth examination on the performance of the Inveon microPET system was accomplished in which the available reconstruction algorithms available on the system were compared. This was the first step of the presented work. The second step included the development of a deblurring technique in order to deblur the reconstructed data and correct for the spillover effect. The deblurring technique has been applied on phantom experiments with the microPET scanner based on the most appropriate reconstruction algorithm.

Phantom experiments accomplished with the microPET scanner have been performed based on 3D-printing technologies for the NEMA phantom [6] and the Derenzo phantom [21]. The present work appeared to be the first in using 3D-printed phantoms reflecting tumor heterogeneity and showed great performance in the use to characterize the microPET system. Points of concern with respect to the 3D-printing material could include the absorption of FDG by the material and the formation of air bubbles during filling. Research showed that the first concern was not applicable and that FDG was not absorbed by the 3D-printed material [32]. To overcome the problem of air bubble formation, multiple designs were printed and tested for the filling of the phantom. This process was optimized, resulting in an airtight compartment without the presence of bubbles.

The performance of the Inveon microPET system was quantified for different reconstruction algorithms with accompanying figures of merit. The results regarding the capability of reconstruction algorithms to reconstruct true values showed what was expected: maximum and mean activity values were higher for more complex reconstruction algorithms compared to mathematically less complex algorithms since iterative algorithms are built to reconstruct data more accurately [88]. High deviations in reconstructed data were mainly observed in iterative algorithms which is a generally known observation for iterative reconstruction algorithms since increasing number of iterations amplify noise artifacts [17].

The investigation of the signal-to-noise ratios in the phantom features for different reconstruction algorithms allowed a useful method to compare reconstruction performance. However, the determination of signal-to-noise ratios for extreme small features as in the 4x4 phantom brings doubt in the reliability of the ratios. The relative contrast for the homogeneous phantoms couldn't be reliably compared since contrast was determined between the ROI in the phantom and a region in the background. As mentioned in section 2.2.6, reconstructed FBP data showed negative pixel values in the background which were all set to zero, therefore creating an unreliable approach of the relative contrast with respect to other algorithms.

A main point of concern includes the alignment of the computed phantom with the phantoms in the PET images. Despite the 2D cross-correlation in order to perfectly align the phantoms, an error was present in the alignment of the phantoms. This point of concern is caused by the limited pixel dimensions of the microPET scanner (0.39 mm x 0.79 mm). The dimensions refrain to resemble the exact phantom dimensions of 10.0 x 10.0 mm (and features of 2.5 mm x 2.5 mm and 5.0 mm x 5.0 mm). The chosen dimensions of the computational phantom are slightly smaller than the true dimensions with an error of 112 μm in one single feature of the 4x4 phantom in the x-direction, and 448 μm in total in the x-direction. In the y-direction this equals 171 μm for a single feature in the 4x4 phantom, and 683 μm in total in the y-direction, accounting for an error of 4.48% in the x-direction and an error of 6.83% in the y-direction. A comparable concern was observed in the z-direction in the H25 phantom. The region in which activity is present was 0.25 mm. With a slice thickness of 0.39 mm, an underestimation of the mean activity values in this phantom was generated. This was indeed observed in the low mean activity values compared to the other phantoms.

The deblurring technique was applied on the snake phantom for all reconstruction algorithms. Results showed improved spatial resolution in the OSEM3D algorithms with increased maximum values and lowered minimum values, approaching more the true activity values. Regarding the deblurring technique, the OSEM3DMAP algorithm performed best in contrast improvement of the PET images and sharper edges between features within the phantom, therefore allowing a correction strategy for the spillover effect. However, edge artifacts are present in OSEM3D and OSEM3DMAP. They appear as an intensification of the activity at a sharp transition in the phantom, preventing a true representation of the activity distribution within a feature. Edge artifacts were less observed in FBP. Tsutsui et al. reported that edge artifacts are dependent on the iteration number of the reconstruction algorithm and object size [81], two concepts which must be further addressed in future work.

The presented work has shown the ability of the deblurring technique to improve the contrast and

transition between phantom features. The most remarkable contribution of the deblurring technique is the correction for the spillover effects, leading to improved differentiation of FDG values in small features. MicroPET scanners that apply the deblurring technique on PET images would be capable to deblur the images and represent a more accurate representation of the measured object.

3

Ex vivo Validation of PET Imaging for Response Assessment in Non-Small Cell Lung Cancer

Abstract

Response based dose-painting in Non-Small Cell Lung Cancer (NSCLC) patients during treatment based on high 2-deoxy-2-(^{18}F)fluoro-D-glucose (FDG) regions is an effective method to overcome the challenge of intra-tumor heterogeneity. The challenge remains to validate the correlation of the imaging target with a local biological trait. Pathology is required to assess the challenge. However, since the study concerns inoperable patients, the pathology cannot be accessed. An *ex vivo* culturing platform is set up to validate PET imaging tracers for response assessment of NSCLC patients and to correlate FDG uptake with the number of proliferating cells. An unbiased method is presented to assess the number of proliferating cells present in histology images. From ten NSCLC patients the pathology is examined. Of each individual tumor slice the number of proliferating cells is determined with an automated detection method in viable tissue whereupon a linear mixed-effects model is used to investigate FDG uptake with the number of proliferating cells within patients. Results show that no significant correlation exists between FDG and the number of proliferating cells. This implicates that FDG uptake in tumor slices does not significantly reflects the number of proliferating cells. Therefore, FDG was not suitable as a highly selective tracer for response based imaging during radiotherapy treatment in NSCLC.

Keywords **—** Non-Small Cell Lung Cancer - Ki-67 - proliferating cells - FDG uptake - automated detection method - pathology - *ex vivo*

Note

The following work is written by multiple authors of the Erasmus Medical Center, Rotterdam. The following sections are written by other authors: section 3.1, 3.2.1, 3.2.2, 3.2.3, 3.2.4. The sections 3.2.5, 3.2.6, 3.2.7, 3.3, 3.4 and the abstract are written by C.F. Groenendijk.

3.1. Introduction

Lung cancer is the leading cause of cancer related deaths, with 1.6 million deaths worldwide [30]. Non-Small Cell Lung Cancer (NSCLC) accounts for 80-85% of all lung cancer diagnoses and is therefore the most common type of lung cancer. Many patients are diagnosed with inoperable NSCLC and about 40% of patients with advanced stage disease [69]. Advanced stage NSCLC patients are offered chemo-radiation treatment, but despite this 3-year survival is only 27% [35]. Intra-tumor heterogeneity of NSCLCs plays a key role in the development of therapy resistance and negatively influences radiotherapy outcomes, since specific sub-regions of the tumor may be resistant to chemo-radiotherapy [56, 64]. Therefore, dose-painting, a technique that allows one to more precisely prescribe different radiation dosimetries to different areas within the tumor, may be a very effective method to overcome this challenge of intra-tumor heterogeneity. Thanks to recent advances in proton therapy and robotic radiosurgery, it is technically feasible to deliver a high boost of radiation specifically to small sub-regions of a tumor without compromising the treatment tolerance. The most pragmatic strategy for improving radiotherapy outcome is response-based dose-painting. First, patients are treated with a conventional radiation plan, followed by response measurement. Next, according to the response of different intratumor areas, the remaining fractions are boosted in the poorly responding tumor regions. However, the main challenge for response-based dose-painting is to measure response noninvasively in 3D *in vivo*. Positron emission tomography (PET) imaging using 2-deoxy-2-[^{18}F]fluoro-D-glucose (FDG) is currently used in the clinic for radiation treatment planning [25]. Whether PET tracers could be useful to noninvasively identify differences in response across the tumor should be validated first. The gold standard for determining therapy response is pathologic examination of the resected tissue (either by biopsy material or surgical specimen). However, it is not feasible to relate *in vivo* PET imaging results to *ex vivo* resected material. Recently, we have developed technology to keep organotypic tissue slices of breast tumors alive *ex vivo* for at least one week [63]. The advantage of this tumor model system is that the tumor cells remain in their natural (micro)environment. Under optimal culture conditions, the fraction of tumor cells that is dividing remains constant for a period of at least one week, indicating that these conditions faithfully mimic tumor growth in the patient [63]. Organotypic tissue slices from NSCLCs would represent a useful *ex vivo* model system to test whether tracer uptake corresponds with pathologic examination. The aim of this study is to set up an experimental procedure to validate PET imaging tracers for response assessment of NSCLC patients *ex vivo*. Using this procedure, we determined whether FDG uptake reflects the number of proliferating tumor cells.

3.2. Methods

The experimental setup of the presented study is composed of multiple steps, described in the following subsections. An overview of the procedure is displayed in figure 3.1.

3.2.1. NSCLC specimens

Residual fresh NSCLC tissue was prospectively collected from lobectomy specimens in the Erasmus MC Cancer Institute in Rotterdam, The Netherlands between 20-01-2016 and 06-06-2017. After macroscopic evaluation of the surgical specimen by trained pathologists, residual tumor tissue was collected for our research purposes according to the "Code of proper secondary use of human tissue in the Netherlands" established by the Dutch Federation of Medical Scientific Societies and approved by the local Medical Ethical committees. Patients who had objected to secondary use of residual tumor material for research purposes were not included in this study.

3.2.2. Tissue slicing and culturing

Tumor samples were collected in a RPMI culture medium. Tissue slicing was performed using a Leica VT 1200S Vibratome with slice thickness set at 300 μm, vibration amplitude at 3.0 mm and slicing speed at 0.45 mm/sec, as described previously [63]. Slicing was performed under semi-sterile conditions; without the use of a flow hood. No contaminations were encountered under these conditions. Slices were cultured within 6 hours after the tumor was removed from the patient. Lung tissue slices were cultured at 5% CO^2 at 37 °C and at atmospheric oxygen levels, under constant rotation at 60 rpm using a Stuart SSM1 mini orbital shaker that was placed in the incubator. For culture medium conditions, we tested our customized breast medium [63], DMEM/HAM1:1 with 10% FCS and antibiotics and RPMI

Figure 3.1: Experimental setup

with 10% FCS and antibiotics. The number of proliferating cells after 2, 5 and 7 days of culture was determined to identify the optimal medium condition. Proliferating cells were labeled using 3 μg/ml 5-Ethynyl deoxyuridine (EdU) (Invitrogen) during the last 2 hours before fixation.

3.2.3. PET imaging

For PET imaging, 3.4 – 8.1 MBq FDG was added to the culture medium and was incubated on an orbital shaker at 60 rpm for 30 minutes at room temperature. Next, the tumor samples were transferred to well plates containing PBS and washed for 30 minutes on an orbital shaker (60 rpm) for 30 minutes. This wash step was repeated for 10 minutes in another well plate with fresh PBS. To have a fixed orientation during and after the PET scan, the tumor slices were put into a Falcon cell strainer (Fisher Scientific). The cell strainer containing the tumor sample in their turn were fixed in the well of a six well plate. In the well PBS was present with a liquid level height high enough to prevent the tumor sample from drying out, and low enough to prevent the tumor sample from floating. A 30 minute emission scan of a single bed position was made on a microPET scanner (Siemens Inveon, Knoxville, USA). The PET scans were reconstructed using the OSEM3D algorithm (2 iterations) and the Maximum A Posteriori (MAP) algorithm (18 iterations). The smoothing factor was set to 0.8 mm, the matrix was 256 resulting in a voxel size of 0.4 mm. The resulting images were analyzed using the Siemens Inveon Research Workplace software. For each tumor slice the mean uptake concentration in kBq/mL divided by the activity concentration in the culture medium was calculated by drawing ROIs around the tumor slice.

3.2.4. Fixation, sectioning and immunostaining

After PET acquisition, tumor slices were fixed in 10% neutral buffered formalin for at least 24 hours at room temperature. Subsequently, tumor slices were embedded in paraffin and from each 300 μm thick tumor slice, three 4 μm sections were generated for microscopy analysis at approximately 50 μm, 150 μm and 250 μm of the tumor slice. For optimizing medium conditions, EdU incorporation was visualized using Click-It chemistry (Invitrogen) by incubating samples for 30 minutes with freshly made Click-It Alexa Fluor 594 cocktail (manufacturers protocol). Samples were mounted using Vectashield mounting medium with DAPI. Standardized double immunohistochemistry staining was performed using primary antibodies.

3.2.5. Pathologic examination by an automated detection method

Introduction

A script was created which automatically detected and counted the number of Ki-67 positive cells in histology images. The performance of the script was examined and validated by a pathologist in order to create an unbiased cell counting method. The validation of the script was performed based on a validation protocol, explained later in this section. The data set concerned ten NSCLC tumors, each composed of multiple tumor slices with multiple coupes.

Extraction of 40x magnification histology images

High resolution images of the histology samples were obtained using the Hamamatsu NanoZoomer Slide. 40x magnification images were taken. Their output was visually assessed with the NDPITools software in ImageJ to ensure no abnormalities [23].

Method

Validation of the script started with the extraction of random regions of interest from the 40x magnification histology images in order to create an unbiased methodology. At first, a script was created to produce regions of interest of 250 x 250 μm. These dimensions permitted an easy observation of the complex structures in the histology images, allowing easy manual counting by the pathologist. Secondly, the selection of the first ROI of each tumor slice was accomplished by the assessment of a

random starting point within 500 x 500 pixels from the upper left corner of each image. The remaining ROIs were selected in a systematic way. In order to prevent the acquirement of validation images in which no tumor tissue was visible, the area of tumor tissue visible with respect to the total area in a ROI was determined. The minimal required tumor tissue area within a ROI was set to 75% since this creates a large pool of ROIs to randomly select from. In the case a region of interest contained a low density of tumor tissue – which is often the case due to a lot of gaps present in the tissue – the 75% boundary still creates a few images to apply the random selection to, so this boundary makes a good compromise. Out of this pool of images, a ROI is selected randomly and the validation image was saved.

Automated detection method

The automated detection method was developed in ImageJ. The RGB histology images were splitted according to their color channels. The red channel was assessed, allowing the highest contrast, and a threshold was visually set to detect Ki-67 proliferating cells. The optimization of the threshold value was achieved by back and forth comparing of the result with the pathologist. The Ki-67 positive cells were counted based on an area range of 1.963×10^{-7} to 4.909×10^{-6} cm² per cell with a diameter of 5 μm and 25 μm respectively. The circularity was chosen to vary between 0.50-1.00.

Validation Protocol

For each validation image the pathologist manually counted the Ki-67 positive cells in tumor tissue and stroma tissue and manually registered the numbers in a database. The automated detection method was implemented on the validation images. Subsequently, the automatically counted number of positive cells by the script (tumor and stroma separated) was compared with the manually counted number of positive cells by the pathologist. This protocol was first applied on a set of images used as training set. The performance of the script was intensively discussed with the pathologist and adjusted to meet the requirements of the pathologist as much as possible. This resulted in an optimized version of the detection method which was then applied on a new set of images, the test set. The performance of the script with respect to the pathologist was assessed by a fitted regression line. Validity of the regression fit was evaluated through an R-squared metric.

3.2.6. Automated viability assessment

The detection of metabolically active regions was approached by the division of tumor tissue with stroma tissue based on the immunohistochemical staining with keratin. For this assessment, the same approach was used as in the automated detection method. Tissue slices were assessed in ImageJ at 40x magnification. The first step was to calculate the total number of proliferating cells in the whole coupe, of which a mask was created and saved: a mask of Ki-67 positive cells. By the application of a color thresholder program on the original image the separation of keratin stained areas from stroma (unstained) areas was achieved. The appropriate threshold was applied, following by the application of a dilation operator and the closing of holes. The result included a mask representing the keratin positive areas and was combined with the mask of the Ki-67 positive cells. Overlapping regions of Ki-67 positive cells with the positive keratin mask were detected. In this way the positive cells that were present at boundaries of keratin positive areas were included to tumor tissue. This image was called the division image. By adding up the original image with the division image, a stroma version of the original image was created. By inverting the division image and adding it with the original image, a tumor version of the image was created. Of both the tumor and stroma image the number of proliferating cells was determined. Again, the performance of the division between tumor tissue with stroma tumor was intensively discussed with the pathologist and adjusted to meet the requirements of the pathologist as much as possible.

3.2.7. Linear Mixed-Effects Regression Modeling

A linear mixed-effects regression analysis was performed for the correlation between FDG uptake and the number of vital tumor cells per slice by the use of Matlab. A linear mixed-effects regression model was used to investigate data of multiple groups and fit it simultaneously. The model was able to account for the fact that FDG uptake in multiple tumor slices of the same patient differ from FDG uptake in multiple tumor slices of other patients. The linear mixed-effects model was described by the following formula:

$$y_j = X_j\beta + Z_j b_j + \epsilon_j \tag{3.1}$$

which was associated with fixed and random parameters including independent and dependent errors [9]. The parameter y_j equaled the response variable denoted by the mean activity. This was the dependent variable measured per observation. The predictor variable X_j was the independent variable

and included the number of proliferating cells present in viable tumor tissue with an accompanying vector of the fixed-effects regression coefficients: β. The parameter Z_j included all random factors that affect the uptake of FDG that are uncontrollable and were compared between patients (the grouping variable Z), with a vector of random regression parameters b_j. The residuals are denoted by ϵ [12]. The significance of the inclusion of random effects in this model was verified by the use of a Likelihood Ratio Test. The Likelihood Ratio Test compared a model with and without random effects. Correlations were considered statistically significant at $p < 0.05$.

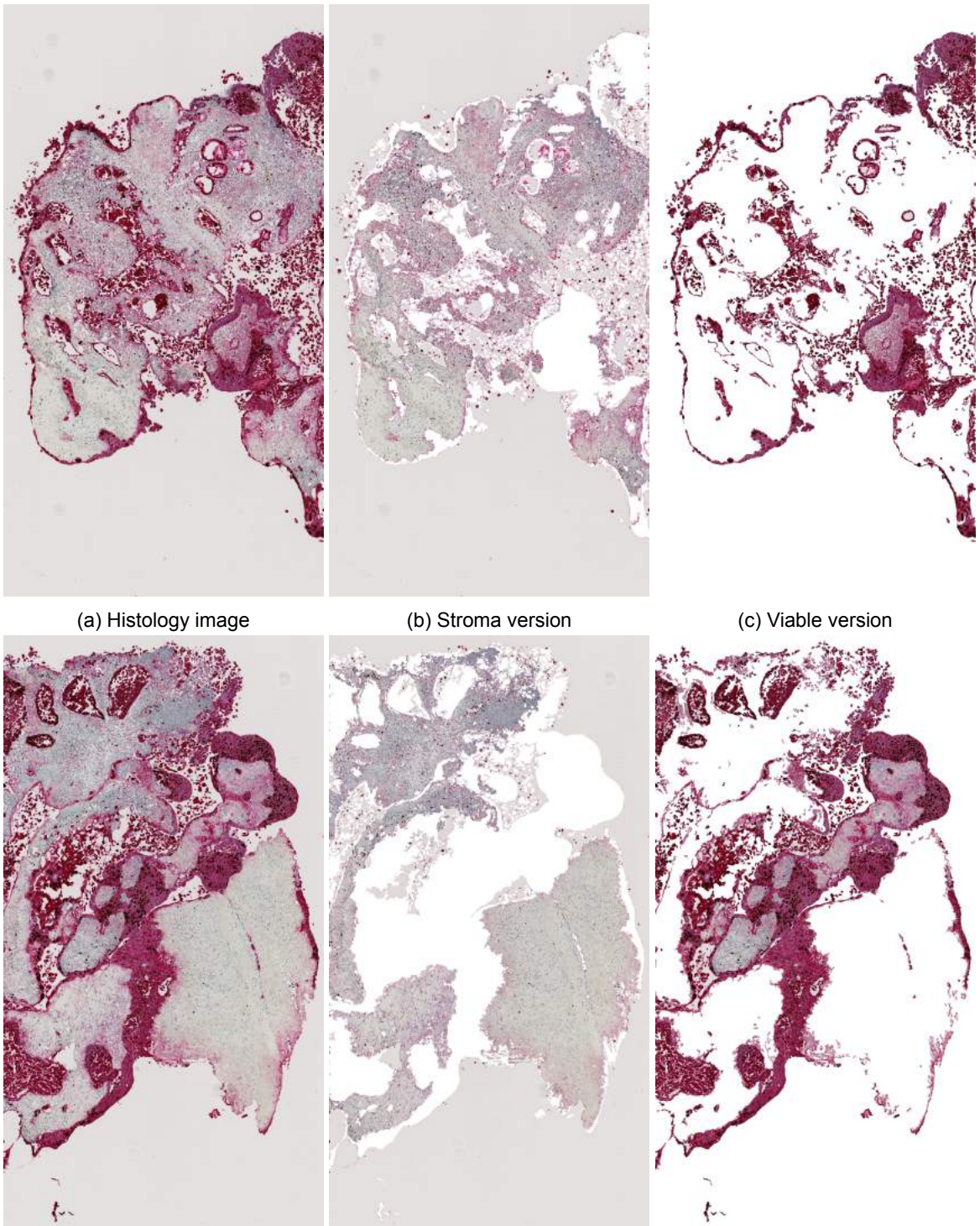

(a) Histology image (b) Stroma version (c) Viable version

(d) Histology image (e) Stroma version (f) Viable version

Figure 3.2: Example automated viability assessment

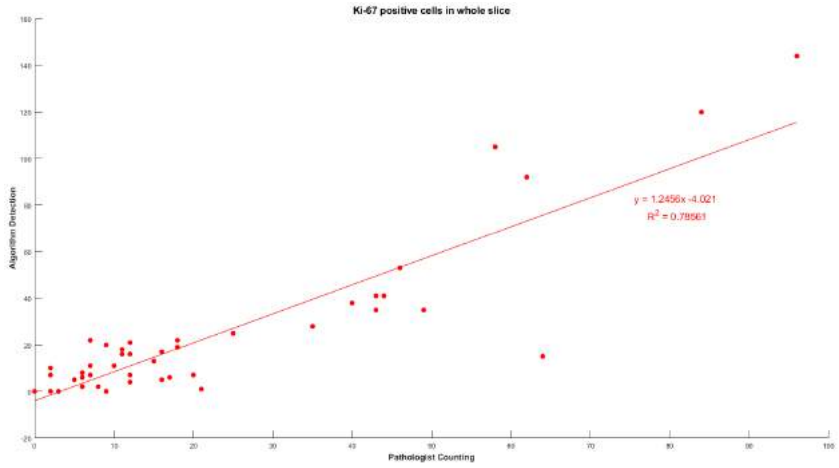

Figure 3.3: Detection method vs. pathologist - total Ki-67 positive cells

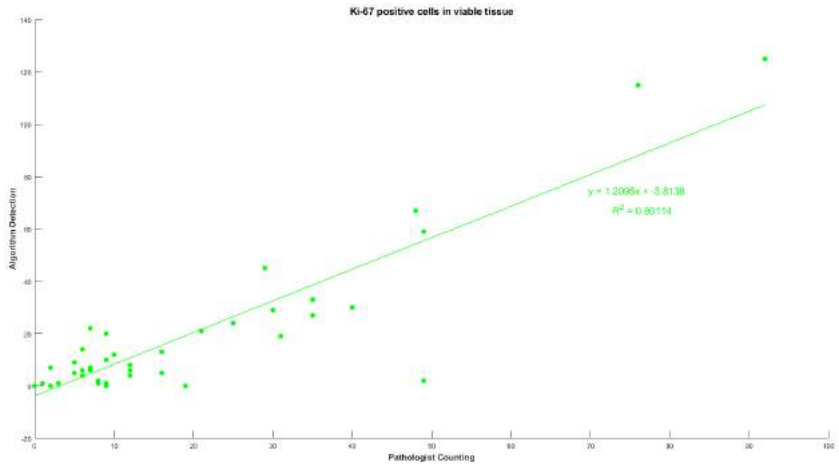

Figure 3.4: Detection method vs. pathologist - Ki-67 positive cells in viable tissue

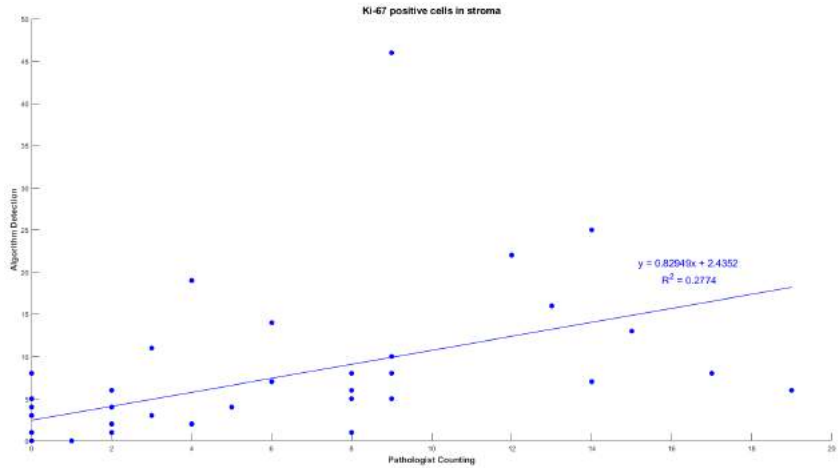

Figure 3.5: Detection method vs. pathologist - Ki-67 positive cells in stroma tissue

3.3. Results

3.3.1. Automated detection method

An example of the performance of the automated detection method on a histology image is shown in figure 3.6. Three randomly selected regions are extracted in which the detection algorithm is applied. The yellow contours show the detection of the Ki-67 positive cell nuclei.

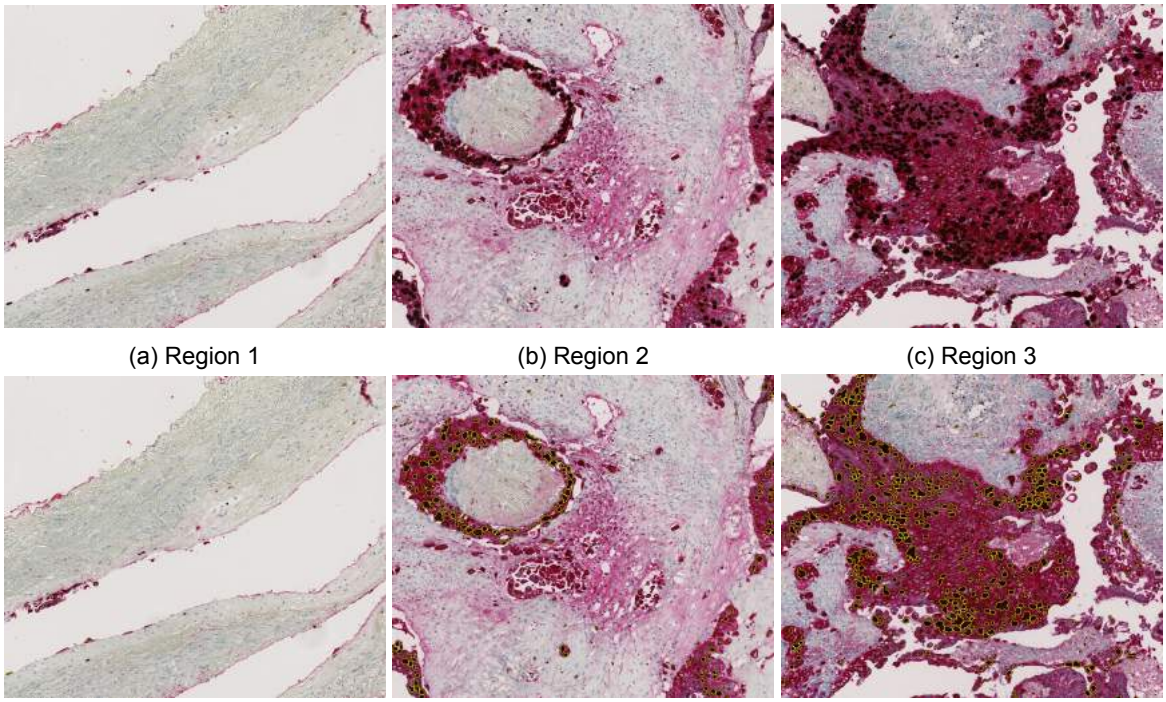

(a) Region 1 (b) Region 2 (c) Region 3

(d) Detection in region 1 (e) Detection in region 2 (f) Detection in region 3

Figure 3.6: Example performance detection algorithm

3.3.2. Automated viability assessment

The performance of the analysis of metabolically active regions by the developed method was visually clarified in figure 3.2. The figures 3.2a and 3.2d show part of a histology image. Figures 3.2b and 3.2e show the stroma version of the tumor slice and figures 3.2c and 3.2f show the metabolically active regions of the tumor slice.

3.3.3. Validation protocol

The performance of the script with respect to the pathologist is assessed by a fitted regression line of which the results are shown in figures 3.3, 3.4 and 3.5. For the number of Ki-67 positive cells in the total slice, in viable tissue and in stroma tissue, the R^2 values equal $R^2 = 0.786$, $R^2 = 0.801$ and $R^2 = 0.278$ respectively.

3.3.4. Statistical analysis

For each patient, the mean activity uptake per tumor slice is compared to the number of proliferating cells in viable tissue. This relation is visualized in scatter plots with fitted regression lines per patient in one graph shown in figure 3.7. The scatter plots suggest different slopes and intercepts of FDG uptake against proliferating cells per patient. This is the motivation behind the implementation of a random intercept and slope model, assuming a possible correlation between them. The result of the Likelihood Ratio Test to verify the significance of the inclusion of random effects in our model gives a p-value of $0.0036272 < 0.05$. This indicates the significance of random effects in the linear mixed-effects model. The estimate of the linear-mixed effects model is 4.2825 for the fixed-effects regression coefficient β, based on a 95% confidence interval (CI). Random effects covariance parameters based on a confidence interval of 95% show a residual standard deviation of 17138 Bq, indicating large variations between individual patients. The p-value for the fixed effects (95% CIs) equals 0.31451, indicating that the number of proliferating cells does not significantly accounts for variation in FDG uptake.

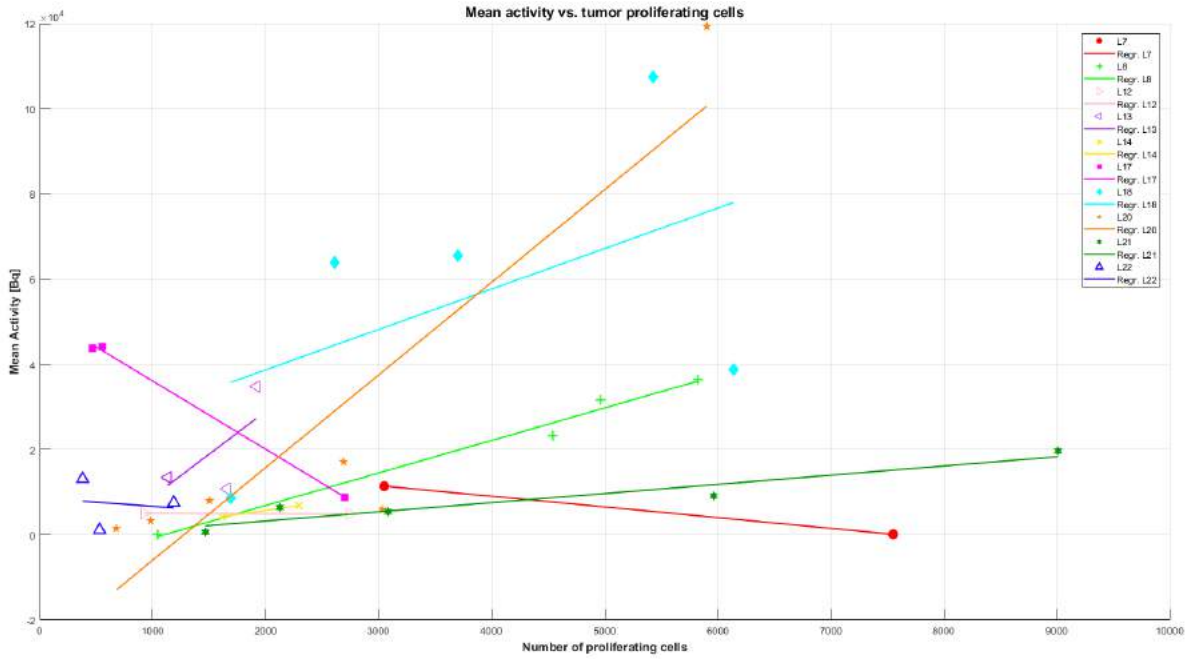

Figure 3.7: Fitted regression lines per patient, expressed in mean activity against number of proliferating cells

3.4. Discussion & Conclusion

In the presented work, an experimental procedure was developed to validate the FDG-PET imaging tracer for response assessment of NSCLC patients *ex vivo*. Measuring response non-invasively *in vivo* by FDG-PET to identify resistant regions is a generally used methodology in NSCLC treatment. Escalating dose to poorly responding regions may increase local tumor control whilst minimizing the occurrence of possible side effects [2]. Whether FDG could be useful to noninvasively identify differences in response should be validated by correlating uptake with the number of proliferating cells. NSCLC slices have been shown to remain vital *ex vivo* for at least 7 days [63] and can thus be employed for direct *ex vivo* comparison of FDG uptake and pathologic examination. Using this procedure, the correlation between FDG uptake and the number of proliferating tumor cells was investigated by the use of a linear mixed-effects model.

For the assessment of the number of proliferating tumor cells, the development of an automated detection method was proven feasible together with the detection of metabolically active regions. This methodology was widely accomplished in breast cancer studies [28, 43, 62] but limited in lung cancer studies [51], making the presented study of added value in this research area. Validation of the detection method was accomplished by a pathologist whereupon a regression analysis was performed.

The regression analysis based on the R^2 metric gave a rough interpretation how well the developed script fitted with the pathologists manual counting results. A main question is how large R^2 needs to be for the regression to be valid. The fit regarding the number of cells in the whole slice and the tumor tissue gave relative high R^2 values compared to R^2 values for stroma tissue. This was explained by the small amount of proliferating cells meaning that a counting error between the script and the pathologist has a larger consequence in stroma tissue than in tumor tissue. Another explanation was that an exact agreement of the counting results was used of which one may discuss the extent of this problem since a difference of a few cells for large quantities may not be harmful. The great benefit of unbiasedness in cell counting across all tumors was the most important argument to make use of an automated detection method. Since the R^2 metric doesn't tell the entire story, the R^2 values could be further evaluated with residual plots and other model statistics like Light's kappa to investigate agreement between observers [44], and Cohen's kappa [34]. The method could be improved by selecting a certain range in which the counted number was valid instead of using an exact agreement of the counting results.

The result of the linear mixed-effects regression model showed an overall weak but positive correlation between FDG uptake and the number of proliferating cells with a large variation between individual patients. The p-value indicated that the number of proliferating cells does not significantly accounts for variation in FDG uptake. The diverse outcomes that were observed between patients are explained by the numerous other biological characteristics that influence FDG uptake in cancerous tissue. Biological characteristics include the existence of hypoxia and enhanced levels of glucose transporters and glucose metabolism regulators [54, 93]. The correlation of FDG uptake with hypoxia inducible factor-1α and GLUT-1 in NSCLC was confirmed by van Baardwijk et al. [84]. The fact that FDG uptake in NSCLC does not reflect proliferation, but is influenced by therapy-resistant pathways was already mentioned by [2]. Further explanation is found in the comparison between FDG, a marker for metabolic activity with Ki-67, a proliferation marker. The radiotracer FDG was a good candicate for this study. However, the use of for example [^{18}F]-FLT, a marker for proliferation or [^{18}F]-misonidazole should be considered.

A weak point in the assessment of *ex vivo* FDG uptake is that response *ex vivo* might not be the same as response *in vivo* despite the mimicking of tumor (micro)environment. Factors could be difficulties in the access to nutrients or adapted behavior of signal molecules at the edges of the slices. This is an element which must be explored in further research.

The presented investigation implicates that FDG uptake in tumor slices does not significantly reflects the number of proliferating cells. Therefore, FDG is not a highly selective tracer for response based imaging during radiotherapy treatment in NSCLC.

4

Future Perspective

The preceding chapters presented the work of the characterization of the microPET scanner by the use of 3D-printed phantoms in combination with the *ex vivo* validation of FDP-PET uptake with pathological examination in non-small cell lung cancer. This work was performed in order to explore the capabilities of the microPET scanner in detecting FDG uptake differences at a small scale and contribute to the development of FDG-PET imaging during radiotherapy treatment in NSCLC patients. This chapter describes work that has been done but was not completely finished, therefore offering future perspectives regarding this Master Thesis.

Regarding chapter 3 of this Master Thesis, analysis have been done on the intra-slice comparison of the number of proliferating cells per unit area in the tumor tissue with FDG uptake values per unit area in (2D) PET images. The first step that was performed included the creation of a heatmap of the histology sections, indicating the extent of proliferating cells per unit area in the histology sections. This unit area could be based on the scanner's spatial resolution or on the dimensions of the PET pixels. An example was shown in figure 4.1a in which a histology slice is shown. For this slice the number of proliferating cells was calculated for areas of 250 μm x 250 μm and expressed in number of proliferating cells per mm^2 visualized by a heatmap in figure 4.1b. Figure 4.1c shows the overlay of the histology slice with the accompanying heatmap of the proliferating cells/mm^2. Dark squares indicate a low number of proliferating cells present in that area. Bright squares indicate a high number of proliferating cells present in that area. The following step included the 2D cross-correlation of the PET data of the concerned tumor slice with the histology image for a perfect overlay. This step has not been succeeding and is the main step for future research. The concluding step would include the assessment of the number of proliferating cells per unit area with FDG uptake in the accompanying area.

Regarding Chapter 2 of this Master Thesis, the deblurring technique has been applied on PET images of tumor specimens. An example of a PET image of a tumor specimen is shown in figure 4.2a. A deblurred version is shown in figure 4.2b on which the deblurring technique was applied. Deblurred versions of PET tumor slice data will serve as more accurate representations of the tumor slices which was proven by phantom experiments in chapter 2 of this Master Thesis.

Regarding the quantification of the PET phantom experiments, there must be a comprehensive look at the absolute activity concentrations in the phantoms. A selection of elements that require extensive elaboration include the exact improvement of the spatial resolution, alignment of the computational phantom with measured data by the use of a high resolution approach, the positron range effect and streaking artifacts as a result of image deblurring.

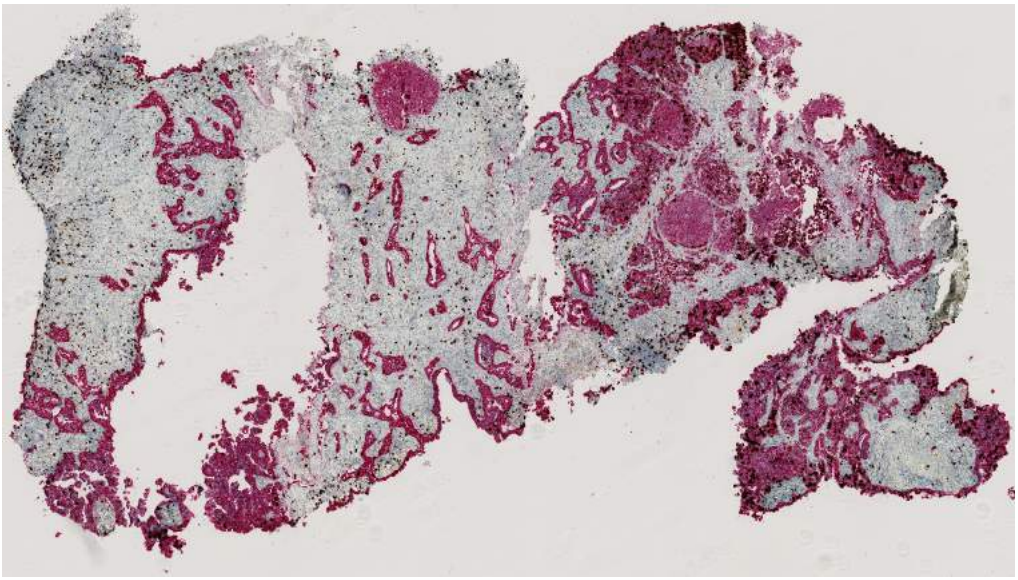

(a) Histology slice

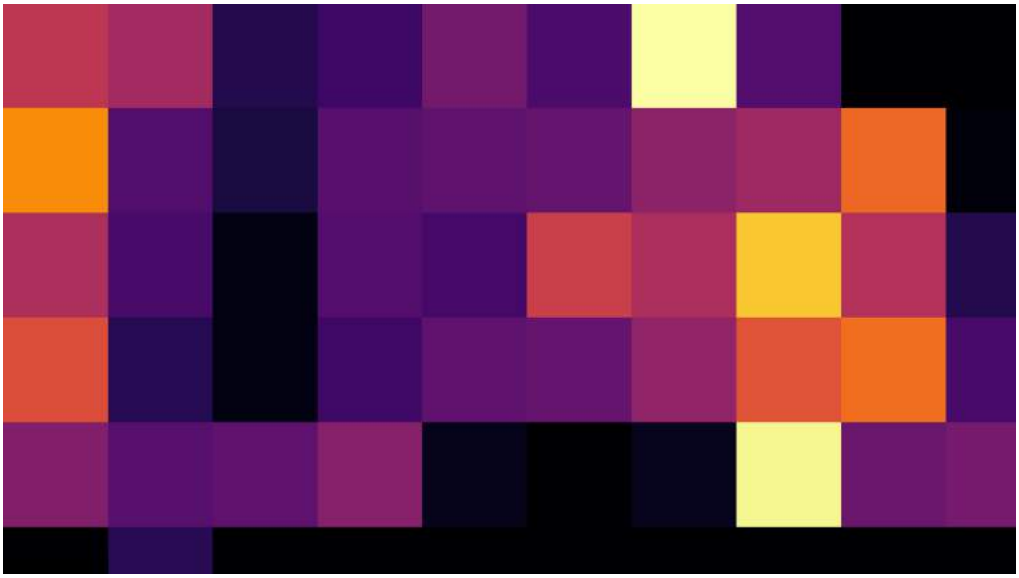

(b) Heatmap proliferating cells per mm^2

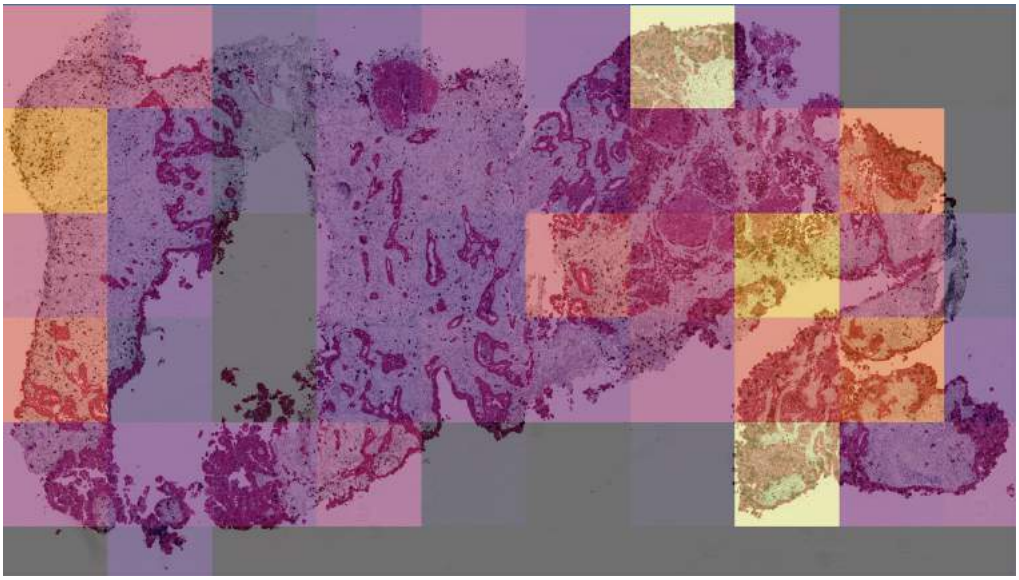

(c) Overlay histology slice with accompanying heatmap

Figure 4.1: Histology slice with accompanying heatmap

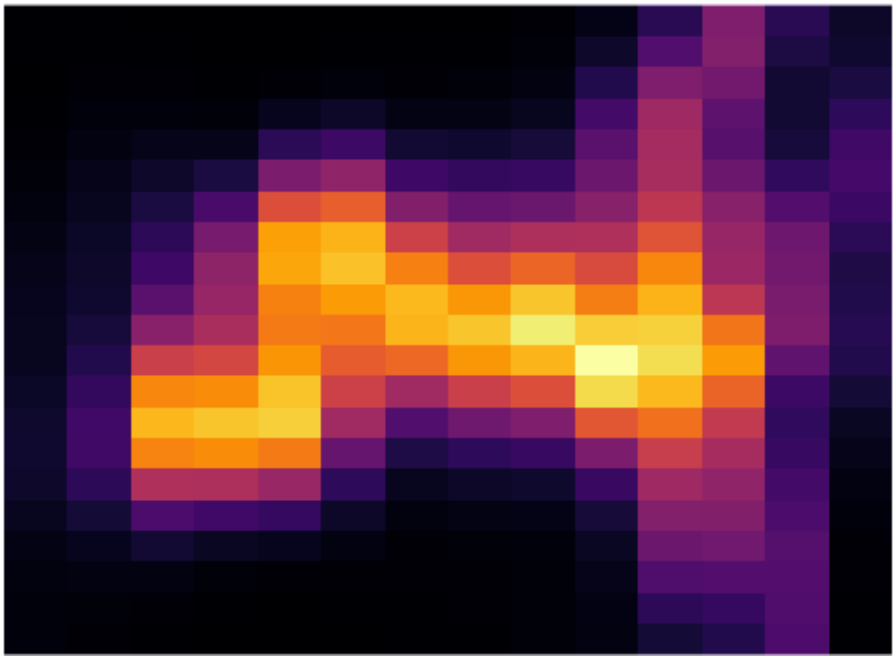

(a) PET image tumor slice

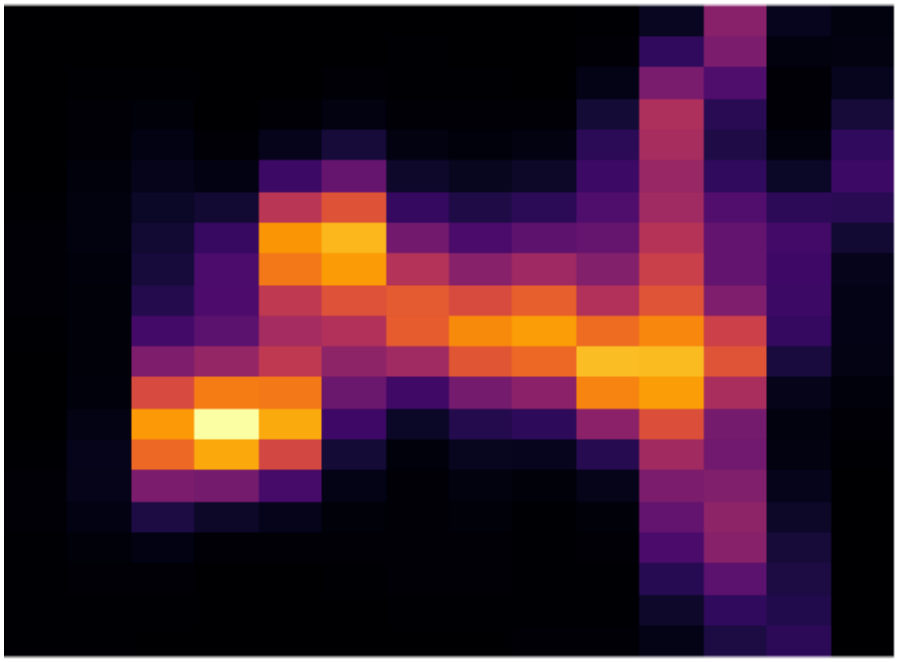

(b) Deblurred PET image tumor slice

Figure 4.2: Example of PET data tumor specimen and deblurred version

5

Appendix

PSF Estimation

```
[V_S,spatial_S,dim_S] = dicomreadVolume('/media/celebrity/Seagate Backup Plus ...
    Drive/MEP/PET experiments/PET_phantoms/OSEM3D+MAP/Phantom ...
    snake/20180419_snake_OSEM3D-MAP/...
1.2.826.0.1.3417726.3.859524741/...
1.2.826.0.1.3417726.3.532305.20180830121010453');
V1_S = squeeze(V_S);

Num_slices =  size(V1_S,3);

for i = 1:Num_slices
    E_S = sum(V1_S(i,:,:),1);
    E_S = permute(E_S,[2 3 1]);
    E_S(E_S<0) = 0;
    max_slice(i) = max(max(E_S(97:152,58:96)));
end
[slice, index] = sort(max_slice(:),'descend');
top = index(1:4);
disp(top');
disp(max_slice(top));

pixeldepth_S = 0.388192;
H_stack = pixeldepth_S*size(top,1);
H_voxel = H_stack/numel(top)/10;
E_S = (sum(V1_S(138:141,:,:),1))*H_voxel;
E_S = permute(E_S,[2 3 1]);

RescaleSlope_S = 8.0059989584E2;
RescaleIntercept_S = 0;
E_S = E_S*RescaleSlope_S + RescaleIntercept_S;

pixeldepth_S = 0.388192;
slicedepth_S = 0.796;
scale_S = slicedepth_S/pixeldepth_S;

figure; axis equal; imagesc(A);
colormap(inferno);
axis image off;
set(gca, 'dataAspectRatio',[pixeldepth_S slicedepth_S 1]);

max_E_S = max(max(E_S));
E_S_norm = E_S./max_E_S;

max_Ideal = max(max(Ideal));
Ideal_norm = Ideal./max_Ideal;

Sx = 0.1:0.1:20;
Sy = 0.1:0.1:20;

for k = 1:numel(Sx)
    for l = 1:numel(Sy)
        S_blurred = imgaussfilt(Ideal_norm, [Sx(k) Sy(l)], 'Padding', ...
            'symmetric','FilterDomain','auto');

        A = (abs((E_S_norm-S_blurred))).^2;
        A_x = sum(A,2)./y_Ideal;
        A_xy = sum(A_x)./x_Ideal;

        B = (abs(E_S_norm)).^2;
        B_x = sum(B,2)./y_Ideal;
        B_xy = sum(B_x)./x_Ideal;
        RMSD(k,l) = sqrt(A_xy./B_xy);
    end
end

[Sx_max, Sy_max] = ind2sub(size(RMSD),find(RMSD==min(min(RMSD))));
fprintf('Lowest RMSD is %10.8f. ',RMSD(Sx_max, Sy_max));
fprintf('STDDEV in x is %10.5f. ',Sx(Sx_max));
```

```
fprintf('STDDEV in y is %10.5f. ',Sy(Sy_max));

range = 0.3;
SSx = (Sx(Sx_max)-range):0.01:(Sx(Sx_max)+range);
SSy = (Sy(Sy_max)-range):0.01:(Sy(Sy_max)+range);

for k = 1:numel(SSx)
    for l = 1:numel(SSy)
        S_blurred_opt = imgaussfilt(Ideal_norm, [SSx(k) SSy(l)], 'Padding', ...
            'symmetric','FilterDomain','auto');

        A = (abs((E_S_norm-S_blurred_opt))).^2;
        A_x = sum(A,2)./y_Ideal;
        A_xy = sum(A_x)./x_Ideal;

        B = (abs(E_S_norm)).^2;
        B_x = sum(B,2)./y_Ideal;
        B_xy = sum(B_x)./x_Ideal;
        RMSD_range(k,l) = sqrt(A_xy./B_xy);
    end
end
[Sx_max_2, Sy_max_2] = ind2sub(size(RMSD_range),find(RMSD_range==min(min(RMSD_range))));
fprintf('Lowest RMSD is \%10.8f. ',RMSD_range(Sx_max_2, Sy_max_2));
fprintf('STDDEV in x is \%10.5f. ',SSx(Sx_max_2));
fprintf('STDDEV in y is \%10.5f. ',SSy(Sy_max_2));
[x_Ideal,y_Ideal] = size(Ideal);

A = (abs((Ideal_norm-E_S_norm))).^2;
A_x = sum(A,2)./y_Ideal;
A_xy = sum(A_x)./x_Ideal;

B = (abs(Ideal_norm)).^2;
B_x = sum(B,2)./y_Ideal;
B_xy = sum(B_x)./x_Ideal;
RMSD_dblvsbi = sqrt(A_xy./B_xy);
disp(RMSD_dblvsbi);

PSF_x_R = 2*ceil(2*SSx(Sx_max_2))+1;
PSF_y_R = 2*ceil(2*SSy(Sy_max_2))+1;

PSF_size_R = ones(PSF_x_R,PSF_y_R);
V = .0001;
WT = edge(Ideal,'Sobel');
WT(5:end-4,5:end-4) = 1;

E_blurred = imgaussfilt(Ideal_norm, [SSx(Sx_max_2) SSy(Sy_max_2)],'Padding', ...
    'symmetric','FilterDomain','auto');

for i = 1:10
    J_R = deconvblind(E_blurred,PSF_size_R,i);
    J_R_max = max(max(J_R));
    J_R_norm = J_R./J_R_max;
    C = (abs((Ideal_norm-J_R_norm))).^2;
    C_x = sum(C,2)./y_Ideal;
    C_xy = sum(C_x)./x_Ideal;

    D = (abs(Ideal_norm)).^2;
    D_x = sum(D,2)./y_Ideal;
    D_xy = sum(D_x)./x_Ideal;
    RMSD_blnd(i) = sqrt(C_xy./D_xy);
end
[ssrS,sndS] = min(RMSD_blnd);
[ijS,jiS] = ind2sub(size(RMSD_blnd),sndS);
disp(sndS)
figure;
plot(RMSD_blnd);
hold on
plot(sndS,ssrS,'or')
hold off
text(sndS*1.05,ssrS,'Minimum')

```

```
134 [J_R,PSF_rec_R] = deconvblind(E_blurred,PSF_size_R,sndS);
135 DEBL_E_S2 = deconvlucy(E_S,PSF_rec_R,5,sqrt(V));
136
137 E_S_counts = sum(sum(E_S,1));
138 DEBL_E_S2_counts = sum(sum(DEBL_E_S2,1));
139 Delta_ESDBL = 1-abs(E_S_counts-DEBL_E_S2_counts)/DEBL_E_S2_counts;
140 DEBL_E_S_REN = DEBL_E_S2.*Delta_ESDBL;
141
142 xi = [59 94];
143 yi = [132 132];
144 improfile(Ideal,xi,yi,10000,'nearest');
145 xi = [59 94];
146 yi = [132 132];
147 improfile(E_S,xi,yi);grid on; hold on
148 xi = [59 94];
149 yi = [132 132];
150 improfile(DEBL_E_S_REN,xi,yi);
151
152 ptsOriginal  = detectSURFFeatures(Ideal);
153 ptsDistorted = detectSURFFeatures(DEBL_E_S1_n);
154
155 [featuresOriginal,   validPtsOriginal]  = extractFeatures(Ideal,  ptsOriginal);
156 [featuresDistorted, validPtsDistorted] = extractFeatures(DEBL_E_S2, ptsDistorted);
157
158 indexPairs = matchFeatures(featuresOriginal, featuresDistorted);
159 matchedOriginal  = validPtsOriginal(indexPairs(:,1));
160 matchedDistorted = validPtsDistorted(indexPairs(:,2));
161
162 figure;
163 showMatchedFeatures(Ideal,DEBL_E_S2,matchedOriginal,matchedDistorted);
164 title('Overlay ideal vs. deconvolved data - SNAKE - OSEM3DMAP');
165
166 [tform, inlierDistorted, inlierOriginal] = estimateGeometricTransform(matchedDistorted, ...
      matchedOriginal, 'similarity');
167
168 C = normxcorr2(Ideal,DEBL_E_S1_n);
169 figure, surf(C), shading flat
170
171 [ypeak, xpeak] = find(C==max(C(:)));
172 yoffSet = ypeak-size(Ideal,1);
173 xoffSet = xpeak-size(Ideal,2);
174
175 figure;
176 imagesc(Ideal);
177 colormap('gray');
178 axis equal
179 axis image off
180 set(gca, 'dataAspectRatio',[1 1 1]);
181 imrect(gca, [xoffSet+1, yoffSet+1, size(Ideal,2), size(Ideal,1)]);
```

Validation protocol with ROI extraction

```
//random selection of region of interest to use for the validation
getDimensions(width, height, channels, slices, frames);
dir = getDirectory("image");
name = getTitle();
tile_x = 1098;       //1 pixel is 0.00002277 cm dus 500 um zijn 2195 pixels (naar ...
    beneden afgerond)
tile_y = 1098;       //dus 250 um is 1098 pixels (naar boven afgerond)
numTiles = 2 //percentage of samples
numRow = ((height/tile_x)/numTiles);
numCol = ((width/tile_x)/numTiles);

for(i = 0; i < numRow; i++)
{
    for(j = 0; j < numCol; j++)
    {    if (i == 0 && j == 0) {
        xOffset1 = (numTiles * random * j * (tile_x)) + random*500;
        yOffset1 = (numTiles * random * i * (tile_y)) + random*500;
        makeRectangle(xOffset1, yOffset1, tile_x, tile_y);
        roiManager("Add");
    } else {
        xOffset = numTiles * j * (tile_x) + xOffset1;
        yOffset = numTiles * i * (tile_y) + yOffset1;
        makeRectangle(xOffset, yOffset, tile_x, tile_y);
        roiManager("Add");
    }
}
}
roiManager("show all with labels")
print("The number of ROIs in the image are " + roiManager("count"));

//Determination of the ROI's with tumor area above 75%
for(k = 0; k < roiManager("count"); k++){
    roiManager("select", k);
    run("Duplicate...", title=Tile + k+1);
    run("Gaussian Blur...", "sigma=3");
    run("8-bit");
    setAutoThreshold("Default");
    setThreshold(205, 255);
    run("Convert to Mask");
    run("Invert");
    run("Analyze Particles...", "size=0-Infinity display clear include summarize");
    close();
}
}

\section*{Automated detection method \& viable tissue separation}
\mcode{
function action(input, filename){
open(input + filename);

//Counting positive cells TOTAL slice
title = getTitle();
run("Duplicate...", "title=[title]");
run("Split Channels");
close();
close();
run("Gaussian Blur...", "sigma=2");
setAutoThreshold("Default");
setThreshold(0, 65);
run("Convert to Mask");
run("Watershed");
run("Analyze Particles...", "size=0.0000001257-0.000004909 circularity=0.50-1.00 ...
    show=Masks clear summarize add");
rename("mask_pos_cells");
close(title + " (red)");

// Determine the area of the tissue in the image
```

```
66 selectWindow(title);
67 run("Duplicate...", "title=[Area total slice]");
68 run("Gaussian Blur...", "sigma=3");
69 run("8-bit");
70 setAutoThreshold("Default");
71 setThreshold(205, 255);
72 run("Convert to Mask");
73 run("Invert");
74 run("Analyze Particles...", "size=10000-Infinity clear include summarize add");
75 close();
76
77 //Division Tumor from Stroma
78 selectWindow(title);
79 run("Duplicate...", "title=[original image]");
80 selectWindow(title);
81 run("Gaussian Blur...", "sigma=2");
82 run("Color Threshold...");
83 // Color Thresholder 2.0.0-rc-43/1.52b
84 min=newArray(3);
85 max=newArray(3);
86 filter=newArray(3);
87 a=getTitle();
88 run("HSB Stack");
89 run("Convert Stack to Images");
90 selectWindow("Hue");
91 rename("0");
92 selectWindow("Saturation");
93 rename("1");
94 selectWindow("Brightness");
95 rename("2");
96 min[0]=211;
97 max[0]=255;
98 filter[0]="pass";
99 min[1]=65; //140 //85
100 max[1]=255;
101 filter[1]="pass";
102 min[2]=0;
103 max[2]=255;
104 filter[2]="pass";
105 for (i=0;i<3;i++){
106   selectWindow(""+i);
107   setThreshold(min[i], max[i]);
108   run("Convert to Mask");
109   if (filter[i]=="stop")  run("Invert");
110 }
111 imageCalculator("AND create", "0","1");
112 imageCalculator("AND create", "Result of 0","2");
113 for (i=0;i<3;i++){
114   selectWindow(""+i);
115   close();
116 }
117 selectWindow("Result of 0");
118 close();
119 selectWindow("Result of Result of 0");
120 rename(a);
121 // Colour Thresholding-------------
122 run("Make Binary");
123 run("Fill Holes");
124 rename("mask_stromatumor");
125
126 //Combine positive cells + tumor/stroma
127 imageCalculator("Add create", "mask_pos_cells", "mask_stromatumor");
128 run("Analyze Particles...", "size=0.000001-Infinity circularity=0-0.75 show=Masks"); ...
      //hogere ondergrens?
129 rename("division");
130 run("Dilate");
131 run("Fill Holes");
132 close("mask_pos_cells");
133 close("mask_stromatumor");
134
135 //Counting positive cells in TUMOR
```

```
136 imageCalculator("Add create", "original image", "division");
137 rename("tumor");
138 run("Duplicate...", " ");
139 tumor_2 = getTitle();
140 run("Split Channels");
141 close();
142 close();
143 selectWindow(tumor_2 + " (red)");
144 run("Gaussian Blur...", "sigma=2");
145 setAutoThreshold("Default");
146 setThreshold(0, 65);
147 run("Convert to Mask");
148 run("Watershed");
149 run("Analyze Particles...", "size=0.0000001257-0.000004909 circularity=0.50-1.00 ...
        summarize");
150 close(tumor_2 + " (red)");
151
152 //Counting positive cells in STROMA
153 selectWindow("division");
154 run("Invert");
155 imageCalculator("Add create", "original image", "division");
156 rename("stroma");
157 close("division");
158 run("Duplicate...", " ");
159 stroma_2 = getTitle();
160 run("Split Channels");
161 close();
162 close();
163 selectWindow(stroma_2 + " (red)");
164 run("Gaussian Blur...", "sigma=2");
165 setAutoThreshold("Default");
166 setThreshold(0, 65);
167 run("Convert to Mask");
168 run("Watershed");
169 run("Analyze Particles...", "size=0.0000001257-0.000004909 circularity=0.50-1.00 ...
        summarize");
170 close(stroma_2 + " (red)");
171 run("Close All");
172 }
```

Linear Mixed-Effects Modeling

```
Activity = [11431.59805; 136.31303; 23175.936; 36504.383; 31711.744; 16.12335; ...
    698315.8; 560333.94; 341344.41; 4890.76233; 5039.49173; 13442.385; 10784.34; ...
    13514.74071; 34775.04; 4239.054; 6847.41; 43827.2; 44100; 8860.8; 8712; 65573.9; ...
    107419.5; 63913.2; 38734.5; 1519.60326; 5961.6; 3314.0975; 17152; 8016; 119314; ...
    9118.6; 19686.4; 657.01857; 5410.8; 6397.597; 1153.26232; 7524; 13130];
Total_cells = [3956 8522 5692 6913 5652 4390 988 755 1458 3023 1450 2473 3838 3355 3138 ...
    2676 3934 552 687 2862 1886 4383 6103 2886 6635 1198 5173 2063 5836 2006 7837 7066 ...
    12657 2563 3468 5173 787 2019 724];
Tumor = [3049; 7550; 4540; 5820; 4963; 1044; 518; 516; 1165; 2745; 925; 1132; 1655; ...
    1137; 1916; 1614; 2296; 465; 554; 2698; 1688; 3698; 5430; 2611; 6139; 679; 3030; ...
    982; 2688; 1504; 5901; 5963; 9009; 1467; 3084; 2125; 531; 1186; 380];
Stroma = [907 972 1152 1093 689 3346 470 239 293 278 525 1341 2183 2218 1222 1062 1638 ...
    87 133 164 198 685 673 275 496 519 2143 1081 3148 502 1936 1103 3648 1096 384 3048 ...
    256 833 344];
Patients = cellstr(['L07';'L07';'L08';'L08';'L08';'L08';'L10';'L10';'L10';'L12';'L12';...
'L13';'L13';'L13';'L13';'L14';'L14';'L17';'L17';'L17';'L18';'L18';'L18';'L18';'L18';...
'L20';'L20';'L20';'L20';'L20';'L20';'L21';'L21';'L21';'L21';'L21';...
'L22';'L22';'L22']);

Activity(7:9,:) = [];
Tumor(7:9,:) = [];
Patients(7:9,:) = [];

BigAnalysis = table(Patients,Tumor,Activity);
BigAnalysis.Patients = categorical(BigAnalysis.Patients);

figure;
gscatter(BigAnalysis.Tumor,BigAnalysis.Activity,BigAnalysis.Patients,[],'.',25);
hold on
title('Simple linear model fit','FontSize',15)
xlabel('Number of proliferating cells','FontSize',15)
ylabel('Activity','FontSize',15)

clc
lme_intercept = fitlme(BigAnalysis,'Activity ~ Tumor');
lme_intercept_slope = fitlme(BigAnalysis,'Activity ~ Tumor + (1+Tumor|Patients)');

[~,~,rEffects] = randomEffects(lme_intercept_slope);

figure,
scatter(rEffects.Estimate(1:2:end),rEffects.Estimate(2:2:end))
title('Random Effects','FontSize',15)
xlabel('Intercept','FontSize',15)
ylabel('Slope','FontSize',15)

compare(lme_intercept, lme_intercept_slope, 'CheckNesting',true)
lme_matrix = fitlmematrix(X,y,Z,G,'CovariancePattern','Diagonal');
```

Example figures of merit 4x4 phantom

```
%% Compartments quantitative analysis ideal phantom

comp11_ID = ID_4x4(117:122,76:78);
comp12_ID = ID_4x4(117:122,79:81);
comp13_ID = ID_4x4(117:122,82:84);
comp14_ID = ID_4x4(117:122,85:87);

comp21_ID = ID_4x4(123:128,76:78);
comp22_ID = ID_4x4(123:128,79:81);
comp23_ID = ID_4x4(123:128,82:84);
comp24_ID = ID_4x4(123:128,85:87);

comp31_ID = ID_4x4(129:134,76:78);
comp32_ID = ID_4x4(129:134,79:81);
comp33_ID = ID_4x4(129:134,82:84);
comp34_ID = ID_4x4(129:134,85:87);

comp41_ID = ID_4x4(135:140,76:78);
comp42_ID = ID_4x4(135:140,79:81);
comp43_ID = ID_4x4(135:140,82:84);
comp44_ID = ID_4x4(135:140,85:87);

mu11_ID = mean2(comp11_ID); mu12_ID = mean2(comp12_ID); mu13_ID = mean2(comp13_ID); ...
    mu14_ID = mean2(comp14_ID);
mu21_ID = mean2(comp21_ID); mu22_ID = mean2(comp22_ID); mu23_ID = mean2(comp23_ID); ...
    mu24_ID = mean2(comp24_ID);
mu31_ID = mean2(comp31_ID); mu32_ID = mean2(comp32_ID); mu33_ID = mean2(comp33_ID); ...
    mu34_ID = mean2(comp34_ID);
mu41_ID = mean2(comp41_ID); mu42_ID = mean2(comp42_ID); mu43_ID = mean2(comp43_ID); ...
    mu44_ID = mean2(comp44_ID);

%% Quantitative analysis ROIs

comp11_EF = E_F(117:122,76:78);
comp12_EF = E_F(117:122,79:81);
comp13_EF = E_F(117:122,82:84);
comp14_EF = E_F(117:122,85:87);
comp11_DBL = DEBL_E_F_REN(117:122,76:78);
comp12_DBL = DEBL_E_F_REN(117:122,79:81);
comp13_DBL = DEBL_E_F_REN(117:122,82:84);
comp14_DBL = DEBL_E_F_REN(117:122,85:87);

comp21_EF = E_F(123:128,76:78);
comp22_EF = E_F(123:128,79:81);
comp23_EF = E_F(123:128,82:84);
comp24_EF = E_F(123:128,85:87);
comp21_DBL = DEBL_E_F_REN(123:128,76:78);
comp22_DBL = DEBL_E_F_REN(123:128,79:81);
comp23_DBL = DEBL_E_F_REN(123:128,82:84);
comp24_DBL = DEBL_E_F_REN(123:128,85:87);

comp31_EF = E_F(129:134,76:78);
comp32_EF = E_F(129:134,79:81);
comp33_EF = E_F(129:134,82:84);
comp34_EF = E_F(129:134,85:87);
comp31_DBL = DEBL_E_F_REN(129:134,76:78);
comp32_DBL = DEBL_E_F_REN(129:134,79:81);
comp33_DBL = DEBL_E_F_REN(129:134,82:84);
comp34_DBL = DEBL_E_F_REN(129:134,85:87);

comp41_EF = E_F(135:140,76:78);
comp42_EF = E_F(135:140,79:81);
comp43_EF = E_F(135:140,82:84);
comp44_EF = E_F(135:140,85:87);
comp41_DBL = DEBL_E_F_REN(135:140,76:78);
comp42_DBL = DEBL_E_F_REN(135:140,79:81);
comp43_DBL = DEBL_E_F_REN(135:140,82:84);
```

```
64 comp44_DBL = DEBL_E_F_REN(135:140,85:87);
65
66 mu11_EF = mean2(comp11_EF); mu12_EF = mean2(comp12_EF); mu13_EF = mean2(comp13_EF); ...
       mu14_EF = mean2(comp14_EF);
67 mu21_EF = mean2(comp21_EF); mu22_EF = mean2(comp22_EF); mu23_EF = mean2(comp23_EF); ...
       mu24_EF = mean2(comp24_EF);
68 mu31_EF = mean2(comp31_EF); mu32_EF = mean2(comp32_EF); mu33_EF = mean2(comp33_EF); ...
       mu34_EF = mean2(comp34_EF);
69 mu41_EF = mean2(comp41_EF); mu42_EF = mean2(comp42_EF); mu43_EF = mean2(comp43_EF); ...
       mu44_EF = mean2(comp44_EF);
70 mu11_DBL = mean2(comp11_DBL); mu12_DBL = mean2(comp12_DBL); mu13_DBL = ...
       mean2(comp13_DBL); mu14_DBL = mean2(comp14_DBL);
71 mu21_DBL = mean2(comp21_DBL); mu22_DBL = mean2(comp22_DBL); mu23_DBL = ...
       mean2(comp23_DBL); mu24_DBL = mean2(comp24_DBL);
72 mu31_DBL = mean2(comp31_DBL); mu32_DBL = mean2(comp32_DBL); mu33_DBL = ...
       mean2(comp33_DBL); mu34_DBL = mean2(comp34_DBL);
73 mu41_DBL = mean2(comp41_DBL); mu42_DBL = mean2(comp42_DBL); mu43_DBL = ...
       mean2(comp43_DBL); mu44_DBL = mean2(comp44_DBL);
74
75 sig11_EF = std2(comp11_EF); sig12_EF = std2(comp12_EF); sig13_EF = std2(comp13_EF); ...
       sig14_EF = std2(comp14_EF);
76 sig21_EF = std2(comp21_EF); sig22_EF = std2(comp22_EF); sig23_EF = std2(comp23_EF); ...
       sig24_EF = std2(comp24_EF);
77 sig31_EF = std2(comp31_EF); sig32_EF = std2(comp32_EF); sig33_EF = std2(comp33_EF); ...
       sig34_EF = std2(comp34_EF);
78 sig41_EF = std2(comp41_EF); sig42_EF = std2(comp42_EF); sig43_EF = std2(comp43_EF); ...
       sig44_EF = std2(comp44_EF);
79 sig11_DBL = std2(comp11_DBL); sig12_DBL = std2(comp12_DBL); sig13_DBL = ...
       std2(comp13_DBL); sig14_DBL = std2(comp14_DBL);
80 sig21_DBL = std2(comp21_DBL); sig22_DBL = std2(comp22_DBL); sig23_DBL = ...
       std2(comp23_DBL); sig24_DBL = std2(comp24_DBL);
81 sig31_DBL = std2(comp31_DBL); sig32_DBL = std2(comp32_DBL); sig33_DBL = ...
       std2(comp33_DBL); sig34_DBL = std2(comp34_DBL);
82 sig41_DBL = std2(comp41_DBL); sig42_DBL = std2(comp42_DBL); sig43_DBL = ...
       std2(comp43_DBL); sig44_DBL = std2(comp44_DBL);
83
84 mu_ROI_ID = mean2(ID_4x4(117:140,76:87));
85 mu_ROI_raw = mean2(E_F(117:140,76:87));
86 mu_ROI_DBL = mean2(DEBL_E_F_REN(117:140,76:87));
87
88 max_ROI_ID = max(max(ID_4x4(117:140,76:87)));
89 max_ROI_raw = max(max(E_F(117:140,76:87)));
90 max_ROI_DBL = max(max(DEBL_E_F_REN(117:140,76:87)));
91
92 sig_ROI_ID = std2(ID_4x4(117:140,76:87));
93 sig_ROI_raw = std2(E_F(117:140,76:87));
94 sig_ROI_DBL = std2(DEBL_E_F_REN(117:140,76:87));
95
96 %% SNR for each region raw data
97
98 SNR_4x4_11 = mu11_EF/sig11_EF;
99 SNR_4x4_12 = mu12_EF/sig12_EF;
100 SNR_4x4_13 = mu13_EF/sig13_EF;
101 SNR_4x4_14 = mu14_EF/sig14_EF;
102
103 SNR_4x4_21 = mu21_EF/sig21_EF;
104 SNR_4x4_22 = mu22_EF/sig22_EF;
105 SNR_4x4_23 = mu23_EF/sig23_EF;
106 SNR_4x4_24 = mu24_EF/sig24_EF;
107
108 SNR_4x4_31 = mu31_EF/sig31_EF;
109 SNR_4x4_32 = mu32_EF/sig32_EF;
110 SNR_4x4_33 = mu33_EF/sig33_EF;
111 SNR_4x4_34 = mu34_EF/sig34_EF;
112
113 SNR_4x4_41 = mu41_EF/sig41_EF;
114 SNR_4x4_42 = mu42_EF/sig42_EF;
115 SNR_4x4_43 = mu43_EF/sig43_EF;
116 SNR_4x4_44 = mu44_EF/sig44_EF;
117
118 %% SNR for deblurred data
```

```
119
120 SNR_4x4_11_DB = mu11_DBL/sig11_DBL;
121 SNR_4x4_12_DB = mu12_DBL/sig12_DBL;
122 SNR_4x4_13_DB = mu13_DBL/sig13_DBL;
123 SNR_4x4_14_DB = mu14_DBL/sig14_DBL;
124
125 SNR_4x4_21_DB = mu21_DBL/sig21_DBL;
126 SNR_4x4_22_DB = mu22_DBL/sig22_DBL;
127 SNR_4x4_23_DB = mu23_DBL/sig23_DBL;
128 SNR_4x4_24_DB = mu24_DBL/sig24_DBL;
129
130 SNR_4x4_31_DB = mu31_DBL/sig31_DBL;
131 SNR_4x4_32_DB = mu32_DBL/sig32_DBL;
132 SNR_4x4_33_DB = mu33_DBL/sig33_DBL;
133 SNR_4x4_34_DB = mu34_DBL/sig34_DBL;
134
135 SNR_4x4_41_DB = mu41_DBL/sig41_DBL;
136 SNR_4x4_42_DB = mu42_DBL/sig42_DBL;
137 SNR_4x4_43_DB = mu43_DBL/sig43_DBL;
138 SNR_4x4_44_DB = mu44_DBL/sig44_DBL;
139
140 %% contrast
141 % [1:1]
142     CNT_EF_1 = (abs(mu21_EF - mu31_EF))/(mu21_EF + mu31_EF);
143     CNT_DB_1 = (abs(mu11_DBL - mu12_DBL))/(mu11_DBL + mu12_DBL);
144     CNT_ID_1 = (abs(mu21_ID - mu31_ID))/(mu21_ID + mu31_ID);
145     CNT_4x4_1_EF = CNT_EF_1/CNT_ID_1;
146     CNT_4x4_1_DB = CNT_DB_1/CNT_ID_1;
147
148     CNT_EF_2 = (abs(mu22_EF - mu32_EF))/(mu22_EF + mu32_EF);
149     CNT_DB_2 = (abs(mu11_DBL - mu12_DBL))/(mu11_DBL + mu12_DBL);
150     CNT_ID_2 = (abs(mu22_ID - mu32_ID))/(mu22_ID + mu32_ID);
151     CNT_4x4_2_EF = CNT_EF_2/CNT_ID_2;
152     CNT_4x4_2_DB = CNT_DB_2/CNT_ID_2;
153
154 % [0:1]
155     CNT_EF_3 = (abs(mu14_EF - mu24_EF))/(mu14_EF + mu24_EF);
156     CNT_DB_3 = (abs(mu11_DBL - mu12_DBL))/(mu11_DBL + mu12_DBL);
157     CNT_ID_3 = (abs(mu14_ID - mu24_ID))/(mu14_ID + mu24_ID);
158     CNT_4x4_3_EF = CNT_EF_3/CNT_ID_3;
159     CNT_4x4_3_DB = CNT_DB_3/CNT_ID_3;
160
161     CNT_EF_4 = (abs(mu34_EF - mu44_EF))/(mu34_EF + mu44_EF);
162     CNT_DB_4 = (abs(mu11_DBL - mu12_DBL))/(mu11_DBL + mu12_DBL);
163     CNT_ID_4 = (abs(mu34_ID - mu44_ID))/(mu34_ID + mu44_ID);
164     CNT_4x4_4_EF = CNT_EF_4/CNT_ID_4;
165     CNT_4x4_4_DB = CNT_DB_4/CNT_ID_4;
166
167 % [1:2]
168     CNT_EF_5 = (abs(mu12_EF - mu13_EF))/(mu12_EF + mu13_EF);
169     CNT_DB_5 = (abs(mu11_DBL - mu12_DBL))/(mu11_DBL + mu12_DBL);
170     CNT_ID_5 = (abs(mu12_ID - mu13_ID))/(mu12_ID + mu13_ID);
171     CNT_4x4_5_EF = CNT_EF_5/CNT_ID_5;
172     CNT_4x4_5_DB = CNT_DB_5/CNT_ID_5;
173
174     CNT_EF_6 = (abs(mu32_EF - mu33_EF))/(mu32_EF + mu33_EF);
175     CNT_DB_2 = (abs(mu11_DBL - mu12_DBL))/(mu11_DBL + mu12_DBL);
176     CNT_ID_6 = (abs(mu32_ID - mu33_ID))/(mu32_ID + mu33_ID);
177     CNT_4x4_6_EF = CNT_EF_6/CNT_ID_6;
178     CNT_4x4_6_DB = CNT_DB_6/CNT_ID_6;
179
180 % [2:3]
181     CNT_EF_7 = (abs(mu22_EF - mu23_EF))/(mu22_EF + mu23_EF);
182     CNT_DB_2 = (abs(mu11_DBL - mu12_DBL))/(mu11_DBL + mu12_DBL);
183     CNT_ID_7 = (abs(mu22_ID - mu23_ID))/(mu22_ID + mu23_ID);
184     CNT_4x4_7_EF = CNT_EF_7/CNT_ID_7;
185     CNT_4x4_7_DB = CNT_DB_7/CNT_ID_7;
186
187     CNT_EF_8 = (abs(mu42_EF - mu43_EF))/(mu42_EF + mu43_EF);
188     CNT_DB_2 = (abs(mu11_DBL - mu12_DBL))/(mu11_DBL + mu12_DBL);
189     CNT_ID_8 = (abs(mu42_ID - mu43_ID))/(mu42_ID + mu43_ID);
```

```
190       CNT_4x4_8_EF = CNT_EF_8/CNT_ID_8;
191       CNT_4x4_8_DB = CNT_DB_8/CNT_ID_8;
192
193   % [3:4]
194       CNT_EF_9 = (abs(mu23_EF - mu24_EF))/(mu23_EF + mu24_EF);
195       CNT_DB_2 = (abs(mu11_DBL - mu12_DBL))/(mu11_DBL + mu12_DBL);
196       CNT_ID_9 = (abs(mu23_ID - mu24_ID))/(mu23_ID + mu24_ID);
197       CNT_4x4_9_EF = CNT_EF_9/CNT_ID_9;
198       CNT_4x4_9_DB = CNT_DB_9/CNT_ID_9;
199
200       CNT_EF_10 = (abs(mu43_EF - mu44_EF))/(mu43_EF + mu44_EF);
201       CNT_DB_2 = (abs(mu11_DBL - mu12_DBL))/(mu11_DBL + mu12_DBL);
202       CNT_ID_10 = (abs(mu43_ID - mu44_ID))/(mu43_ID + mu44_ID);
203       CNT_4x4_10_EF = CNT_EF_10/CNT_ID_10;
204       CNT_4x4_10_DB = CNT_DB_10/CNT_ID_10;
205
206   % [1:4]
207       CNT_EF_11 = (abs(mu11_EF - mu12_EF))/(mu11_EF + mu12_EF);
208       CNT_DB_2 = (abs(mu11_DBL - mu12_DBL))/(mu11_DBL + mu12_DBL);
209       CNT_ID_11 = (abs(mu11_ID - mu12_ID))/(mu11_ID + mu12_ID);
210       CNT_4x4_11_EF = CNT_EF_11/CNT_ID_11;
211       CNT_4x4_11_DB = CNT_DB_11/CNT_ID_11;
212
213       CNT_EF_12 = (abs(mu11_EF - mu21_EF))/(mu11_EF + mu21_EF);
214       CNT_DB_2 = (abs(mu11_DBL - mu12_DBL))/(mu11_DBL + mu12_DBL);
215       CNT_ID_12 = (abs(mu11_ID - mu21_ID))/(mu11_ID + mu21_ID);
216       CNT_4x4_12_EF = CNT_EF_12/CNT_ID_12;
217       CNT_4x4_12_DB = CNT_DB_12/CNT_ID_12;
218
219    % [0:0.5]
220       CNT_EF_13 = (abs(mu13_EF - mu14_EF))/(mu13_EF + mu14_EF);
221       CNT_DB_2 = (abs(mu11_DBL - mu12_DBL))/(mu11_DBL + mu12_DBL);
222       CNT_ID_13 = (abs(mu13_ID - mu14_ID))/(mu13_ID + mu14_ID);
223       CNT_4x4_13_EF = CNT_EF_13/CNT_ID_13;
224       CNT_4x4_13_DB = CNT_DB_13/CNT_ID_13;
225
226       CNT_EF_14 = (abs(mu14_EF - mu24_EF))/(mu14_EF + mu24_EF);
227       CNT_DB_2 = (abs(mu11_DBL - mu12_DBL))/(mu11_DBL + mu12_DBL);
228       CNT_ID_14 = (abs(mu14_ID - mu24_ID))/(mu14_ID + mu24_ID);
229       CNT_4x4_14_EF = CNT_EF_14/CNT_ID_14;
230       CNT_4x4_14_DB = CNT_DB_14/CNT_ID_14;
231
232   %% RMSD ideal vs. deconvolved
233   E_F_max = max(max(E_F));
234   E_F_norm = E_F./E_F_max;
235
236   ID_4x4_max = max(max(ID_4x4));
237   ID_4x4_norm = ID_4x4./ID_4x4_max;
238
239   DEBL_E_F_max = max(max(DEBL_E_F_REN));
240   DEBL_E_F_REN_norm = DEBL_E_F_REN./DEBL_E_F_max;
241
242    [x_ID_4x4,y_ID_4x4] = size(ID_4x4_norm);
243
244   A = (abs((ID_4x4_norm-E_F_norm))).^2;
245   A_x = sum(A,2)./y_ID_4x4;
246   A_xy = sum(A_x)./x_ID_4x4;
247
248   B = (abs(ID_4x4_norm)).^2;
249   B_x = sum(B,2)./y_ID_4x4;
250   B_xy = sum(B_x)./x_ID_4x4;
251   RMSD_dblvsbi = sqrt(A_xy./B_xy);
252   disp(RMSD_dblvsbi);
253
254   %% Proportions based on mean activity in ROIs IDEAL PHANTOM
255   Prop11_4x4_ID = mu11_ID/mu11_ID;
256   Prop12_4x4_ID = mu12_ID/mu11_ID;
257   Prop13_4x4_ID = mu13_ID/mu11_ID;
258   Prop14_4x4_ID = mu14_ID/mu11_ID;
259
260   Prop21_4x4_ID = mu21_ID/mu24_ID;
```

```
261 Prop22_4x4_ID = mu22_ID/mu24_ID;
262 Prop23_4x4_ID = mu23_ID/mu24_ID;
263 Prop24_4x4_ID = mu24_ID/mu24_ID;
264
265 Prop31_4x4_ID = mu31_ID/mu33_ID;
266 Prop32_4x4_ID = mu32_ID/mu33_ID;
267 Prop33_4x4_ID = mu33_ID/mu33_ID;
268 Prop34_4x4_ID = mu34_ID/mu33_ID;
269
270 Prop41_4x4_ID = mu41_ID/mu44_ID;
271 Prop42_4x4_ID = mu42_ID/mu44_ID;
272 Prop43_4x4_ID = mu43_ID/mu44_ID;
273 Prop44_4x4_ID = mu44_ID/mu44_ID;
274
275 %% pROPORTIONS 4X4 PHANTOM rows
276 Prop11_4x4_EF = mu11_EF/mu11_EF;
277 Prop12_4x4_EF = mu12_EF/mu11_EF;
278 Prop13_4x4_EF = mu13_EF/mu11_EF;
279 Prop14_4x4_EF = mu14_EF/mu11_EF;
280
281 Prop21_4x4_EF = mu21_EF/mu24_EF;
282 Prop22_4x4_EF = mu22_EF/mu24_EF;
283 Prop23_4x4_EF = mu23_EF/mu24_EF;
284 Prop24_4x4_EF = mu24_EF/mu24_EF;
285
286 Prop31_4x4_EF = mu31_EF/mu33_EF;
287 Prop32_4x4_EF = mu32_EF/mu33_EF;
288 Prop33_4x4_EF = mu33_EF/mu33_EF;
289 Prop34_4x4_EF = mu34_EF/mu33_EF;
290
291 Prop41_4x4_EF = mu41_EF/mu44_EF;
292 Prop42_4x4_EF = mu42_EF/mu44_EF;
293 Prop43_4x4_EF = mu43_EF/mu44_EF;
294 Prop44_4x4_EF = mu44_EF/mu44_EF;
295 %% pROPORTIONS 4X4 PHANTOM DEBLURRED ROWS
296 Prop11_4x4_EF = mu11_EF/mu11_EF;
297 Prop12_4x4_EF = mu12_EF/mu11_EF;
298 Prop13_4x4_EF = mu13_EF/mu11_EF;
299 Prop14_4x4_EF = mu14_EF/mu11_EF;
300
301 Prop21_4x4_EF = mu21_EF/mu24_EF;
302 Prop22_4x4_EF = mu22_EF/mu24_EF;
303 Prop23_4x4_EF = mu23_EF/mu24_EF;
304 Prop24_4x4_EF = mu24_EF/mu24_EF;
305
306 Prop31_4x4_EF = mu31_EF/mu33_EF;
307 Prop32_4x4_EF = mu32_EF/mu33_EF;
308 Prop33_4x4_EF = mu33_EF/mu33_EF;
309 Prop34_4x4_EF = mu34_EF/mu33_EF;
310
311 Prop41_4x4_EF = mu41_EF/mu44_EF;
312 Prop42_4x4_EF = mu42_EF/mu44_EF;
313 Prop43_4x4_EF = mu43_EF/mu44_EF;
314 Prop44_4x4_EF = mu44_EF/mu44_EF;
315
316 %% deblurred columns
317 Prop11_4x4_DB = mu11_DBL/mu11_DBL;
318 Prop21_4x4_DB = mu21_DBL/mu11_DBL;
319 Prop31_4x4_DB = mu31_DBL/mu11_DBL;
320 Prop41_4x4_DB = mu41_DBL/mu11_DBL;
321
322 Prop12_4x4_DB = mu12_DBL/mu12_DBL;
323 Prop22_4x4_DB = mu22_DBL/mu12_DBL;
324 Prop32_4x4_DB = mu32_DBL/mu12_DBL;
325 Prop42_4x4_DB = mu42_DBL/mu12_DBL;
326
327 Prop13_4x4_DB = mu13_DBL/mu33_DBL;
328 Prop23_4x4_DB = mu23_DBL/mu33_DBL;
329 Prop33_4x4_DB = mu33_DBL/mu33_DBL;
330 Prop43_4x4_DB = mu43_DBL/mu33_DBL;
331
```

```
Prop14_4x4_DB = mu14_DBL/mu44_DBL;
Prop24_4x4_DB = mu24_DBL/mu44_DBL;
Prop34_4x4_DB = mu34_DBL/mu44_DBL;
Prop44_4x4_DB = mu44_DBL/mu44_DBL;
```

Bibliography

[1] Hugo JWL Aerts, Geert Bosmans, Angela AW van Baardwijk, Andre LAJ Dekker, Michel C Oellers, Philippe Lambin, and Dirk De Ruysscher. Stability of 18f-deoxyglucose uptake locations within tumor during radiotherapy for nsclc: a prospective study. *International Journal of Radiation Oncology* Biology* Physics*, 71(5):1402–1407, 2008.

[2] Hugo J.W.L. Aerts, Angela A.W. van Baardwijk, Steven F. Petit, Claudia Offermann, Judith van Loon, Ruud Houben, Anne-Marie C. Dingemans, Rinus Wanders, Liesbeth Boersma, Jacques Borger, Gerben Bootsma, Wiel Geraedts, Cordula Pitz, Jean Simons, Bradly G. Wouters, Michel Oellers, Philippe Lambin, Geert Bosmans, Andre L.A.J. Dekker, and Dirk De Ruysscher. Identification of residual metabolic-active areas within individual NSCLC tumours using a pre-radiotherapy 18fluorodeoxyglucose-PET-CT scan. *Radiotherapy and Oncology*, 91(3):386–392, June 2009. ISSN 01678140. doi: 10.1016/j.radonc.2009.03.006.

[3] Vinita Ahuja, R Edward Coleman, James Herndon, and Edward F Patz Jr. The prognostic significance of fluorodeoxyglucose positron emission tomography imaging for patients with nonsmall cell lung carcinoma. *Cancer: Interdisciplinary International Journal of the American Cancer Society*, 83 (5):918–924, 1998.

[4] Adam Alessio, Paul Kinahan, et al. Pet image reconstruction. *Nuclear medicine*, 1:1–22, 2006.

[5] Khalid O Alfarouk, Muntaser E Ibrahim, Robert A Gatenby, and Joel S Brown. Riparian ecosystems in human cancers. *Evolutionary applications*, 6(1):46–53, 2013.

[6] National Electrical Manufacturers Association et al. Performance measurements of positron emission tomographs. *NEMA standards publication NU 2-2001*, 2001.

[7] John AD Aston, Vincent J Cunningham, Marie-Claude Asselin, Alexander Hammers, Alan C Evans, and Roger N Gunn. Positron emission tomography partial volume correction: estimation and algorithms. *Journal of Cerebral Blood Flow & Metabolism*, 22(8):1019–1034, 2002.

[8] Gillian C. Barnett, Catherine M. L. West, Alison M. Dunning, Rebecca M. Elliott, Charlotte E. Coles, Paul D. P. Pharoah, and Neil G. Burnet. Normal tissue reactions to radiotherapy: towards tailoring treatment dose by genotype. *Nature Reviews Cancer*, 9(2):134–142, February 2009. ISSN 1474-175X, 1474-1768. doi: 10.1038/nrc2587.

[9] Martijn PF Berger and Frans ES Tan. Robust designs for linear mixed effects models. *Journal of the Royal Statistical Society: Series C (Applied Statistics)*, 53(4):569–581, 2004.

[10] J Martin Brown and William R Wilson. Exploiting tumour hypoxia in cancer treatment. *Nature Reviews Cancer*, 4(6):437, 2004.

[11] Jeremy MC Brown, John E Gillam, David M Paganin, and Matthew R Dimmock. Laplacian erosion: an image deblurring technique for multi-plane gamma-cameras. *IEEE Transactions on Nuclear Science*, 60(5):3333–3342, 2013.

[12] J. Bruin. Introduction to linear mixed models, February 2011.

[13] Rebecca A. Burrell, Nicholas McGranahan, Jiri Bartek, and Charles Swanton. The causes and consequences of genetic heterogeneity in cancer evolution. *Nature*, 501(7467):338–345, September 2013. ISSN 0028-0836, 1476-4687. doi: 10.1038/nature12625.

[14] Robert W Burt, Orrin W Perkins, Bernard E Oppenheim, Donald S Schauwecker, Leon Stein, Henry N Wellman, and Robert M Witt. Direct comparison of fluorine-18-fdg spect, fluorine-18-fdg pet and rest thallium-201 spect for detection of myocardial viability. *Journal of Nuclear Medicine*, 36(2):176–179, 1995.

[15] KS Clifford Chao, Walter R Bosch, Sasa Mutic, Jason S Lewis, Farrokh Dehdashti, Mark A Mintun, James F Dempsey, Carlos A Perez, James A Purdy, and Michael J Welch. A novel approach to overcome hypoxic tumor resistance: Cu-atsm-guided intensity-modulated radiation therapy. *International Journal of Radiation Oncology* Biology* Physics*, 49(4):1171–1182, 2001.

[16] Arion F Chatziioannou, Simon R Cherry, Yiping Shao, Robert W Silverman, Ken Meadors, Thomas H Farquhar, Marjan Pedarsani, and Michael E Phelps. Performance evaluation of micropet: a high-resolution lutetium oxyorthosilicate pet scanner for animal imaging. *Journal of Nuclear Medicine*, 40(7):1164, 1999.

[17] Huafu Chen, Xu Lei, and Dezhong Yao. An improved ordered subsets expectation maximization positron emission computerized tomography reconstruction. *Computers in biology and medicine*, 37(12):1780–1785, 2007.

[18] Xiao-Ting Chen, Xin Zhao, Zhen-Hua Gao, Yong-Sheng Gao, Bai-Jiang Zhang, Zheng Fu, Dian-Bin Mu, Jin-Ming Yu, and Xue Meng. Proliferation pet image to characterize pathological spatial features in patients with non-small cell lung cancer: a pilot study. *International journal of clinical and experimental medicine*, 8(6):9758, 2015.

[19] Simon R. Cherry, James A. Sorenson, and Michael E. Phelps. Positron Emission Tomography. In *Physics in Nuclear Medicine*, pages 307–343. Elsevier, 2012. ISBN 978-1-4160-5198-5. doi: 10.1016/B978-1-4160-5198-5.00018-6.

[20] Cristian C Constantinescu and Jogeshwar Mukherjee. Performance evaluation of an inveon pet preclinical scanner. *Physics in Medicine & Biology*, 54(9):2885, 2009.

[21] Benjamin L Cox, Stephen A Graves, Mohammed Farhoud, Todd E Barnhart, Justin J Jeffery, Kevin W Eliceiri, and Robert J Nickles. Development of a novel linearly-filled derenzo micropet phantom. *American journal of nuclear medicine and molecular imaging*, 6(3):199, 2016.

[22] Clemens Decristoforo, Uwe Haberkorn, Roland Haubner, Walter Mier, and Sibylle I Ziegler. Pet and spect. In *Small Animal Imaging*, pages 361–402. Springer, 2017.

[23] Christophe Deroulers, David Ameisen, Mathilde Badoual, Chloé Gerin, Alexandre Granier, and Marc Lartaud. Analyzing huge pathology images with open source software. *Diagnostic pathology*, 8(1):92, 2013.

[24] INC ENVISIONTEC. EnvisionTEC's P4 Mini. `https://envisiontec.com/3d-printers/perfactory-family/p4-mini/`, 2017.

[25] Yusuf E Erdi, Kenneth Rosenzweig, Alev K Erdi, Homer A Macapinlac, Yu-Chi Hu, Louise E Braban, John L Humm, Olivia D Squire, Chen-Shou Chui, Steven M Larson, et al. Radiotherapy treatment planning for patients with non-small cell lung cancer using positron emission tomography (pet). *Radiotherapy and Oncology*, 62(1):51–60, 2002.

[26] Aniek J.G. Even, Judith van der Stoep, Catharina M.L. Zegers, Bart Reymen, Esther G.C. Troost, Philippe Lambin, and Wouter van Elmpt. PET-based dose painting in non-small cell lung cancer: Comparing uniform dose escalation with boosting hypoxic and metabolically active sub-volumes. *Radiotherapy and Oncology*, 116(2):281–286, August 2015. ISSN 01678140. doi: 10.1016/j.radonc.2015.07.013.

[27] Aniek J.G. Even, Bart Reymen, Matthew D. La Fontaine, Marco Das, Felix M. Mottaghy, José S.A. Belderbos, Dirk De Ruysscher, Philippe Lambin, and Wouter van Elmpt. Clustering of multiparametric functional imaging to identify high-risk subvolumes in non-small cell lung cancer. *Radiotherapy and Oncology*, 125(3):379–384, December 2017. ISSN 01678140. doi: 10.1016/j.radonc.2017.09.041.

[28] S Fasanella, E Leonardi, C Cantaloni, C Eccher, I Bazzanella, D Aldovini, E Bragantini, L Morelli, LV Cuorvo, A Ferro, et al. Proliferative activity in human breast cancer: Ki-67 automated evaluation and the influence of different ki-67 equivalent antibodies. In *Diagnostic pathology*, volume 6, page S7. BioMed Central, 2011.

[29] Eric R Fearon and Bert Vogelstein. A genetic model for colorectal tumorigenesis. *Cell*, 61(5):759–767, 1990.

[30] Jacques Ferlay, Isabelle Soerjomataram, Rajesh Dikshit, Sultan Eser, Colin Mathers, Marise Rebelo, Donald Maxwell Parkin, David Forman, and Freddie Bray. Cancer incidence and mortality worldwide: sources, methods and major patterns in globocan 2012. *International journal of cancer*, 136(5):E359–E386, 2015.

[31] FormLabs. 3D Printing Technology Comparison: SLA vs. DLP. `https://formlabs.com/blog/3d-printing-technology-comparison-sla-dlp/`, 2017.

[32] Laura Ghesquière-Diérickx. Improvement of tumour heterogeneity quantification in pet images. *uuid:0183c922-76a4-4507-96dd-38362e27da0a*, 2017.

[33] Charles Gillham, Daniel Zips, Falk Pönisch, Carsten Evers, Wolfgang Enghardt, Nasreddin Abolmaali, Klaus Zöphel, Steffen Appold, Tobias Hölscher, Jörg Steinbach, et al. Additional pet/ct in week 5–6 of radiotherapy for patients with stage iii non-small cell lung cancer as a means of dose escalation planning? *Radiotherapy and Oncology*, 88(3):335–341, 2008.

[34] Kevin A Hallgren. Computing inter-rater reliability for observational data: an overview and tutorial. *Tutorials in quantitative methods for psychology*, 8(1):23, 2012.

[35] N Hanna, M Neubauer, C Yiannoutsos, R McGarry, J Arseneau, R Ansari, et al. Phase iii study of cisplatin, etoposide, and concurrent chest radiation with or without consolidation docetaxel in patients with inoperable stage iii non-small-cell lung cancer: the hoosier oncology group and us oncology. *J Clin Oncol*, pages 5755–60, 2008.

[36] Harvey R Herschman. Micro-PET imaging and small animal models of disease. *Current Opinion in Immunology*, 15(4):378–384, August 2003. ISSN 09527915. doi: 10.1016/S0952-7915(03)00066-9.

[37] Manuel Hidalgo, Frederic Amant, Andrew V Biankin, Eva Budinská, Annette T Byrne, Carlos Caldas, Robert B Clarke, Steven de Jong, Jos Jonkers, Gunhild Mari Mælandsmo, et al. Patient-derived xenograft models: an emerging platform for translational cancer research. *Cancer discovery*, 4(9):998–1013, 2014.

[38] Kotaro Higashi, Yoshimichi Ueda, Aya Sakurai, Xiao MingWang, Linfeng Xu, Manabu Murakami, Hiroyasu Seki, Manabu Oguchi, Suzuka Taki, Yoshihiro Nambu, et al. Correlation of glut-1 glucose transporter expression with [18 f] fdg uptake in non-small cell lung cancer. *European journal of nuclear medicine*, 27(12):1778–1785, 2000.

[39] Jan Nyrop Jakobsen and Jens Benn Sørensen. Clinical impact of ki-67 labeling index in non-small cell lung cancer. *Lung Cancer*, 79(1):1–7, January 2013. ISSN 01695002. doi: 10.1016/j.lungcan.2012.10.008.

[40] Aparna Kanakatte, Jayavardhana Gubbi, Nallasamy Mani, Tomas Kron, and David Binns. A pilot study of automatic lung tumor segmentation from positron emission tomography images using standard uptake values. In *Computational Intelligence in Image and Signal Processing, 2007. CIISP 2007. IEEE Symposium on*, pages 363–368. IEEE, 2007.

[41] Jin Su Kim, Jae Sung Lee, Ki Chun Im, Su Jin Kim, Seog-Young Kim, Dong Soo Lee, and Dae Hyuk Moon. Performance measurement of the micropet focus 120 scanner. *Journal of Nuclear Medicine*, 48(9):1527–1535, 2007.

[42] Christof Knoess, Stefan Siegel, Anne Smith, Danny Newport, Norbert Richerzhagen, Alexandra Winkeler, Andreas Jacobs, Rhonda N Goble, Rudolf Graf, Klaus Wienhard, et al. Performance evaluation of the micropet r4 pet scanner for rodents. *European journal of nuclear medicine and molecular imaging*, 30(5):737–747, 2003.

[43] Juho Konsti, Mikael Lundin, Heikki Joensuu, Tiina Lehtimäki, Harri Sihto, Kaija Holli, Taina Turpeenniemi-Hujanen, Vesa Kataja, Liisa Sailas, Jorma Isola, et al. Development and evaluation of a virtual microscopy application for automated assessment of ki-67 expression in breast cancer. *BMC clinical pathology*, 11(1):3, 2011.

[44] Anne-Vibeke Laenkholm, Dorthe Grabau, Maj-Lis Møller Talman, Eva Balslev, Anne Marie Bak Jylling, Tomasz Piotr Tabor, Morten Johansen, Anja Brügmann, Giedrius Lelkaitis, Tina Di Caterino, et al. An inter-observer ki67 reproducibility study applying two different assessment methods: on behalf of the danish scientific committee of pathology, danish breast cancer cooperative group (dbcg). *Acta Oncologica*, 57(1):83–89, 2018.

[45] Richard Laforest, Desmond Longford, Stefan Siegel, Danny F Newport, and Jeffrey Yap. Performance evaluation of the micropet®—focus-f120. *IEEE Transactions on Nuclear Science*, 54(1): 42–49, 2007.

[46] Philippe Lambin, Steven F Petit, Hugo JWL Aerts, Wouter JC van Elmpt, Cary JG Oberije, Maud HW Starmans, Ruud GPM van Stiphout, Guus AMS van Dongen, Kristoff Muylle, Patrick Flamen, et al. The estro breur lecture 2009. from population to voxel-based radiotherapy: exploiting intra-tumour and intra-organ heterogeneity for advanced treatment of non-small cell lung cancer. *Radiotherapy and oncology*, 96(2):145–152, 2010.

[47] Sanghyeb Lee, Jens Gregor, and Dustin Osborne. Development and validation of a complete gate model of the siemens inveon trimodal imaging platform. *Molecular Imaging*, 12(7):7290–2013, 2013.

[48] Craig S Levin and Edward J Hoffman. Calculation of positron range and its effect on the fundamental limit of positron emission tomography system spatial resolution. *Physics in Medicine & Biology*, 44(3):781, 1999.

[49] Lian Tao Li, Guan Jiang, Qian Chen, and Jun Nian Zheng. Ki67 is a promising molecular target in the diagnosis of cancer. *Molecular medicine reports*, 11(3):1566–1572, 2015.

[50] C Clifton Ling, John Humm, Steven Larson, Howard Amols, Zvi Fuks, Steven Leibel, and Jason A Koutcher. Towards multidimensional radiotherapy (md-crt): biological imaging and biological conformality. *International Journal of Radiation Oncology* Biology* Physics*, 47(3):551–560, 2000.

[51] Sandy Z Liu, Paul N Staats, Lindsay Goicochea, Borislav A Alexiev, Nirav Shah, Renee Dixon, and Allen P Burke. Automated quantification of ki-67 proliferative index of excised neuroendocrine tumors of the lung. *Diagnostic pathology*, 9(1):174, 2014.

[52] Michaël G Magagnin, Marianne Koritzinsky, and Bradly G Wouters. Patterns of tumor oxygenation and their influence on the cellular hypoxic response and hypoxia-directed therapies. *Drug resistance updates*, 9(4-5):185–197, 2006.

[53] Eirik Malinen, Åste Søvik, Dimitre Hristov, Øyvind S Bruland, and Dag Rune Olsen. Adapting radiotherapy to hypoxic tumours. *Physics in Medicine & Biology*, 51(19):4903, 2006.

[54] Marcelo Mamede, Tatsuya Higashi, Masanori Kitaichi, Koichi Ishizu, Takayoshi Ishimori, Yuji Nakamoto, Kazuhiro Yanagihara, Mio Li, Fumihiro Tanaka, Hiromi Wada, et al. [18f] fdg uptake and pcna, glut-1, and hexokinase-ii expressions in cancers and inflammatory lesions of the lung. *Neoplasia*, 7(4):369–379, 2005.

[55] William H Martin, Dominique Delbeke, James A Patton, Brian Hendrix, Zeev Weinfeld, Israel Ohana, Robert M Kessler, and Martin P Sandler. Fdg-spect: correlation with fdg-pet. *Journal of nuclear medicine: official publication, Society of Nuclear Medicine*, 36(6):988–995, 1995.

[56] Andriy Marusyk, Vanessa Almendro, and Kornelia Polyak. Intra-tumour heterogeneity: a looking glass for cancer? *Nature Reviews Cancer*, 12(5):323, 2012.

[57] Pawitra Masa-Ah and Somphob Soongsathitanon. A novel standardized uptake value (suv) calculation of pet dicom files using matlab. In *WSEAS Int Conf on Biomedical Electronics and Biomedical Informatics*, 2010.

[58] Saroj P Mathupala, Annette Rempel, and Peter L Pedersen. Aberrant glycolytic metabolism of cancer cells: a remarkable coordination of genetic, transcriptional, post-translational, and mutational events that lead to a critical role for type ii hexokinase. *Journal of bioenergetics and biomembranes*, 29(4):339–343, 1997.

[59] Nicholas McGranahan and Charles Swanton. Biological and Therapeutic Impact of Intratumor Heterogeneity in Cancer Evolution. *Cancer Cell*, 27(1):15–26, January 2015. ISSN 15356108. doi: 10.1016/j.ccell.2014.12.001.

[60] Evelina Miele, Gian Paolo Spinelli, Federica Tomao, Angelo Zullo, Filippo De Marinis, Giulia Pasciuti, Luigi Rossi, Federica Zoratto, and Silverio Tomao. Positron emission tomography (pet) radiotracers in oncology–utility of 18f-fluoro-deoxy-glucose (fdg)-pet in the management of patients with non-small-cell lung cancer (nsclc). *Journal of Experimental & Clinical Cancer Research*, 27(1): 52, 2008.

[61] Everett J. Moding, Michael B. Kastan, and David G. Kirsch. Strategies for optimizing the response of cancer and normal tissues to radiation. *Nature Reviews Drug Discovery*, 12(7):526–542, July 2013. ISSN 1474-1776, 1474-1784. doi: 10.1038/nrd4003.

[62] ZMA Mohammed, DC McMillan, B Elsberger, JJ Going, C Orange, E Mallon, JC Doughty, and J Edwards. Comparison of visual and automated assessment of ki-67 proliferative activity and their impact on outcome in primary operable invasive ductal breast cancer. *British journal of cancer*, 106(2):383, 2012.

[63] Kishan A. T. Naipal, Nicole S. Verkaik, Humberto Sánchez, Carolien H. M. van Deurzen, Michael A. den Bakker, Jan H.J. Hoeijmakers, Roland Kanaar, Maaike P.G. Vreeswijk, Agnes Jager, and Dik C. van Gent. Tumor slice culture system to assess drug response of primary breast cancer. *BMC Cancer*, 16(1), December 2016. ISSN 1471-2407. doi: 10.1186/s12885-016-2119-2.

[64] Takahiro Nakagomi, Taichiro Goto, Yosuke Hirotsu, Daichi Shikata, Kenji Amemiya, Toshio Oyama, Hitoshi Mochizuki, and Masao Omata. Elucidation of radiation-resistant clones by a serial study of intratumor heterogeneity before and after stereotactic radiotherapy in lung cancer. *Journal of thoracic disease*, 9(7):E598, 2017.

[65] Johan Nuyts, Patrick Dupont, Sigrid Stroobants, Roel Benninck, Luc Mortelmans, and Paul Suetens. Simultaneous maximum a posteriori reconstruction of attenuation and activity distributions from emission sinograms. *IEEE transactions on medical imaging*, 18(5):393–403, 1999.

[66] Steven F. Petit, Hugo J.W.L. Aerts, Judith G.M. van Loon, Claudia Offermann, Ruud Houben, Bjorn Winkens, Michel C. Öllers, Philippe Lambin, Dirk De Ruysscher, and André L.A.J. Dekker. Metabolic control probability in tumour subvolumes or how to guide tumour dose redistribution in non-small cell lung cancer (NSCLC): An exploratory clinical study. *Radiotherapy and Oncology*, 91(3):393–398, June 2009. ISSN 01678140. doi: 10.1016/j.radonc.2009.02.020.

[67] Pramudita R. Prasetyanti and Jan Paul Medema. Intra-tumor heterogeneity from a cancer stem cell perspective. *Molecular Cancer*, 16(1), December 2017. ISSN 1476-4598. doi: 10.1186/s12943-017-0600-4.

[68] Mariano Provencio, Dolores Isla, Antonio Sánchez, and Blanca Cantos. Inoperable stage III non-small cell lung cancer: Current treatment and role of vinorelbine. *Journal of Thoracic Disease*, 3 (3):8, 2011.

[69] Suresh Ramalingam and Chandra Belani. Systemic chemotherapy for advanced non-small cell lung cancer: recent advances and future directions. *The Oncologist*, 13(Supplement 1):5–13, 2008.

[70] Ben Redwood, Filemon Schffer, and Brian Garret. 3d printing. In *The 3D Printing Handbook: Technologies, design and applications*. 3D Hubs, 2017.

[71] Gopal B Saha. Performance characteristics of pet scanners. In *Basics of PET Imaging*, pages 121–142. Springer, 2016.

[72] Toshiro Sato, Daniel E Stange, Marc Ferrante, Robert GJ Vries, Johan H Van Es, Stieneke Van Den Brink, Winan J Van Houdt, Apollo Pronk, Joost Van Gorp, Peter D Siersema, et al. Long-term expansion of epithelial organoids from human colon, adenoma, adenocarcinoma, and barrett's epithelium. *Gastroenterology*, 141(5):1762–1772, 2011.

[73] Hans-Helge Seifert, Andrea Meyer, Marcus V Cronauer, Jiri Hatina, Mirko Müller, Harald Rieder, Michele J Hoffmann, Rolf Ackermann, and Wolfgang A Schulz. A new and reliable culture system for superficial low-grade urothelial carcinoma of the bladder. *World journal of urology*, 25(3):297–302, 2007.

[74] Sara Sheikhbahaei, Esther Mena, Anusha Yanamadala, Siddaling Reddy, Lilja B Solnes, Jason Wachsmann, and Rathan M Subramaniam. The value of fdg pet/ct in treatment response assessment, follow-up, and surveillance of lung cancer. *American Journal of Roentgenology*, 208(2): 420–433, 2017.

[75] Åste Søvik, Eirik Malinen, and Dag Rune Olsen. Strategies for Biologic Image-Guided Dose Escalation: A Review. *International Journal of Radiation Oncology*Biology*Physics*, 73(3):650–658, March 2009. ISSN 03603016. doi: 10.1016/j.ijrobp.2008.11.001.

[76] Yuan-Chuan Tai, Ananya Ruangma, Douglas Rowland, Stefan Siegel, Danny F Newport, Patrick L Chow, and Richard Laforest. Performance evaluation of the micropet focus: a third-generation micropet scanner dedicated to animal imaging. *Journal of nuclear medicine*, 46(3):455–463, 2005.

[77] Le Tang, Fang Wei, Yingfen Wu, Yi He, Lei Shi, Fang Xiong, Zhaojian Gong, Can Guo, Xiayu Li, Hao Deng, Ke Cao, Ming Zhou, Bo Xiang, Xiaoling Li, Yong Li, Guiyuan Li, Wei Xiong, and Zhaoyang Zeng. Role of metabolism in cancer cell radioresistance and radiosensitization methods. *Journal of Experimental & Clinical Cancer Research*, 37(1), December 2018. ISSN 1756-9966. doi: 10.1186/s13046-018-0758-7.

[78] Hannah Mary Thomas, Paul E Kinahan, James Jebaseelan E Samuel, and Stephen R Bowen. Impact of tumour motion compensation and delineation methods on FDG PET-based dose painting plan quality for NSCLC radiation therapy. *Journal of Medical Imaging and Radiation Oncology*, 62 (1):81–90, February 2018. ISSN 17549477. doi: 10.1111/1754-9485.12693.

[79] Daniela Thorwarth, Susanne-Martina Eschmann, Frank Paulsen, and Markus Alber. Hypoxia dose painting by numbers: a planning study. *International Journal of Radiation Oncology* Biology* Physics*, 68(1):291–300, 2007.

[80] F. Tixier, D. Vriens, C. Cheze-Le Rest, M. Hatt, J. A. Disselhorst, W. J. G. Oyen, L.-F. de Geus-Oei, E. P. Visser, and D. Visvikis. Comparison of Tumor Uptake Heterogeneity Characterization Between Static and Parametric 18f-FDG PET Images in Non-Small Cell Lung Cancer. *Journal of Nuclear Medicine*, 57(7):1033–1039, July 2016. ISSN 0161-5505. doi: 10.2967/jnumed.115.166918.

[81] Yuji Tsutsui, Shinichi Awamoto, Kazuhiko Himuro, Yoshiyuki Umezu, Shingo Baba, and Masayuki Sasaki. Edge artifacts in point spread function-based pet reconstruction in relation to object size and reconstruction parameters. *Asia Oceania Journal of Nuclear Medicine and Biology*, 5(2):134, 2017.

[82] A.B. Ulrich and P.M. Pour. Cell lines. In Sydney Brenner and Jefferey H. Miller, editors, *Encyclopedia of Genetics*, pages 310 – 311. Academic Press, New York, 2001. ISBN 978-0-12-227080-2. doi: https://doi.org/10.1006/rwgn.2001.0173.

[83] Angela van Baardwijk, Geert Bosmans, André Dekker, Marinus van Kroonenburgh, Liesbeth Boersma, Stofferinus Wanders, Michel Öllers, Ruud Houben, André Minken, Philippe Lambin, et al. Time trends in the maximal uptake of fdg on pet scan during thoracic radiotherapy. a prospective study in locally advanced non-small cell lung cancer (nsclc) patients. *Radiotherapy and oncology*, 82(2):145–152, 2007.

[84] Angela van Baardwijk, Christophe Dooms, Robert Jan van Suylen, Erik Verbeken, Monique Hochstenbag, Cary Dehing-Oberije, Dennis Rupa, Silvia Pastorekova, Sigrid Stroobants, Ulrich Buell, et al. The maximum uptake of 18f-deoxyglucose on positron emission tomography scan correlates with survival, hypoxia inducible factor-1α and glut-1 in non-small cell lung cancer. *European Journal of cancer*, 43(9):1392–1398, 2007.

[85] Pierre Vera, Pierre Bohn, Agathe Edet-Sanson, Alice Salles, Sebastien Hapdey, Isabelle Gardin, Jean-François Ménard, Romain Modzelewski, Luc Thiberville, and Bernard Dubray. Simultaneous positron emission tomography (pet) assessment of metabolism with 18f-fluoro-2-deoxy-d-glucose (fdg), proliferation with 18f-fluoro-thymidine (flt), and hypoxia with 18fluoro-misonidazole (f-miso) before and during radiotherapy in patients with non-small-cell lung cancer (nsclc): a pilot study. *Radiotherapy and Oncology*, 98(1):109–116, 2011.

[86] Sidra Waheed, Joan M Cabot, Niall P Macdonald, Trevor Lewis, Rosanne M Guijt, Brett Paull, and Michael C Breadmore. 3d printed microfluidic devices: enablers and barriers. *Lab on a Chip*, 16 (11):1993–2013, 2016.

[87] Simone Weber and Andreas Bauer. Small animal pet: aspects of performance assessment. *European journal of nuclear medicine and molecular imaging*, 31(11):1545–1555, 2004.

[88] R Glenn Wells, Michael A King, Peter H Simkin, Philip F Judy, A Bertrand Brill, Howard C Gifford, Robert Licho, P Hendrik Pretorius, Peter B Schneider, and David W Seldin. Comparing filtered backprojection and ordered-subsets expectation maximization for small-lesion detection and localization in^ 6^ 7ga spect. *Journal of nuclear medicine*, 41(8):1391–1399, 2000.

[89] Scott D Wollenweber, Adam M Alessio, and Paul E Kinahan. A phantom design for assessment of detectability in pet imaging. *Medical physics*, 43(9):5051–5062, 2016.

[90] Yuka Yamamoto, Yoshihiro Nishiyama, Shinya Ishikawa, Jun Nakano, Sung Soo Chang, Shuji Bandoh, Nobuhiro Kanaji, Reiji Haba, Yoshio Kushida, and Motoomi Ohkawa. Correlation of 18 f-flt and 18 f-fdg uptake on pet with ki-67 immunohistochemistry in non-small cell lung cancer. *European journal of nuclear medicine and molecular imaging*, 34(10):1610–1616, 2007.

[91] Rutao Yao, Jürgen Seidel, Calvin A Johnson, Margaret E Daube-Witherspoon, Michael V Green, and Richard E Carson. Performance characteristics of the 3-d osem algorithm in the reconstruction of small animal pet images. *IEEE transactions on medical imaging*, 19(8):798–804, 2000.

[92] Yinyin Yuan. Spatial Heterogeneity in the Tumor Microenvironment. *Cold Spring Harbor Perspectives in Medicine*, 6(8):a026583, August 2016. ISSN 2157-1422. doi: 10.1101/cshperspect.a026583.

[93] Songji Zhao, Yuji Kuge, Takafumi Mochizuki, Toshiyuki Takahashi, Kunihiro Nakada, Masayuki Sato, Toshiki Takei, and Nagara Tamaki. Biologic correlates of intratumoral heterogeneity in 18f-fdg distribution with regional expression of glucose transporters and hexokinase-ii in experimental tumor. *Journal of Nuclear Medicine*, 46(4):675, 2005.